UNIVERSITÀ DEGLI STUDI DI PADOVA

Dipartimento di Ingegneria Elettrica

Scuola di Dottorato di Ricerca in Ingegneria Industriale

Indirizzo Ingegneria Elettrotecnica

Ciclo XXIII

STUDY OF THE POWER SUPPLY SYSTEM
FOR THE ACCELERATION GRIDS
OF THE ITER NEUTRAL BEAM INJECTOR

Direttore della Scuola: Ch.mo Prof. Paolo Bariani

Coordinatore di Indirizzo: Ch.mo Prof. Giovanni Martinelli

Supervisore: Ch.mo Prof. Francesco Gnesotto

Tutor: Ing. Vanni Toigo

Dottorando: Alberto Ferro

31 gennaio 2011

Dedicated to Federica, my wife

Contents

Abstract

Thermonuclear fusion is a promising alternative to hydrocarbons as a clean and almost unlimited source of energy, presently the only one having the potential to substitute completely the non-renewable resources. The increase and the volatility of the oil prices, the foreseeable forthcoming shortage of oil and natural gas and the apparent co-responsibility of the combustion of coal and hydrocarbons in the recent climate changes make fusion more and more interesting. ITER (International Thermonuclear Experimental Reactor) is a large-scale prototype of a fusion power plant, under construction in Cadarache, south of France. ITER, resulting from a large international cooperation, will be the most ambitious of a series of fusion experiments built and operated around the world, in which a gas of light nuclei is heated up to become plasma, and suspended into a toroidal vacuum chamber by means of powerful magnetic fields produced by electromagnets. If the plasma temperature is sufficient and if the magnetic confinement is good, the fusion reactions become probable enough to produce higher fusion energy than the energy necessary to sustain the fusion boundary conditions. The main aim of ITER is to prove the physical and technological feasibility of fusion as an effective source of energy and to develop the technologies to be implemented in the future fusion reactors.

In ITER, to heat the plasma, the contribution of 2 or 3 Neutral Beam Injectors (NBI) is necessary. In these devices, a beam of negative ions (40 A) is accelerated up to 1MeV by a set of grids having increasing potentials. Then, the beam is neutralized and injected into the ITER vacuum vessel, heating the plasma by collision with plasma particles. The NBI accelerator is fed by a dedicated power supply system (AGPS, Acceleration Grid Power Supply), rated for a total power of 54.7 MW. Being the technical requirements of the overall ITER NBI system well above the performances presently achieved in similar neutral beam injectors in fusion experiments, a test facility is foreseen and presently under construction in the CNR Research Area in Padova. In this facility, called PRIMA (Padova Research on ITER Megavolt Accelerator), the present NBI design will be tested and, where necessary, improvements and further developments of the NBI components will be implemented before their installation in ITER.

This thesis presents the studies carried out by the author on the AGPS system, in collaboration with the research group of Consorzio RFX and the researchers of the other institutions involved in the project. The objectives of these studies are the following: to verify the feasibility of the AGPS, to support the definition of a reference design and to verify the achievement of the required performance. In section 1, a brief introduction to the energy problem and the thermonuclear fusion is given. Section 2 describes the principle of a tokamak, the most promising configuration for a fusion reactor. Section 3 contains a short description of the ITER experiment. In section 4, the main components of the ITER NBI are presented, together with a brief introduction to the PRIMA test facility. In section 5, the power supply system of the ITER NBI and the layouts foreseen on ITER and PRIMA sites are introduced. The main requirements for the AGPS are given in section 6, focusing in particular

on those related with the analyses presented in this thesis. In section 7, the reference design of the AGPS is revised and the calculations for the most important components of the AGPS conversion system are given. The reference design presented here, of course, is the result of the contributions of many researchers working under the respective national domestic agencies involved in the project. Moreover, some open points of the AGPS design are still under discussion and the AGPS specifications are not finalized yet, thus the parameters and the technical choices shown here not necessarily represent the final version that will be implemented in the real system. The same considerations are applicable to section 8, where the design of the AGPS control system is described. The performance of the AGPS system defined in the previous sections has been tested by using proper computer models and simulations, under normal and abnormal conditions. In sections 9, 10, 11 and 12, the models developed by the author and the results of the simulations are described. In section 13, some specific issues regarding the tests to be performed on the real AGPS system are investigated. In particular, an alternative type of dummy load is proposed by the author, and a solution to test the voltage control loop is studied, by means of original computer models and simulations. The conclusions of this work are summarized in section 14.

Sommario

La fusione termonucleare controllata costituisce una promettente alternativa agli idrocarburi quale fonte pulita e quasi illimitata di energia, attualmente la sola potenzialmente in grado di sostituire del tutto le fonti non rinnovabili. L'incremento e la volatilità dei prezzi del petrolio, la prevedibile futura scarsità di idrocarburi e l'apparente corresponsabilità della combustione di tali sostanze nei recenti cambiamenti climatici rendono la fusione sempre più attraente. ITER (International Thermonuclear Experimental Reactor) è un prototipo su larga scala di un reattore a fusione, in costruzione a Cadarache, nel sud della Francia. ITER, frutto di una vasta collaborazione internazionale, sarà il più ambizioso di una serie di esperimenti di fusione costruiti e resi operativi nel mondo, nei quali un gas di atomi leggeri è riscaldato fino a divenire un plasma e sospeso in una camera da vuoto toroidale per mezzo di potenti campi magnetici prodotti da elettromagneti. Se la temperatura del plasma è sufficiente e il confinamento magnetico è abbastanza buono, le reazioni di fusione diventano abbastanza probabili da produrre più energia di quanta non ne serva per sostenere le condizioni di fusione. Lo scopo principale di ITER è di provare la fattibilità fisica e tecnologica della fusione quale fonte di energia e di sviluppare le tecnologie che dovranno essere implementate nei futuri reattori a fusione.

In ITER, per riscaldare il plasma è necessario il contributo di 2 o 3 iniettori di atomi neutri (NBI). In questi dispositivi, un fascio di ioni negativi (40 A) è accelerato fino a 1 MeV da una serie di griglie aventi potenziali crescenti. Il fascio viene quindi neutralizzato e iniettato nella camera da vuoto di ITER, dove collide con le particelle di plasma contribuendo al loro riscaldamento. L'acceleratore dell'NBI è alimentato da un sistema dedicato (AGPS, Acceleration Grid Power Supply) dimensionato per 54.7 MW totali. Essendo i requisiti tecnici del sistema NBI nel suo complesso molto superiori alle prestazioni attualmente raggiunte in NBI simili operanti negli esperimenti di fusione, una test facility è prevista e attualmente in costruzione nell'area della ricerca del CNR di Padova. In questa facility, detta PRIMA (Padova Research on ITER Megavolt Accelerator), il progetto attuale dell'NBI verrà testato e migliorato laddove necessario e verranno implementati ulteriori sviluppi dei componenti dell'NBI prima della loro installazione in ITER.

Questa tesi espone gli studi condotti dall'autore sull'AGPS, in collaborazione con il gruppo di ricerca del Consorzio RFX di Padova e i ricercatori degli altri enti coinvolti nel progetto. Questi studi hanno lo scopo di verificare la fattibilità dell'AGPS, di supportare la definizione del progetto di riferimento e di verificare il raggiungimento delle prestazioni richieste. Nella sezione 1, è riportata una breve introduzione sul problema energetico e sulla fusione termonucleare controllata. La sezione 2 descrive il principio di funzionamento di un tokamak, la più promettente configurazione per un reattore a fusione. La sezione 3 contiene una breve descrizione dell'esperimento ITER. Nella sezione 4 vengono presentati i componenti principali dell'iniettore di ITER, oltre ad una breve introduzione sulla test facility PRIMA. In sezione 5, vengono introdotti il sistema di alimentazione dell'NBI e i relativi layout. I principali requisiti dell'AGPS sono forniti nella sezione 6, con particolare riguardo a quelli relativi alle analisi

presentate in questa tesi. Nella sezione 7, si fornisce una revisione del progetto di riferimento dell'AGPS, descrivendo i calcoli dei principali componenti del sistema di conversione. Il progetto di riferimento presentato in questa tesi, ovviamente, è il risultato del contributo di molti ricercatori che operano all'interno dei relativi enti di ricerca nazionali coinvolti nella sua definizione. Inoltre, alcuni punti aperti del progetto dell'AGPS sono ancora in discussione, e le specifiche dell'AGPS non sono ancora state ultimate. Di conseguenza, i parametri e le scelte tecniche mostrati in questa tesi non rispecchiano necessariamente la versione finale che sarà implementata nel sistema reale. Le stesse considerazioni valgono per la sezione 8, in cui si descrive il progetto del sistema di controllo dell'AGPS. Le prestazioni dell'AGPS descritto nelle sezioni precedenti sono state verificate per mezzo di appositi modelli e simulazioni al calcolatore, sia in condizioni normali che anormali. Nelle sezioni 9, 10, 11 e 12 vengono descritti i modelli sviluppati dall'autore e i risultati delle simulazioni. Nella sezione 13, vengono studiate alcune questioni specifiche riguardanti i test da realizzarsi sull'AGPS reale. In particolare, l'autore propone un tipo di carico fittizio alternativo e studia un sistema per testare il controllo di tensione in catena chiusa, per mezzo di modelli al calcolatore e simulazioni originali. Le conclusioni della tesi sono riassunte nella sezione 14.

Acronyms

ACCC	Active Control Correction Coils
AGPS	Acceleration Grid Power Supply
AGPS-CS	Acceleration Grid Power Supply-Conversion System
AGPS-DCG	Acceleration Grid Power Supply-DC Generator
BBD	Breakdown & Beam-Off Detector
BD	BreakDown
BPPS	Bias Plate Power Supply
BPS	Bias Power Supply
CAD	Computer Aided Design
CCPS	Correction Coils Power Supply
CIS	Central Interlock System
CODAC	COntrol and Data ACquisition
CNR	Italian National Research Council
CSS	Central Safety System
DA	Domestic Agency
DCG	DC Generator
DNB	Diagnostic Neutral Beam
DL	Dummy Load
EG	Extraction Grid
EGPS	Extraction Grid Power Supply
EM	Electromagnetic
EU	European
EUDA	European Domestic Agency
GRPS	Ground Related Power Supplies
HF	High Frequency
HMI	Human Machine Interface
HNB	Heating Neutral Beam
HV	High Voltage
HVD	High Voltage Deck
IGCT	Integrated Gate-Commutated Thyristor
ISEPS	Ion Source and Extraction Power Supplies
IO	ITER Organization
ITER	International Thermonuclear Experimental Reactor
JA	Japanese
JADA	Japanese Domestic Agency
LCC	Local Control Cubicle
LCS	Local Control System
LV	Low Voltage
MAMuG	Multi Aperture Multi Gap
MITICA	Megavolt ITER Injector & Concept Advancement
MSE	Motional Stark Effect
MV	Medium Voltage
NB	Neutral Beam
NBI	Neutral Beam Injector
NPC	Neutral Point Clamped
PCS	Plant Control System
PG	Plasma Grid
PGFPS	Plasma Grid Filter Power Supply
PS	Power Supply
PIS	Plant Interlock system
PRIMA	Padova Research on ITER Megavolt Accelerator
PSS	Plant Safety System
RF	Radio Frequency
RFPS	Radio Frequency Power Supply
RFX	Reverse Field eXperiment
RMFC	Residual Magnetic Field Coils
RMFPS	Residual Magnetic Field Power Supply
rms	Root Mean Square
RID	Residual Ion Dump
SINGAP	Single Aperture Single Gap
SPIDER	Source for Production of Ion of Deuterium Extracted from RF plasma
TL	Transmission Line

1 Controlled thermonuclear fusion

1.1 The energy problem

The evolution of the human society towards a more comfortable way of life requires a more intensive use of commodities such as household appliances, private and public transports, domestic heating, and a wider development of the mechanized industry to produce goods and services. Despite any reasonable improvement in the efficiency of all these energy demanding systems, the progressively increasing number of people gaining access to the new technologies will imply for sure an increasing demand of primary energy. On the other hand, the present society reached this high level of technological development by using a large amount of non-renewable resources, in particular coal, hydrocarbons (oil and natural gas) and uranium. Figure 1-1 reports the contribution of each primary energy source to the world primary energy production, as a function of time [1].

Nowadays, the peak of production of coal and oil seems more and more close in time [2]. When it will happen, the world will run into shortage of fossil fuels, which will imply energy cost increase and a set of implications also in the stability of the modern societies, making progressively harder to increase or at least to keep constant the present level of economical development.
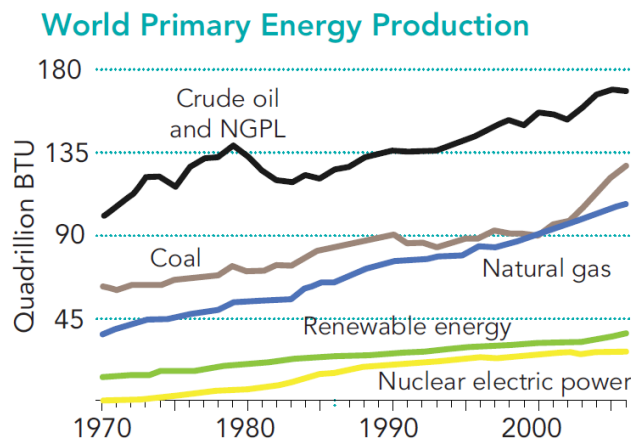
Figure 1-1 – World primary energy production

At the same time, the intensive use of fossil fuels is not a viable solution to sustain the future energy consumption, because of the negative impact on the environment. In fact, combustion of coal and hydrocarbons is an important source of air pollution and contributes to the production of greenhouse gases, such as carbon dioxide. Recent studies [3] seem to demonstrate that these gases have a significant impact in the overheating of the planet measured in the recent years, being therefore co-responsible of the latest climate changes.

For both the above reasons, alternatives to fossil fuels must be discovered, developed and widely used in a short time. A set of technologies to exploit renewable energy resources is already available or under development, for example the solar energy technology (photovoltaic and solar thermal), the wind turbines, the geothermal power plants, the hydropower or tidal

power plants and the bio-fuels technology. Nevertheless, all these energy resources suffer of a set of problems, which are inherent to the nature of the resource itself. For example, all these resources show low densities, in the sense that an intensive exploitation of them implies an anti-economic waste of large territories, often interfering with other human activities. Moreover, wide electric power generation with solar and wind technologies is risky, because these energy resources are intermittent and the storage of huge quantities of energy is impracticable. Finally, most of these technologies, also due to the consequent wide use of terrains, show some negative impact on the environment. For example, presently the most used renewable resource for production of electricity is represented by the hydropower plants. Unfortunately, the intensive use of natural water basins or the creation of new basins by flooding natural valleys could destroy the local natural eco-systems and could make unavailable a large amount of useful terrains, like in China for the construction of the well-known Three-gorges big hydropower plant.

Concerns about climate changes, security of energy supply, and depletion of fossil fuel reserves have spurred a revival of interest in nuclear power generation in Europe and North America, while other regions continue or initiate an expansion in exploiting this energy resource [1]. Nevertheless, an energy strategy based on fission power has to cope with two key challenges, which have to be overcome. The first is the development of civil nuclear programs in all parts of the world without risking the proliferation of nuclear weapon technologies. The second is to safely deal, in an environmentally compatible way, with the unavoidable nuclear waste. Even if technical proposals are available for long-term nuclear storage, including deep geological disposal, the assessment and perception of the risks associated with the transport and storage of radioactive waste will continue to be reconsidered. Newer reactor designs offer the promise of using more efficiently the nuclear fuels, and of creating less waste or waste having shorter lifetime, but some technical issues still remain to be solved.

1.2 The fusion reaction

A very promising line of research focuses on a completely different concept of nuclear power plant, based on nuclear fusion reactions of light nuclei, instead of fission of heavy nuclei of unstable (and then, radioactive) elements [4]. Nuclear fusion is the process that powers the stars in the Universe. The most viable fusion reaction for a fusion power plant considers as reacting elements Deuterium and Tritium, which are isotopes of Hydrogen:

$$^{2}_{1}D + ^{3}_{1}T \rightarrow ^{4}_{2}He + ^{1}_{0}n + 17.6 MeV$$

(1-1)

If Deuterium and Tritium are heated at very high temperatures, in the order of 20 keV (which corresponds to about $200 \cdot 10^6$ K), the kinetic energy of the nuclei overcomes the Coulomb repulsion, then the nuclei likely collide and react, producing a nucleus of Helium, a neutron

and energy. This energy is due to the mass defect of the reaction products with respect to the reagents, in agreement with the well-known Einstein's law:

$$E = mc^2 \tag{1-2}$$

where m is the mass defect and c is the speed of light. The energy is spread between the neutron (14.1 MeV) and the Helium nucleus (3.5 MeV). The reaction is represented graphically in Figure 1-2.
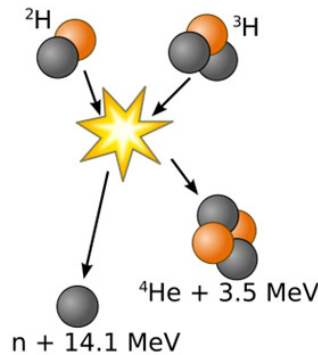
Figure 1-2 – Fusion reaction between Deuterium and Tritium

Also other fusion reactions are possible, as for example between nuclei of Deuterium, or nuclei of Hydrogen, but the reaction (1.1) is the most likely at lower temperatures, as shown in Figure 1-3, where the cross-sections of various possible reactions are shown as a function of temperature.
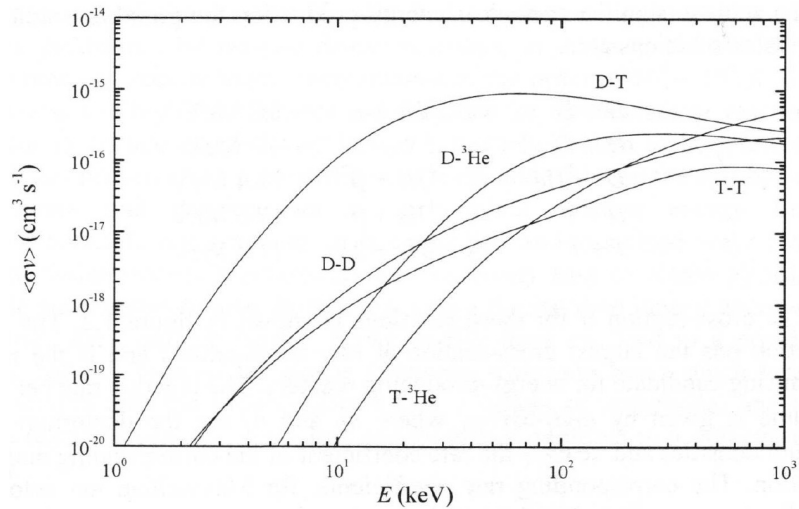
Figure 1-3 – Fusion reaction rate <σv> for couples of reactants

Deuterium is a relatively abundant element on Earth, being 0.014% of ocean waters composed by D_2O (heavy water). Naturally occurring tritium, instead, is extremely rare on

Earth, where trace amounts are formed by the interaction of the atmosphere with cosmic rays. Tritium is radioactive, with a half-life of 12.3 years. It can be obtained from Lithium with the nuclear reactions (1-3) and (1-4).

$$_3^6Li + n \rightarrow _2^4He + _1^3T + 4.8MeV \qquad (1\text{-}3)$$

$$_3^7Li + n + 2.5MeV \rightarrow _2^4He + _1^3T + n \qquad (1\text{-}4)$$

Reaction (1.4) is endothermic, but the reagent is ^{7}Li, which is more abundant on Earth than ^{6}Li.

1.3   The fusion power plant

In the present concepts of fusion power plants, Deuterium and Tritium react as in (1.1). At temperatures in the order of 20 keV, Deuterium and Tritium are in the form of plasma, which is an electrically conducting gas in which the electrons are detached from their respective nuclei. To heat the reactants up to the requested extreme temperatures, they have to be excited and confined, to minimize as much as possible any direct contact of the plasma with the walls of the reactor core. Two main ways are envisaged to confine such plasmas: the inertial confinement and the magnetic confinement [5].

In the inertial confinement fusion approach, the nuclear fusion reactions are initiated by heating and compressing a fuel target, typically in the form of a pellet made by a mixture of Deuterium and Tritium (in the order of 10 mg). To compress and heat the fuel, energy is delivered to the outer layer of the target using high-energy beams of laser light, electrons or ions. The heated outer layer explodes outward, producing a reaction force against the remainder of the target, accelerating it inwards and sending shock waves into the center. A sufficiently powerful set of shock waves can compress and heat the fuel at the center so much that fusion reactions o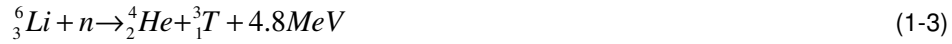ccur. The energy released by these reactions will then heat the surrounding fuel, which may also begin to undergo fusion.

In the magnetic confinement fusion concept, the plasma is confined inside a vacuum vessel by means of magnetic fields, produced by powerful electromagnets. The plasma is heated by the current induced by time-varying magnetic fields, by electromagnetic waves or by neutral beam injection.

In both inertial and magnetic confinement approaches, inside a fusion reactor the neutrons produced by the nuclear reactions are collected in the blanket, which covers the internal surface of the vacuum vessel. There, the neutrons transfer their energy by heating a proper fluid, which undergoes a thermodynamic cycle, finally producing electricity, as in a conventional electric power plant.

In a Deuterium-Tritium power plant, the blanket may also contain Lithium in some form (liquid or solid), which reacts, aided by some neutron multiplier (based for example on Beryllium), with the high energy neutrons, producing the Tritium necessary to sustain the fusion reactions

(as for eq. (1-3) or eq. (1-4)). A blanket containing Lithium is called "breeding blanket" and allows to avoid any external Tritium supply. In conclusion, if the breeding blanket is available, the actual nuclear fuels of the fusion power plant are Lithium and Deuterium, and the exhaust is Helium, a non-radioactive well manageable and safe element.

A schematic view of a fusion power plant with breeding blanket is represented in Figure 1-4.
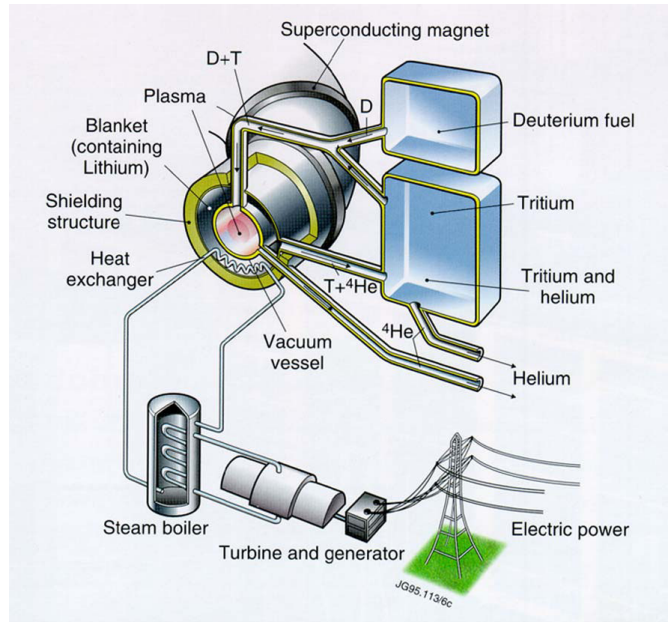
Figure 1-4 – Scheme of principle of a fusion power plant

In the magnetic confinement fusion concept, the Helium nuclei generated by the reactions, being electrically charged, are confined by the magnetic fields and contribute to heat the plasma. This process could lead in principle to the self-sustainment of the reaction, reducing the external heating contribution to the power merely necessary to control the plasma. The Helium ash, together with the outer colder part of the D-T plasma, is collected by a dedicated pumping system, called divertor, and then separated from Deuterium and Tritium, which are re-injected into the reactor.

A fusion power plant would have a series of big advantages with respect to the conventional fission power plants. One is represented by the under-critical working conditions. This means that in a fusion reactor it would be simply impossible, also in case of total loss of control, to get an unwanted increase of power from nuclear reactions. In a fission reactor, instead, a total loss of control (involving both passive and active control systems) would produce in principle the fission of all the nuclear fuel, with consequent production of an unmanageable quantity of energy, causing the fusion of the core. For a fusion reactor, there is no possibility of a 'run-away' reaction because the conditions for fusion are very precise and any alteration of them causes the cooling of the plasma within seconds and stops the reaction.

Moreover, fusion fuels are abundantly available and inherently safe. Only tiny amounts of Deuterium and Tritium are necessary to fuel the fusion reaction: just a few grams are present

in the plasma at any time. In fact, a fusion reaction is about four million times more energetic than a chemical reaction such as the burning of coal, oil or gas. While a 1 GW coal-fired power plant requires 2.7 million tons of coal per year, a fusion plant of the kind envisioned for the second half of this century would only require 250 kg of fuel per year, half of it Deuterium, half of it Tritium. As an alternative, Tritium can be produced by a corresponding quantity of Lithium if a breeding blanket is provided.

In addition, fusion emits no pollution or greenhouse gases in the atmosphere. Its major by-product is Helium: an inert, non-toxic gas. Although no radioactive products are produced by the fusion reaction itself, energetic neutrons interacting with the walls of the vacuum vessel will activate these materials over time. Also, materials can become contaminated by Beryllium and Tungsten dust, and Tritium. Therefore, proper precautions shall be taken to manage elements of the reactor exposed to neutron fluxes, both during operation of the power plant and during decommissioning. For example, all the maintenance operations on such devices shall be made by remote handling, in dedicated hot cell facilities. In any case, the problem of storing these components is orders of magnitude easier to solve than for the waste from a fission power plant.

2 Magnetic confinement: the tokamak

The simplest magnetic configuration conceivable to confine a hot plasma is a linear solenoid, a cylinder wound with magnetic coils producing a field whose lines of force run parallel to the axis of the cylinder. Such a field would hinder ions and electrons from being lost radially, but not from being lost from the ends of the solenoid. To solve this problem, two approaches could be envisaged. One is to provide two magnetic mirrors at the ends, the other is to eliminate the ends themselves by changing the cylinder into a torus.

Among the torus, the most studied magnetic configurations are: the tokamak, the Stellarator and the Reverse Field Pinch (RFP). The tokamak is, up to now, the most promising solution [6]. The schematic view of a tokamak is represented in Figure 2-1.
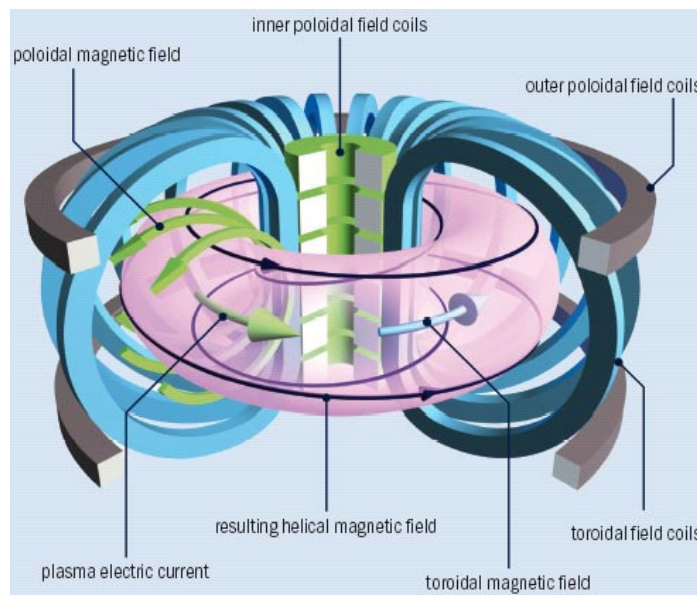
Figure 2-1 – Schematic view of a tokamak

In the tokamak, vacuum vessel and plasma have a toroidal shape, elongated in the vertical direction. Besides the toroidal magnetic field, also a strong toroidal current must be provided. Three main sets of coils are needed. The toroidal field coils generate the toroidal magnetic field, along which the plasma particles are confined. The central solenoid generates the poloidal magnetic flux derivative over time necessary for the first gas breakdown and to induce the toroidal current inside the plasma. This current, in the order of some MA (mega-ampere) on reactor relevant tokamaks, provide the Ohmic heating of the plasma. Finally, to counteract the outward force acting on the current ring, a set of equilibrium coils produces a vertical magnetic field.

As the temperature of the plasma rises, the plasma resistance, and therefore the Ohmic heating effect, decreases. Therefore, in tokamaks, to heat the plasma up to fusion relevant temperatures, auxiliary heating systems shall be adopted [6]. Moreover, the time duration of the inductive sustainment of the plasma current is limited by the poloidal magnetic flux

available: after a full swing of such flux, no more flux time derivative is possible, so no more current can be magnetically induced inside the plasma. Therefore, steady state plasmas require external heating and current drive systems.

Two families of external heating and current drive methods are envisaged [7]: neutral beams and high-frequency electromagnetic waves. Neutral beam injection consists in shooting high energy particles into the plasma [8]. Outside of the tokamak, Deuterium is ionized in a proper ion source and accelerated up to the required energy level. These accelerated ions then pass through a neutralizer, where their electrical charge is removed. The high velocity neutral particles are then injected into the vacuum vessel, where they collide with the plasma particles, transferring their energy.

Three types of electromagnetic waves are presently considered to heat the plasma, each matching a resonance frequency of plasma ions or electrons, to maximize the heat transfer: Ion Cyclotron Resonance Heating (ICRH, 30÷50 MHz), Electron Cyclotron Resonance Heating (ECRH 100÷200 GHz) and Lower Hybrid Current Drive (LHCD). On ICRH, tetrods are used as oscillating amplifiers on the radio frequency source whereas, for LHCD and ECRH, klystrons and gyrotrons are used respectively. In comparison to the ICRH system, the ECRH has the advantage that the RF beam can be transmitted through air, which simplifies the design and allows the source to be far from the plasma, simplifying maintenance.

Beside Ohmic heating, neutral beam injection and high-frequency waves, in a fusion reactor also the self-heating of the plasma, due to the Helium nuclei produced by the fusion reactions, has to be considered.

3 ITER

ITER (International Thermonuclear Experimental Reactor) is a large-scale scientific experiment that aims at demonstrating the technical and scientific feasibility of magnetic thermonuclear fusion to produce energy [9]. ITER will be the world's largest and most advanced experimental tokamak nuclear fusion reactor, and it is currently under construction at Cadarache, in the south of France.

Presently, the project's members are China, European Union, India, Japan, Korea, Russia and United States [10]. Most of the components that make up the ITER project are to be procured by each of the participating countries and contributed in kind through so-called Domestic Agencies. In many cases the engineering and the technologies required to manufacture these components are very advanced. The procurements are managed by ITER Organization (IO), the international organization for the construction of ITER, which has its headquarters in Cadarache.

The ITER fusion reactor is designed to produce 500 MW of thermal power, with a ratio Q between output fusion power and input power to the tokamak higher than 10. Hereby the machine is expected to demonstrate the principle of getting more energy out of the fusion process than is used to sustain it, a target not yet achieved in the present experimental fusion reactors. Nevertheless, ITER will be again an experimental device, unable to inject electricity into the grid. The first commercial demonstration fusion power plant, named DEMO, is proposed to follow on the research of ITER, to bring fusion energy to the commercial markets [11]. A conceptual design for such a machine could be completed by 2017. If the research progresses as hoped, DEMO will lead fusion into its industrial era, beginning operation in the early 2030s and putting fusion power into the grid as early as 2040.

A cross section of the ITER reactor is represented in Figure 3-1. Here, the main components are highlighted. In particular, the poloidal and toroildal magnets are visible, together with the vacuum vessel, the breeding blanket and the divertor. The toroidal and poloidal magnets are superconducting, therefore they have to be maintained at cryogenic temperatures (4.5 K). Thus, the reactor is enclosed inside a cryostat under vacuum (28.6 m diameter, 29.3 m height), providing thermal insulation.

The ITER mission includes specifically the following objectives:

- to demonstrate the feasibility to produce ten times more thermal energy from fusion heating than is supplied by auxiliary heating ($Q \geq 10$);
- to produce a steady-state plasma with $Q \geq 5$, using auxiliary heating systems only;
- to maintain a fusion pulse for up to 400 seconds;
- to ignite a 'burning' (self-sustaining) plasma;
- to develop technologies and processes needed for a fusion power plant, including superconducting magnets and remote handling;
- to implement a working breeding blanket, able to collect most of the thermal energy produced by fusion reactions and to produce Tritium to supply the plasma.
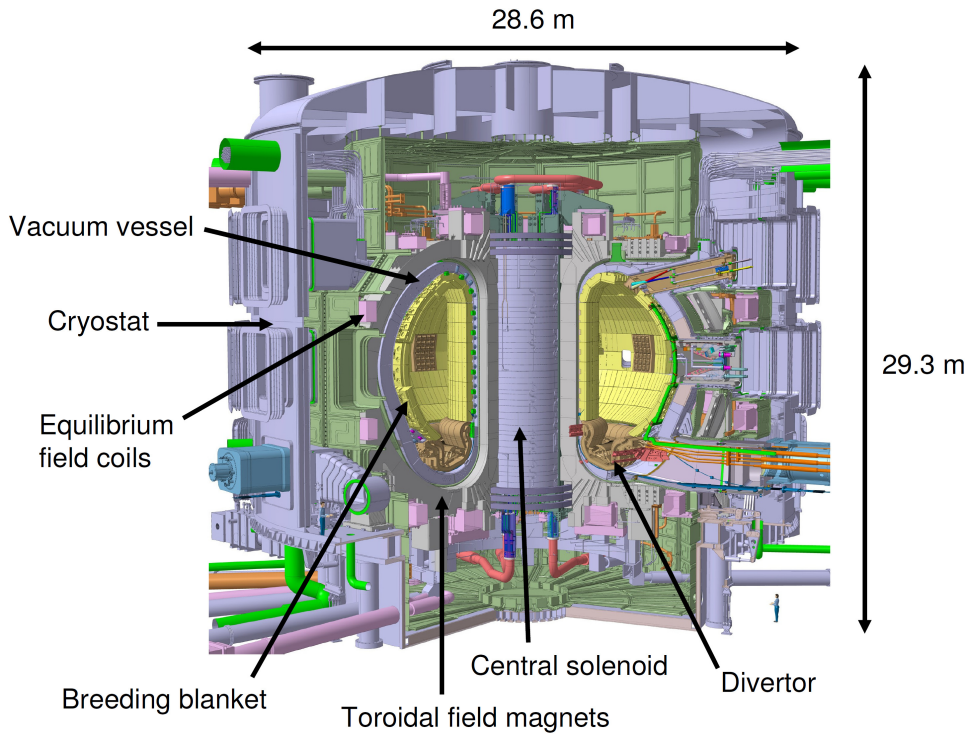
Figure 3-1 – Cross section of the ITER reactor

The main parameters of ITER are listed in Table 3-1 (for inductive operation scenario I, [12]). Also non-inductive scenarios are foreseen, in which the external heating power is completely sustained by neutral beam injection and radio-frequency, without any current induced by poloidal field coils. In this case, the pulse duration can be extended up to 1 hour.

Table 3-1 – Main parameters of ITER for inductive operation scenario I

Parameter	Inductive operation I
Major plasma radius	6.2 m
Minor plasma radius	2 m
Plasma volume	831 m^3
Toroidal field	5.3 T
Plasma current	15 MA
Confinement time	3.4 s
Fusion power	500 MW
Additional power	50 MW
Energy multiplication Q	10
Burn time	400 s

New physical regimes and a variety of technological issues will be explored with ITER. For example, conditions in which the particles significantly contribute to plasma heating, maybe producing a new class of plasma instabilities never studied on previous devices. A set of new technologies will be tested in ITER, like advanced materials facing very large heat and particle fluxes, concepts for a tritium breeding module, superconducting magnets under high neutron flux and many others. The auxiliary systems needed to achieve the conditions expected in

ITER include an external heating and current drive capability higher than 50 MW and several advanced diagnostics for both analysis and plasma control. All these features make ITER a key step in solving many of the scientific and engineering issues concerning a burning plasma, towards the demonstration of nuclear fusion as a viable source of energy.

Presently, the ITER site in Cadarache is levelled and the construction of the main buildings is starting. For 2015 it is foreseen to start the tokamak construction, to be concluded in 2018. The first Hydrogen plasma of ITER is foreseen in 2019. After some experimental years, also Deuterium plasmas will be produced and, finally, Deuterium-Tritium plasmas in 2026.

Figure 3-2 – The ITER platform in Cadarache, where construction will begin in 2010 on buildings and facilities

Figure 3-3 – A sketch of the ITER site as foreseen in 2019

4   Neutral beam injection

4.1   Principle and main components

Neutral Beam Injectors (NBI) are used to shoot uncharged high-energy Deuterium atoms into the plasma where, by way of collision, they transfer their energy to the plasma particles.

The present concept of NBI [13] used in fusion experiments (see Figure 4-2 in the following) foresees an ion source, in which the gas is ionized. The source is included in the NBI vacuum vessel, in which different vacuum pressures are maintained in the various zones, as requested for the optimal working of the NBI. The ions produced in the ion source, being electrically charged, can be extracted by the voltage across a couple of grids, the plasma grid (PG, facing the plasma) and the extraction grid (EG). After passing the EG, the ions are accelerated by an electrostatic accelerator, made by a series of accelerating grids at different potentials. Then, the accelerated ion beam passes through a neutralizer, in which a suitable gas pressure is maintained in order to de-ionize the beam by collision with neutral atoms. Downstream the neutralizer, however, not all the beam ions are converted into neutrals. The residual ions are deflected by transversal grids at different potentials inside a Residual Ion Dump (Electrostatic RID, ERID). Alternatively, the residual ions could be deflected by a magnetic field (Magnetic RID, MRID). Downstream the RID, the accelerated beam is composed of neutrals only and can be injected into the plasma through a port hole of the vacuum vessel of the reactor.

To avoid undue beam deflections inside the NBI, the stray magnetic fields along the ion beam path should be minimized. Moreover, the beam optics is determined by the shape of the grid surfaces and of the grid holes and it is optimized if the accelerating voltage and the ion beam current follow a certain equation, called perveance matching law:

$$I_{beam} = \frac{k}{\sqrt{m}} V_{acc}^{3/2} \qquad\qquad\qquad (4\text{-}1)$$

where I_{beam} is the ion beam current which crosses the grids, V_{acc} is the accelerating voltage, m is the mass of the ions and k is a constant which is determined by the accelerator geometry.

In the present NBI concepts, the ions can be produced inside the ion source by means of arc discharges or alternatively by radiofrequency excitation of the gas. The arc discharge is commonly produced inside the ion source between proper tungsten electrodes and the source inner surface. Conversely, the radiofrequency excitation is induced by coils, wound around proper cavities of the source and fed by RF generators. The main disadvantage of the arc-based ion source is the need of frequent maintenance, due to electrode consumption, which requires periodic replacements. Maintenance operations should be avoided as much as possible in a fusion reactor, especially on devices radio-activated by exposition to high neutron fluxes.

4.2 Neutral beam injectors for ITER

For ITER, 2 heating NBI are foreseen, with the possibility to add another heating neutral beam (HNB) if required. In addition, a diagnostic neutral beam (DNB) has to be provided [14].

The large volume and the high temperature and density of the ITER plasma impose new requirements on the HNB. In order to penetrate far enough into the plasma, the neutrals must be accelerated up to 1 MeV. For comparison, the maximum rated beam energy reached up to now is 500 keV on JT-60U experiment [15]. At these high energies the positively-charged ions become difficult to neutralize, as shown in Figure 4-1. Therefore, the ITER NBI shall produce and accelerate negative ions of Deuterium or Hydrogen. Although high energy negative ions are easier to neutralize in a conventional neutralization cell, they are also more challenging to create and to handle than positive ions. In fact, the additional electron that gives to the ion its negative charge is only loosely bound, and consequently readily lost.
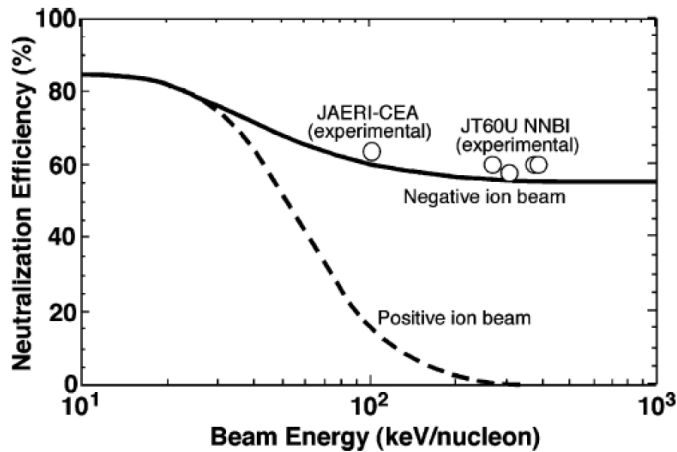
Figure 4-1 – Neutralization efficiency for positive and negative Deuterium and Hydrogen ions against beam energy per nucleon

The main requirements of the ITER HNB are summarized in Table 4-1 [16]. The required extracted ion current density, source pressure, pulse length, extraction area and uniformity have never been attained together at the same time in previous experimental ion sources.

Table 4-1 – Requirements of the ITER HNB

Parameter	ITER Requirements
Beam energy	1 MeV (D-) / 870 kV (H-)
Beam current	40 A (D-) / 46 A (H-)
Beamlet divergence	< 7 mrad
Extracted ion current density	29 mA/cm^2 (D-) / 35 mA/cm^2 (H-)
Extraction voltage	12 kV
Source pressure	0.3 Pa
Ion / electron ratio	>1 (D-) / >2 (H-)
Pulse length	3600 s
Source dimension	1.5 × 0.6 m^2
Extraction area	$\cong$ 1500 cm^2
Uniformity	±10%

In Figure 4-2 a schematic view of the ITER HNB is represented. To give an idea of the overall dimensions of this device, it is worth to say that the total length of the beam vessel is 15 m. The main beam line components are visible, in particular the ion source, the neutralizer, the residual ion dump and the calorimeter. The very high voltage (1 MV) that feeds the acceleration grids is provided by means of a SF_6 gas insulated Transmission Line (TL). The high voltage bushing is necessary to separate the SF_6 from the high vacuum in the beam vessel, and to transmit at the same time the accelerating voltages to the grids. In the same Figure, on the lower and upper sides of the vessel, the correction coils are shown. Their aim is to compensate the external stray magnetic field produced by the tokamak coils, which otherwise would deflect the ion beam inside the NBI.
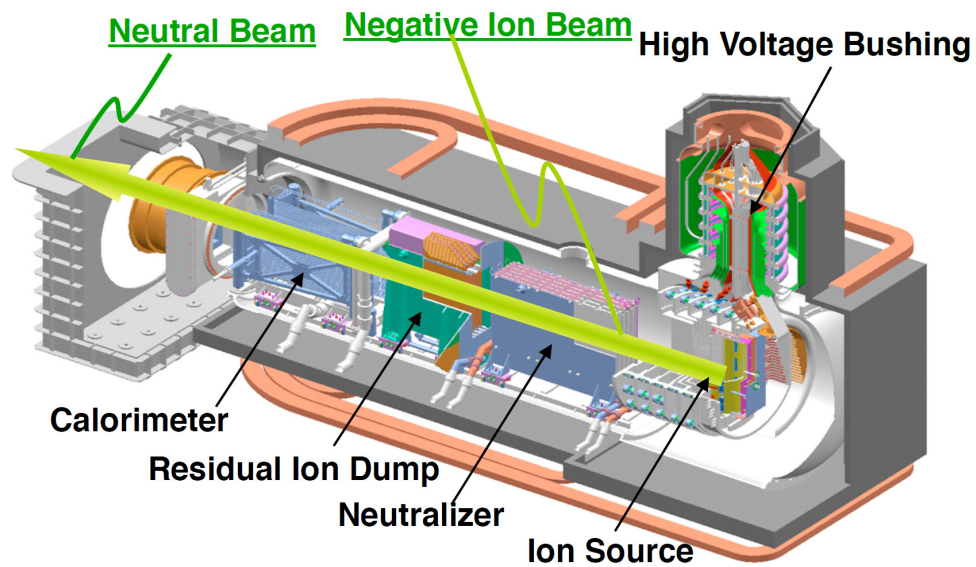
Figure 4-2 – Schematic view of the ITER neutral beam injector

Figure 4-3 represents a cross section view of a HNB installed on ITER. The TL coming from the upper floor is shown, together with the duct that conveys the neutral beam up to the tokamak porthole. The beam vessel is electrically connected to the tokamak vessel, but it is mechanically decoupled from it, in order to allow movements of the tokamak due to electromagnetic forces and temperature changes.
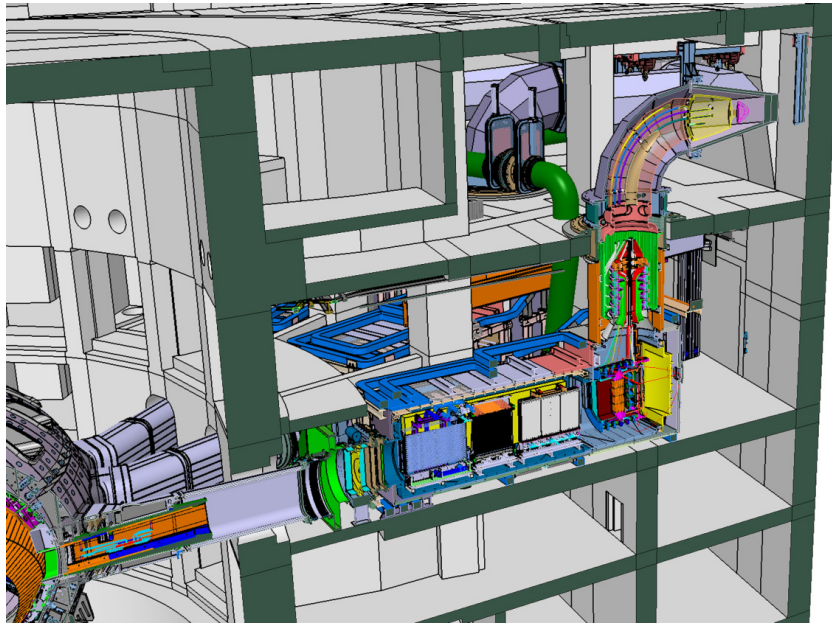
Figure 4-3 – Cross section of a neutral beam injector installed on ITER

The global power flow of the HNB is schematized in Figure 4-4 [13]. Starting from the total power at the input of the power supplies (59 MW), somewhat is dissipated on the power supplies and TL. The remaining power, partly dissipated into the accelerator, forms the output power of the ion beam (40 MW). A small part of it is lost to the neutralizer, much more into the RID. This because at 1 MV accelerating voltage more than 40% of the ion beam is not neutralized, due to the low efficiency of the neutralization process based on charge exchange in the gas cell (see also Figure 4-1). Therefore it is clear that, from the point of view of the NBI efficiency, the most critical component is the neutralizer. Alternative neutralization concepts are under study to improve its efficiency, based for example on laser detachment [17]. These advanced concepts will be developed in the Padova test facility PRIMA, described in section 4.3.
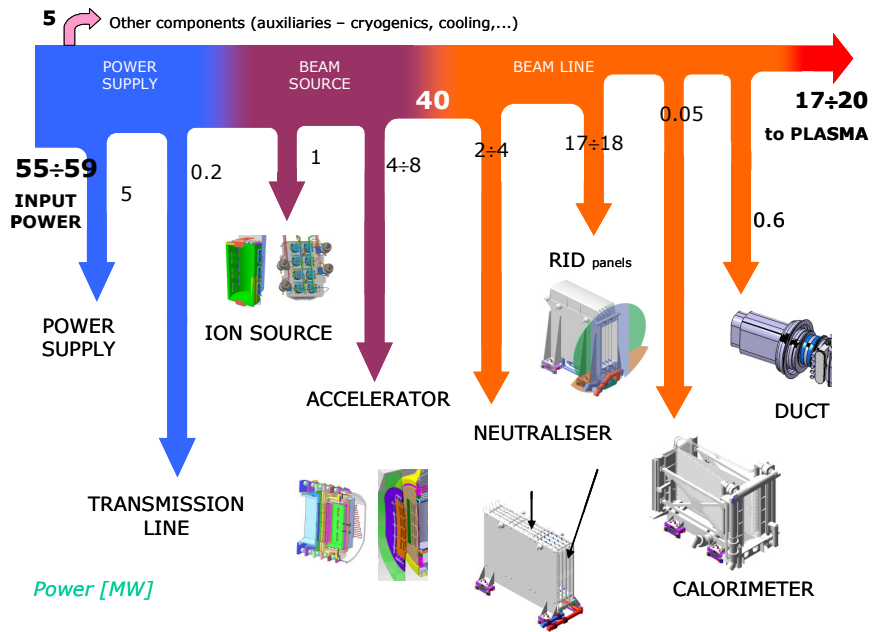
Figure 4-4 – Power flow on the ITER HNB

In the following, the main HNB mechanical components are briefly described. A more detailed description of the HNB can be found in [18].

4.2.1 Negative Plasma Source

The 2001 design of the plasma source was based on the arc source concept where tungsten electrodes, placed inside the source, are heated in order to emit electrons by thermo-ionic effect. A voltage of about 100 V sustains the arc discharge between electrodes and inner source surface, to ionize the filling gas. This concept was inspired by the classical Kamaboko ion source [19], commonly used in the neutral beam injectors operating on fusion experiments.

The present design, instead, is based on a radio-frequency (RF) ion source, and it is inspired by the RF ion source experiments operating at the Max-Planck-Institut für Plasmaphysik (IPP) in Garching [20]. A front view of the model of the ITER ion source is shown in Figure 4-5 [21]. The source can work both with Hydrogen and Deuterium, and the same beam source is used for both the HNB (Heating Neutral Beam) and the DNB (Diagnostic Neutral Beam) injectors.
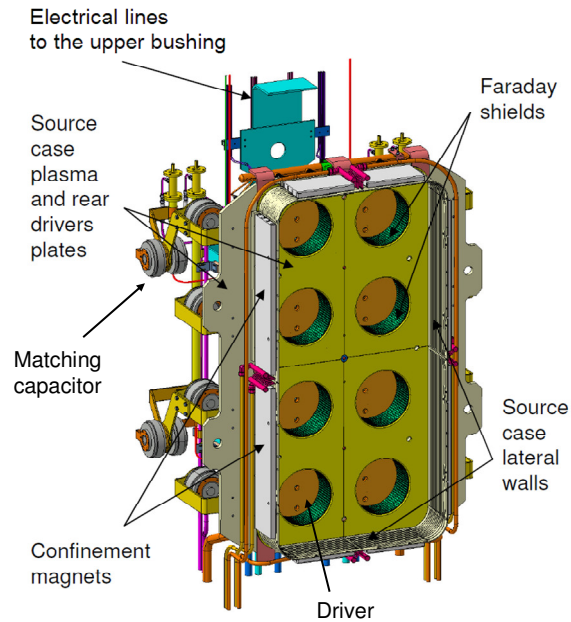
Figure 4-5 – Present design of the RF ion source of the ITER HNB, front view

In the ITER ion source, the ions are generated inside 8 drivers, each one composed by a copper coil wound around a cylinder made of Alumina, forming a cavity in which plasma is produced by RF excitation. The RF coils are grouped in couples, each one connected to three capacitors (two in series and one in parallel) to match the impedance of the RF transmission line. The fine tuning of the matching is made by the RF generator, by adjusting the RF frequency by ±10% around 1 MHz. Four RF generators are foreseen, each one rated for a maximum power of 200 kW into a couple of drivers. The RF generators are able to modulate their power during the pulse in very short times.

The plasma inside the drivers is initiated by proper tungsten starter filaments before the pulse. When a sufficient ion density is reached, the RF can sustain the plasma transferring energy by inductive effect, and the filaments can be switched off to avoid their consumption.

Small quantities (< 1 g) of Caesium are introduced into the source, as this has been found to enhance the production of negative ions. The Caesium is vaporized inside the chamber itself, diffusing from the Caesium oven and condensing on the colder wall. The Caesium is used because it acts as a catalyst of trapped electrons by ions reaction: it lowers the work function of the metal surface, facilitating the emission of electrons when ions or neutrals hit it. Most of the negative ions are produced on the plasma grid surface, which is the region closest to the extraction, where the electron stripping on the negative ions is minimized. The overall efficiency of the source is also increased by a proper magnetic field configuration, created by permanent magnets on the source body.

The ions generated inside the beam source are extracted by the voltage applied between the plasma grid and the extraction grid. The maximum extracting voltage is limited to 12 kV. Together with negative ions, also electrons are extracted. For the ITER NBI source, the target

co-extracted electron fraction with respect to negative ions shall be <0.5 for Hydrogen operation, and <1 for Deuterium operation. Having the same charge, in principle the electrons can be accelerated up to 1 MeV. To avoid their full acceleration, a set of permanent magnets are inserted into the accelerating grids, to deviate the electrons without affecting too much the negative ion beam optics. Additional electrostatic or magnetic deflectors could be conceived too.

4.2.2   Electrostatic accelerator

The NBI electrostatic accelerator is based on a Multi Aperture Multi Gap (MAMuG) configuration. Five accelerating grids at different increasing potentials are used, the last grid being referred to the NBI ground reference (the vacuum vessel). In Deuterium operation, the rated voltage across each couple of grids is 200 kV, to reach a total accelerating voltage of 1 MV. Therefore, the beam source potential with respect to the NBI vessel is up to -1 MV. A simplified CAD view of the MAMuG accelerator for ITER HNB is shown in Figure 4-6.

In the past, another concept was proposed by the European team, called Single Aperture Single Gap (SINGAP). This configuration foresaw a preacceleration grid at 60 kV with respect to the source and then a single voltage step to accelerate the ion beam up to 1 MV. Even if this configuration is simpler than MAMuG, it is much less efficient, because of the very high rate of electrons stripped and fully accelerated up to 1 MV. In the MAMuG configuration, instead, the electrons co-extracted or stripped inside the accelerator are deviated by the permanent magnets embedded in the accelerating grids and collide with the grids themselves [22].
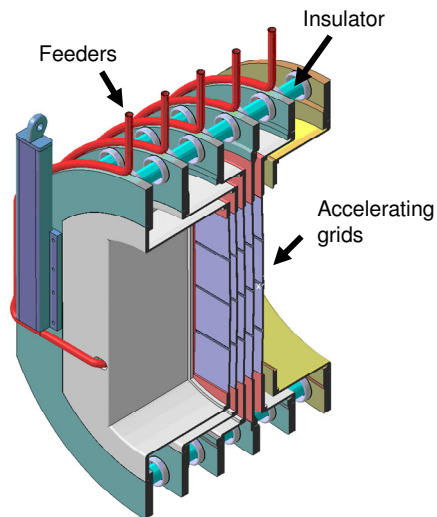

Figure 4-6 – CAD view of the MAMuG accelerator for the ITER HNB, cross section

4.2.3 Neutralizer

The neutralization of the accelerated negative ion beam is achieved by charge exchange collisions between the beam and a neutral gas (Deuterium or Hydrogen) in the neutralizer. The pressure in this component has to be high enough to provide good neutralization efficiency, but not too high otherwise the diffused gas causes beam stripping losses in the acceleration stages. The neutralizer of the ITER HNB is composed of 4 vertical channels, between which the beam flows. The neutral gas is continuously injected into the channels and removed by cryopumps, to control the pressure. A simplified CAD view of the ITER HNB neutralizer is shown in Figure 4-7. Water cooling is provided to sustain the high heat fluxes on the component.
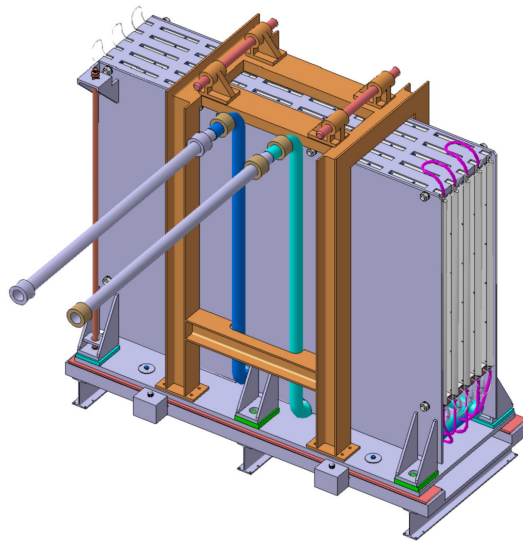
Figure 4-7 – CAD view of the ITER HNB neutralizer

4.2.4 Residual ion dump and calorimeter

At 1 MV accelerating voltage, at the output of the neutralizer about 45-50% of the ion beam is not yet neutralized. The fraction of residual ions has to be removed from the beam by the RID. In the present design, this device is based on electrostatic deflection of the charged particles. A new concept is under study, in which the steering effect is achieved by means of magnetic fields.

The calorimeter has the function to stop the beam when the valve between the HNB and the tokamak is closed, for example in case of commissioning. This device shall be able to receive all the beam power (up to 20 MW) for the overall duration of the beam pulse (up to 3600 s). Therefore the calorimeter, as the RID, is provided with water cooling channels to remove the power. In general, all the beam line components are subjected to high heat fluxes, which can reach locally peaks in the order of tens of MW/m^2, with possible modulation in time. This implies high mechanical stresses, which pose a series of technological issues.

4.2.5 High voltage bushing

The high voltage bushing has the function to separate the TL, insulated with high pressure SF_6 (6 bar) from the high vacuum of the beam vessel. At the same time, through the bushing all the electric, water and gas feeders should pass, to supply the RF ion source, the acceleration grids, the water cooling systems and the gas injection of the beam source. Neutralizer, RID and calorimeter, instead, being electrically referred to the HNB ground reference, are fed directly from the beam line vessel.

The MAMuG configuration of the accelerator implies 5 different potentials for the grids, which have to be separately connected to the respective busbars of the TL. The connections are made by tubes, passing through the high-voltage bushing, in which also the water necessary to cool down the acceleration grids flows.

Due to the very high insulation voltages, high electric fields appear inside the bushing, which have to be mitigated by properly designed electrostatic shields. The high insulation voltages also imply the overall dimensions of this device (4.7 m long) at the limit of the present technical feasibility, in particular for the big ceramic rings (diameter 1.56 m) which divide the five insulation stages. A simplified CAD view of the high voltage bushing is shown in Figure 4-8.
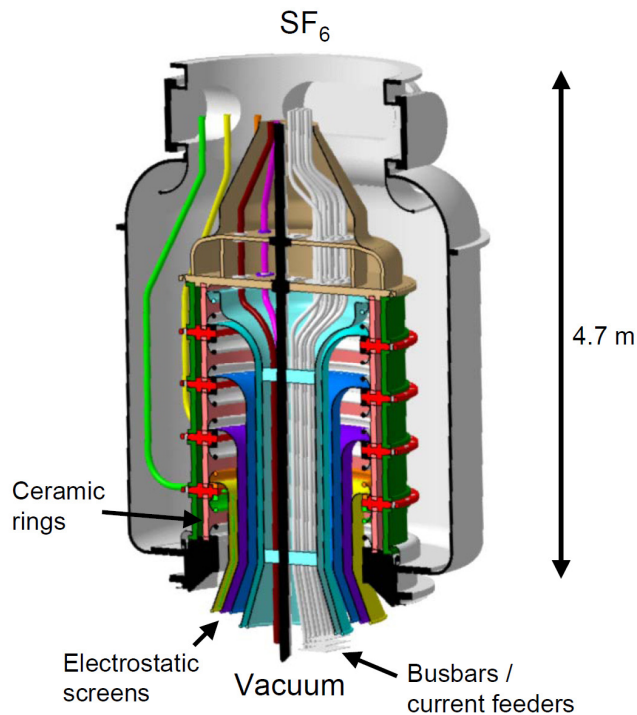

Figure 4-8 – CAD view of the ITER HNB high voltage bushing

4.3 PRIMA: the neutral beam test facility in Padova

In the framework of the activity planned by the ITER Organization for the research and development on the NBI system for ITER, considering the numerous big technical challenges to be overcome in order to achieve the required performance, it has been decided to build a test facility, devoted to experiment with two prototypes. Padova was chosen to host this test facility, called PRIMA (acronym for Padova Research on ITER Megavolt Accelerator), in the Research Area of CNR (National Research Council). The two experiments are: a full size plasma source with low voltage extraction, called SPIDER (Source for Production of Ions of Deuterium Extracted from RF plasma) and a full size HNB, called MITICA (Megavolt ITER Injector and Concept Advancement). A sketch of this test facility is shown in Figure 4-9.
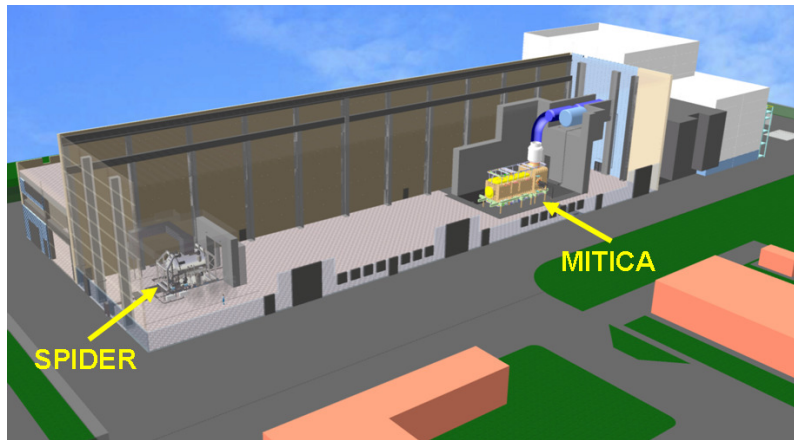
Figure 4-9 – Sketch of the PRIMA test facility in Padova

The main objective of the SPIDER experiment is to finalize, as far as possible, the development of the full ITER size ion source at full current, full pulse length. In particular, the research and development program aims at optimizing the following performances of the ion source [21]: current density, current density uniformity, ions/electrons ratio, low pressure, steady state operation and beam modulation. This should be achieved by tuning the parameters of the source, as for example: RF power, Caesium injection, temperature, current and bias of the PG, and also by optimizing some properties of the source, as for example the magnetic configuration, the PG material, the size and shape of the grid apertures and so on. Finally, the minimization of the Caesium consumption and the tolerance to the presence of impurities have to be studied.

The vacuum vessel and the ion source of the SPIDER experiment are represented in Figure 4-10. The vacuum vessel (total length 6.4 m) is mounted on rails, to be easily open. On SPIDER, the beam extracted is accelerated at 100 kV only, and the bushing and TL are designed accordingly. The TL, in particular, is air-insulated, with a double screen structure, in order to minimize the EM disturbances due to the grid breakdowns. The bushing is split in two sets of devices, the first on the top side, for the electrical connections, the second on the bottom side (split in two items), for gas and water supply.
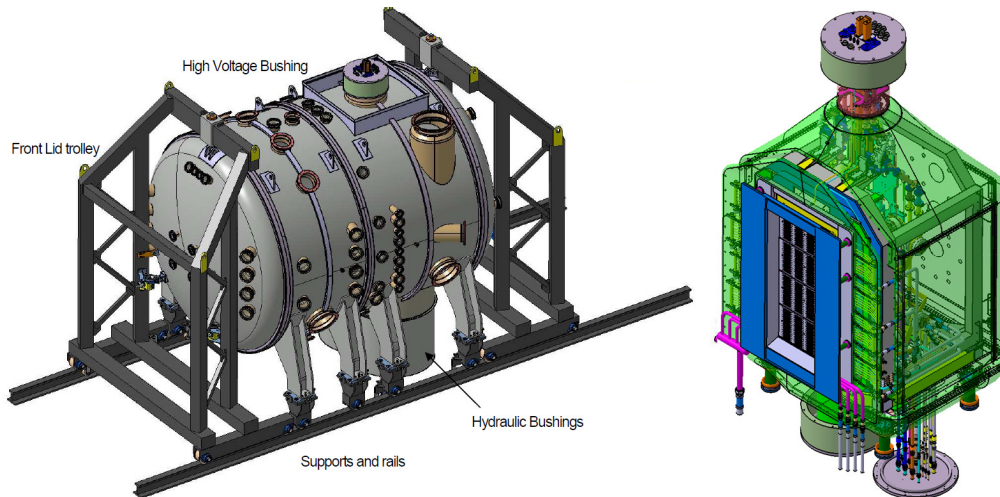
Figure 4-10 – CAD drawings of the SPIDER experiment. On the left, the vacuum vessel. On the right: the beam source

MITICA shall be as similar as possible to the ITER HNB, with the addition of more diagnostics for experimental purposes, and shall be operated up to full power, dissipating the beam energy into the calorimeter. A drawing of the MITICA injector is represented in Figure 4-11. Being the tokamak stray magnetic fields absent in the Padova site, the corresponding correction coils, foreseen for the ITER HNB, are not necessary for MITICA. Instead, residual magnetic field coils will be mounted, to reproduce as close as possible the residual magnetic field present inside the ITER HNB. This in order to verify the impact of such stray magnetic fields on beam optics. These coils are visible in the upper and lower part of the beam vessel in Figure 4-11.
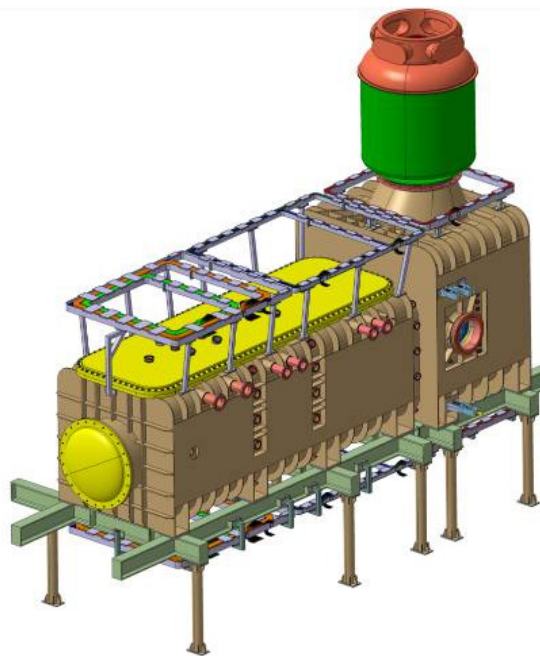
Figure 4-11 – CAD drawing of the MITICA experiment injector

5 Overview of the power supply system for the ITER heating neutral beam

5.1 Introduction

The power supplies of the ITER HNB can be divided into three main systems:

- Acceleration Grid Power Supply (AGPS), devoted to supply the acceleration grids up to 1 MV, through the high voltage TL and bushing;
- Ion Source and Extraction Power Supply (ISEPS), to supply all the ion source devices (RF drivers, plasma grid, bias, Caesium ovens, starter filaments and others) and the extraction grid; these loads are electrically referred to the ion source, which is located at up to -1 MV with respect to ground;
- Ground Related Power Supply (GRPS), to supply all the devices referred to ground, in particular the RID and the correction coils.

The overall scheme of the power supply system for the ITER HNB is reported in Figure 5-1. The corresponding scheme for MITICA is shown in Figure 5-2. The two schemes are identical, a part for the connections to the grid network, made by circuit breakers in ITER and by a switchboard at the PRIMA site. The GRPS are different too, because of the different loads in MITICA (residual magnetic field coils) and in the ITER HNB (correction coils).

In the following, AGPS, ISEPS and GRPS are briefly described. A more detailed description of the AGPS components is given in section 6.
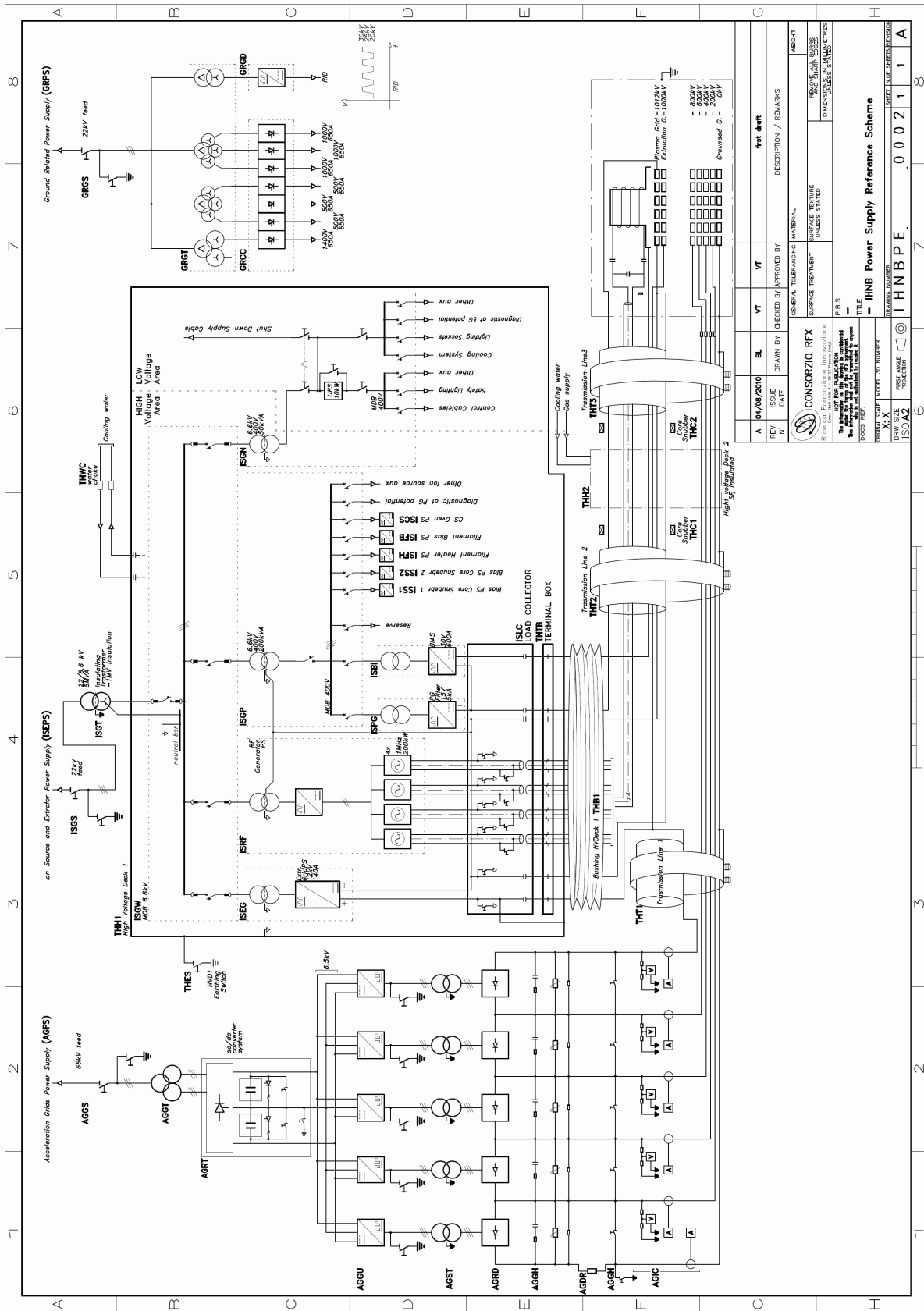
Figure 5-1– Reference electrical scheme of the ITER heating neutral beam injector power supplies
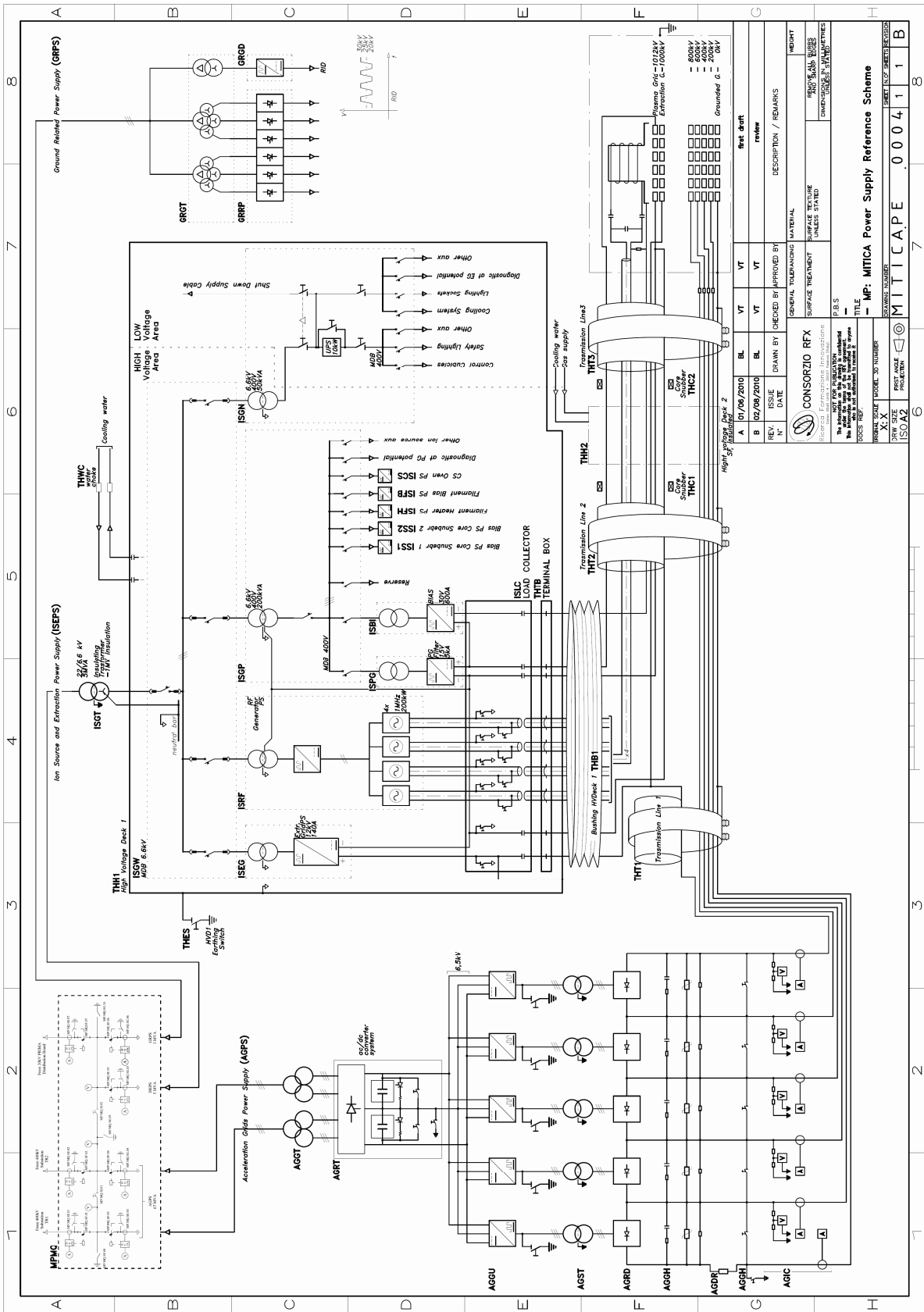
Figure 5-2 – Reference electrical scheme of the MITICA power supplies

5.2 AGPS

In ITER, the AGPS is fed by the 66 kV ITER medium voltage (MV) grid. A dedicated 66 kV circuit breaker, able to interrupt the full current, separates the AGPS from the grid in case of severe fault. In addition, a 66 kV disconnector and earthing switch can be operated when the AGPS is not in use, to remove safely the voltage to the AGPS components.

The AGPS can be divided into a power conversion stage (AGPS-CS, to be procured by the European Domestic Agency, EUDA) and a dc generator system (AGPS-DCG, to be delivered by the Japanese Domestic Agency, JADA). Five dc generators (DCG) are foreseen, each one generating the voltage across a couple of acceleration grids (200 kV for Deuterium operation). The reference scheme of the AGPS can be found in Figure 5-3.

MAMuG Configuration

step-down transformer	ac/dc converter system	dc link	Inverters	step-up transformers	diode rectifiers		
66 kV ITER grid					DCG1 dc filters	(62.8 A) 59.4 A -1000 kV	(-870 kV) H⁻ D⁻
					DCG2	(2.4 A) 3.0 A -800 kV	(-696 kV) H⁻ D⁻
					DCG3	(4.3 A) 5.3 A -600 kV	(-522 kV) H⁻ D⁻
					DCG4	(3.1 A) 3.1 A -400 kV	(-348 kV) H⁻ D⁻
					DCG5	(2.1 A) 2.7 A -200 kV	(-174 kV) H⁻ D⁻
						(50.9 A) 45.3 A 0 kV	H⁻ D⁻
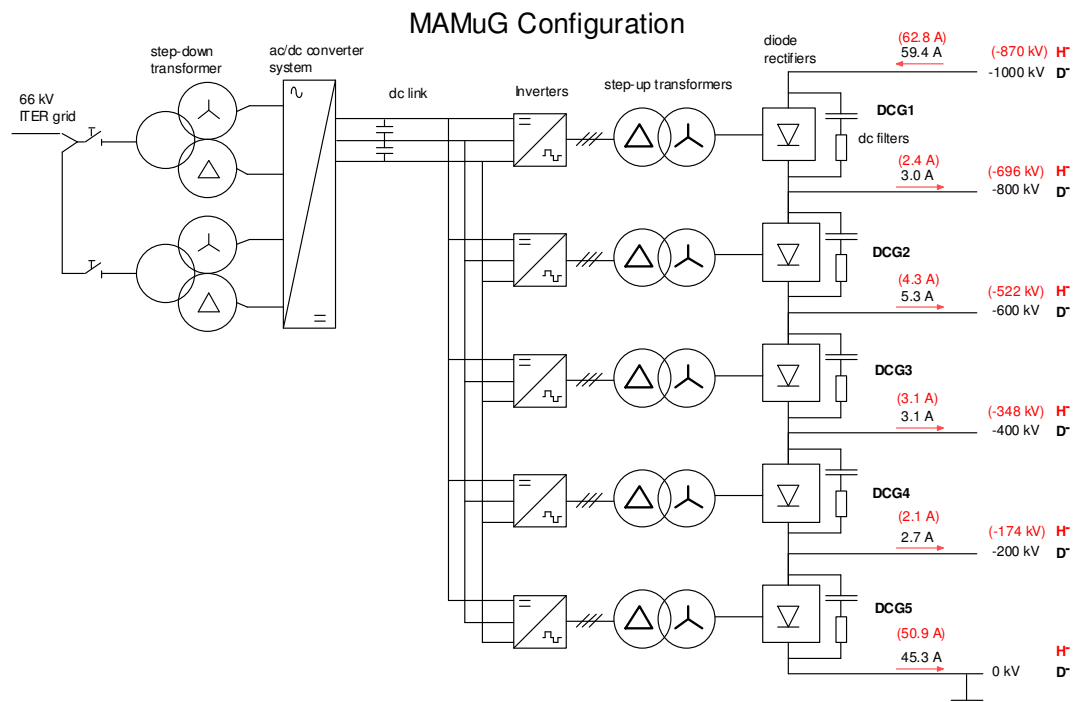
Figure 5-3 – Reference scheme of the AGPS, with the nominal dc output currents for H- and D- operation

The AGPS-CS includes a step-down transformer system, which reduces the medium voltage and produces a sufficient number of secondary voltages (phase-shifted one to another), which in turn feed a line-commutated ac/dc converter. At the output of the converter, a dual dc voltage is produced, levelled by a system of dc-link capacitor banks. This dual voltage feeds five neutral point clamped (NPC) dc/ac inverters, one for each acceleration stage. The inverters are connected at the output to their respective DCG, each one including: a step-up transformer, to increase the voltage level and to provide the required insulation between the AGPS-CS and the dc output voltage (up to 1 MV for the first stage); an high voltage diode rectifier; an high voltage dc-filter. The five DCG are connected in series at the output, to produce the required total accelerating voltage (up to 1 MV). In the MAMuG configuration, the

intermediate voltages feed the intermediate acceleration grids, which also collect part of the beam current. In principle, this scheme in compatible also with SINGAP configuration: in this case, the intermediate connections are not used.

5.3 ISEPS

ISEPS includes all the power supplies for the ion source devices and for the extraction grid. In detail, it includes:

- the Radio Frequency Power Supply (RFPS), which feeds the RF drivers of the ion source. The RFPS includes an ac/dc conversion system and four RF generators, one for each couple of drivers, rated for 200 kW on a 50 Ω matched load. The RF power is transmitted to the ion source via 4 RF 50 Ω coaxial lines, 3 1/8 inches each. The RF generators can modulate in feedback the output power in the range 10 ÷ 100%, with an accuracy of ±1%. Also the frequency can be changed in real time, in the range 0.9 ÷ 1.1 MHz (with an accuracy of ±1 kHz), to guarantee continuously the matching conditions;

- the Extraction Grid Power Supply (EGPS), rated for 12 kV and 140 A, is connected between the PG and the EG, such that the EG is polarized positively with respect to the PG. The voltage can be varied in feedback continuously from 0 to 100%, with a resolution of 100 V and an accuracy of 2%. The rise time (from 10 to 90% of the full voltage) can be adjusted in the range 500 μs ÷ 100 ms. EGPS is connected to the EG through a dedicated insulated cable;

- the Plasma Grid Filter Power Supply (PGFPS) generates the current flowing into the PG that produces the magnetic field necessary to separate the negative ions from the electrons co-generated into the ion source. PGFPS is rated for 5 kA and 15 V, and it is connected to the two vertical extremities of the PG by water-cooled copper busbars. The current is adjustable in real time in the full range with closed control loop;

- the Bias Power Supply (BPS) produces the bias voltage of the PG with respect to the source body. This voltage is proven to enhance the negative ion yield and to suppress the electrons. The BPS can generate up to 600 A and 30 V, with the possibility to regulate both the current and the voltage in real time and in feedback. It is connected to the load by two water-cooled busbars, one of them being shared with the PGFPS;

- the Bias Plate Power Supply (BPPS, not shown in Figure 5-1 and Figure 5-2). As an additional experimental tool to enhance the negative ion yield and to suppress electrons, a bias plate is foreseen inside the beam source of the SPIDER facility. The bias plate shall be positively biased against the source body. The BPPS, rated for 30 V and 150 A, generates the voltage between bias plate and source body;

- minor power supplies: the Caesium ovens PS, the starter filaments PS (heating and bias) and the bias PS for the two core snubbers of the TL.

All these power supplies are referred to -1 MV with respect to ground. For this reason, they are installed inside a dedicated high voltage deck (HVD1), insulated for 1 MV, which acts as

an air-insulated Faraday cage [23]. The very high insulation voltage requires a special design of the HVD1 and a clearance between HVD1 and building walls of at least 5 m. All the ISEPS devices, moreover, shall be fed by an insulating transformer, rated for the same insulation voltage. This transformer is installed in the same building which hosts the HVD1, it is oil type and it is provided with an air-oil bushing, 14 m tall. It provides at the secondary side an ac voltage equal to 6.6 kV, which feeds all the ISEPS by means of a metal clad board installed inside HVD1.

The HVD1 is organized in two floors, and it contains transformers, cubicles and all the electronics necessary for the ISEPS system, together with control and diagnostic cubicles. Its overall dimensions are 12 × 8 × 10 m (l × w × h). The outlets of ISEPS power supplies (cables, busbars and RF coaxial lines) are connected to the HV TL via a dedicated 7 m long air-SF$_6$ bushing. An overall view of the PS layout for MITICA is represented in Figure 5-4. In green are highlighted the TL, the AGPS step-up transformer (on the right) and the ISEPS insulating transformer (with its bushing).
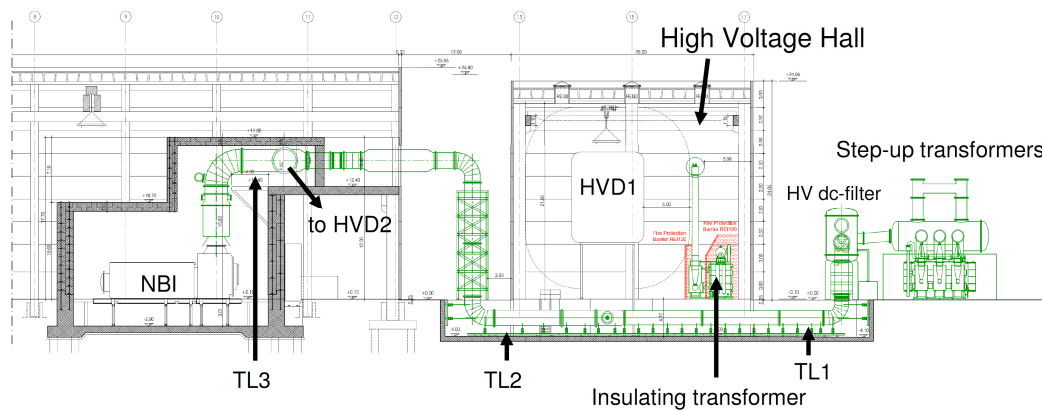
Figure 5-4 – Lateral view of the layout of MITICA power supplies. In the center, the high voltage deck 1

5.4 GRPS

GRPS is a system of power supplies referred to ground, which includes:

- the Residual Ion Dump Power Supply (RIDPS), feeding the RID. This PS generates a 25 kV dc bias voltage to polarize the RID plates, to which is superimposed an alternating voltage (sinusoidal or trapezoidal) of ±5kV at 50 Hz. The rated output current is 60 A. Both the bias and the oscillating voltages are controlled in real time, in closed control loop;

- at the ITER site, the Correction Coils Power Supply (CCPS), to supply the Active Control Correction Coils (ACCC) of the ITER injectors for magnetic field compensation purposes;

- at the PRIMA site, the Residual Magnetic Field Power Supply (RMFPS), which feeds the Residual Magnetic Field Coils (RMFC) of MITICA, aiming at generating the residual magnetic field foreseen in ITER. In total there are 7 correction coils for each

ITER HNB and 6 residual magnetic field coils in MITICA, each one to be fed by an independent PS with current feedback control loop. The main ratings of CCPS and RMFPS are presently under discussion, trying to find a compromise between modularity and optimized design of each PS.

5.5   Layout on ITER

An overall view of the layout of the ITER NBI PS system is presented in Figure 5-5. In this drawing, the PS of three HNB are shown (the PS for the third optional HNB cover the upper part of the Figure). The AGPS-CS of the first two HNB are hosted in the Building 34. The step down transformers are outdoors. Building 37 contains the HVD1 of the first two HNB, plus the high voltage deck of the DNB. Between Building 34 and Building 37, the step-up transformers are shown, outdoors. On the top of these transformers, the high voltage diode rectifiers are installed. Their outputs are series connected via branches of SF_6 TL. Other branches of the TL connect all the diode output terminals to the high voltage dc-filter tank and then to the respective neutral beam injector. Between dc-filter tank and injector, the ISEPS hosted in the HVD1 are connected to the TL by means of the air-SF_6 bushings.

Both in MITICA and in ITER, another relatively small high voltage deck is foreseen near the injector, called HVD2. It hosts the equipments to feed the cooling water and the Hydrogen / Deuterium gas required for the injector. Being the water cooling systems electrically referred to ground, the cooling water shall be fed to the ion source by a special feed-trough, which shall guarantees the 1 MV insulation between inlet and outlet. This device is included inside HVD2. The TL of each HNB is therefore divided into three sections:

- TL1, connecting AGPS to HVD1;
- TL2, connecting HVD1 to HVD2;
- TL3, connecting HVD2 to the Ion Source.
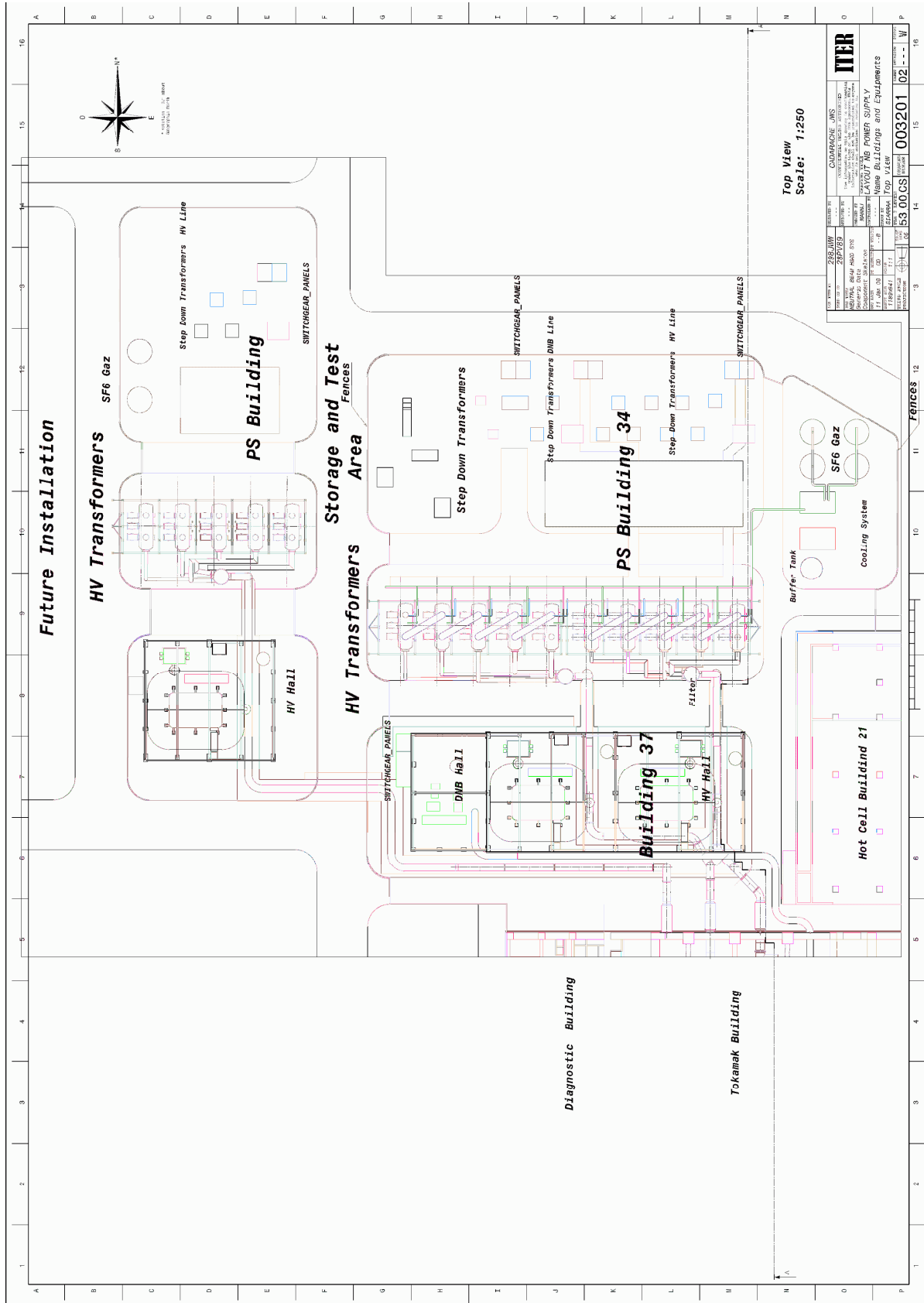
Figure 5-5 – Layout of the PS buildings and facilities of all the neutral beam injectors in ITER

5.6 Layout on PRIMA

In Figure 5-6, the layout of the MITICA PS is shown. It resembles as much as possible the ITER layout, both to reproduce in ITER the same experimental results of MITICA, and to guarantee the modularity of the PS devices to be delivered to both sites. The room dashed in red will host the AGPS-CS and the GRPS, whereas HVD1 is located in a high voltage hall very similar to Building 37 in ITER. The AGPS step-down transformers are located outdoors, on the right of the AGPS/GRPS hall in the Figure. In red and green are highlighted the AGPS step-up transformers and the GRPS transformers respectively, located outdoors. On the left, not shown in the Figure, there is the main experimental room, where the MITICA experiment is located.

Figure 5-6 – Layout of the PS buildings of MITICA and cable routings

6 Main requirements for AGPS

6.1 Operational requirements

In the following, the main operational requirements of the AGPS will be given. They are mainly consequent the parameters listed in Table 4-1, plus more detailed requirements for the ITER HNB specified in the ITER Design Description Document (DDD 5.3) [14]. The current distribution among the five DCG stages is based on estimations of the rates of ions and electrons captured by the acceleration grids at nominal working conditions. These quantities have been obtained by means of proper codes simulating the beam optics [22] and contain a certain degree of uncertainties, due to possible changes of the grid mechanical design, misalignments, impact of halo currents and so on. In Figure 6-1 and Figure 6-2 the present reference distribution of the currents among the grids is schematized, for Deuterium and Hydrogen operation respectively [25]; these currents are the same shown in Figure 5-3. The power requested to the single stages and the total power are also shown.
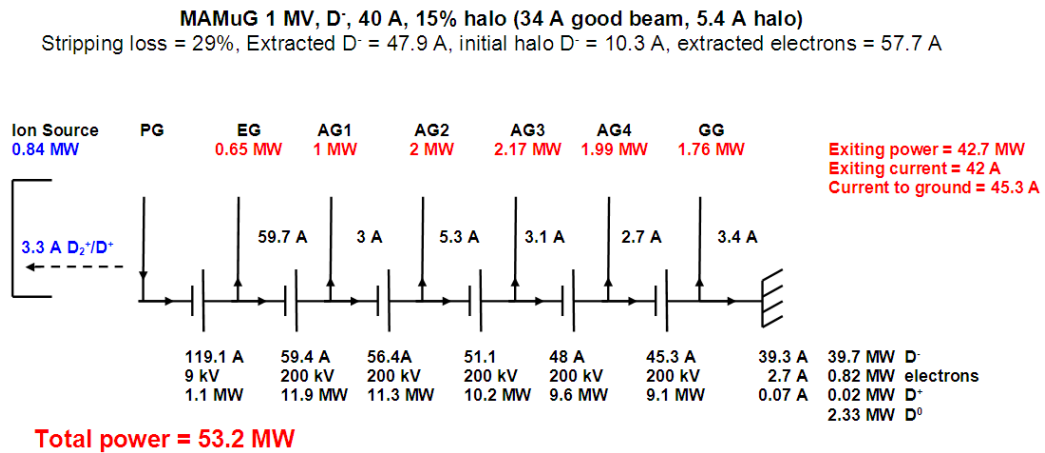

Figure 6-1 – Reference current distribution among the acceleration grids in case of nominal Deuterium operation, 15% halo current
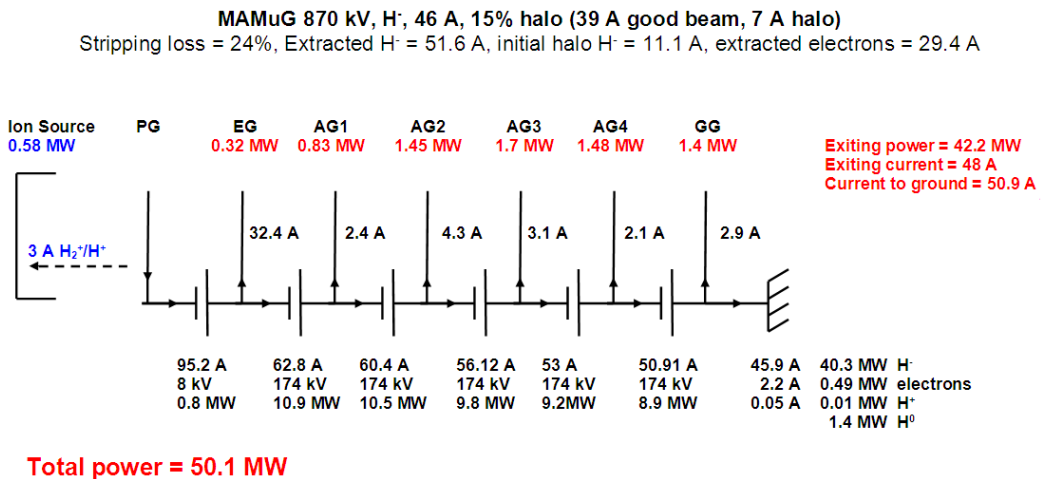

Figure 6-2 – Reference current distribution among the acceleration grids in case of nominal Hydrogen operation, 15% halo current

6.1.1 Main output electrical requirements

On the basis of the voltages required for the ion acceleration, summarized in Table 4-1, and of the estimation of the current distribution among the acceleration grids given in Figure 6-1 and Figure 6-2, the rated voltages and currents at the outputs of the AGPS-DCG have been obtained. The values are listed in Table 6-1. In agreement with IO, the output currents of the five DCG stages are increased by 5% with respect to the required currents shown in Figure 6-1 and Figure 6-2, to take into account the uncertainties in the current estimation and possible developments of the accelerator [25].

Table 6-1 – Rated voltages and currents of the AGPS-DCG stages

	D- operation		H- operation	
	Voltage	Current	Voltage	Current
DCG1	200 kV	62 A	174 kV	66 A
DCG2	200 kV	59 A	174 kV	64 A
DCG3	200 kV	54 A	174 kV	59 A
DCG4	200 kV	50 A	174 kV	56 A
DCG5	200 kV	48 A	174 kV	54 A

The main regulation and dynamic requirements of the output voltages of the AGPS-DCG are listed in Table 6-2.

Table 6-2 – Requirements for the AGPS output voltages of the AGPS-DCG stages

Parameter	Value
Voltage regulation range	20% - 100%
Voltage resolution	1 kV
Output voltage accuracy for 1 hour operation[1]	±2% with respect to the full voltage
Maximum voltage fluctuation[2]	±2.5% at flat top
Maximum voltage ripple[3]	±5%
Maximum rise time of the DCG voltage[4]	80 ms
Max. settling time[5]	50 ms
Max. undershoot at beam on[6]	15%

1. Defined as the maximum per unit error of the average DCG output voltage with respect to voltage reference, without considering the ripple and temporary voltage fluctuations. It takes into account i.e. for the precision of the DCG voltage transducers on the overall range of variation of the system temperature.
2. Defined as the maximum per unit fluctuation of the instantaneous DCG output voltage with respect to the actual average DCG output voltage, without considering the ripple. It is generally due to transient phenomena.
3. Defined as the maximum per unit oscillation of the instantaneous output voltage with respect to the actual average output voltage in steady state condition, due only to the switching action of the AGPS conversion system.
4. To reach 90% of the full DCG output voltage, with the total dc-link voltage regulated to 6.5 kV. The rise time is specified in two conditions:
1.1   with the RF power on the ion source regulated to obtain the perveance matching;
1.2   without load.
5. Defined as the time between the 90% of the full DCG output voltage and when the DCG output voltage is within the accuracy range, with the total dc-link voltage regulated to 6.5 kV.
6. Defined as the DCG voltage undershoot (without considering the ripple) with respect to the full voltage, for a ramp-up of the beam current in 20 ms from 10% to 100% of the optimum required for perveance matching.

The AGPS shall be controlled by a Local Control System that, besides allowing local control of the AGPS, shall be interfaced with the NBI-PS Control system, which controls the overall NBI power supplies (see section 8.1).

6.1.2 Operational life

The AGPS shall be designed to withstand the number and typology of pulses reported in Table 6-3.

Table 6-3 – AGPS operational requirements

Parameter	Value
Maximum pulse length	3600 s
Total number of pulses	50000 (not all at full pulse length)
Total beam on time	1.98×10^7 s
Total number of breakdowns	4.5×10^5
Duty cycle	1 shot/10 min for t < 150s 25% for 150 s < t < 3600 s
Maximum number of energizations – de-energizations during lifetime	10000
Operational lifetime	20 years

6.1.3 Normal operating sequence

In ITER, the duty of the AGPS is to produce the required acceleration voltage for the HNB, following a voltage reference sent by the ITER control system (namely CODAC, COntrol and Data ACquisition). The RF power delivered to the ion source drivers, the extraction voltage and the acceleration voltage have to be controlled simultaneously, in order to guarantee in any time the best focalization of the beam, following the perveance matching law [eq. (4-1)]. The coordination of RFPS, EGPS and AGPS is realized by the NBI-PS Control system, on the basis of the voltage reference from CODAC.

The typical operating sequence of the AGPS is the following. Before the beam initiation (i.e. the switch-on of the ion source current), the AGPS ac/dc converter shall energize the dc-link. Then, at beam initiation, the AGPS dc/ac inverters are switched-on to supply the respective DCG. The dc/ac inverters are controlled in feedback on the dc output voltage at the output of their respective DCG, to produce the required overall accelerating voltage.

The ion source RF drivers are controlled to produce the required extracted ion current, according to two possible scenarios:

- start-up in "perveance matching": when the AGPS output voltage ramps up, the power to the RF drivers is controlled to generate an extracted ion current that corresponds to 80-90% of the perveance value of eq. (4-1). When the acceleration voltage approaches the set-point, the ion beam current is further increased to reach 100% of the perveance value. Just after the turn on of the acceleration voltage, the accelerated current may not be zero, because of the residual ions extracted from the ion source. In this case, the beam current is controlled to 80-90% of the perveance value as soon as the voltage is ramped over a certain threshold;

- start-up at maximum voltage: the AGPS output voltage ramps up to the full requested voltage without beam current (therefore, the AGPS-DCG operates without load), then the beam current increases up to 100% of the perveance value.

At the end of the NBI pulse, the AGPS dc/ac inverters are switched off and the dc-link is de-energized. In normal operation, the GRPS is energized before the beam initiation and it is turned off after the end of the NBI pulse. The sequence of operation of the AGPS is reported in Figure 6-3.
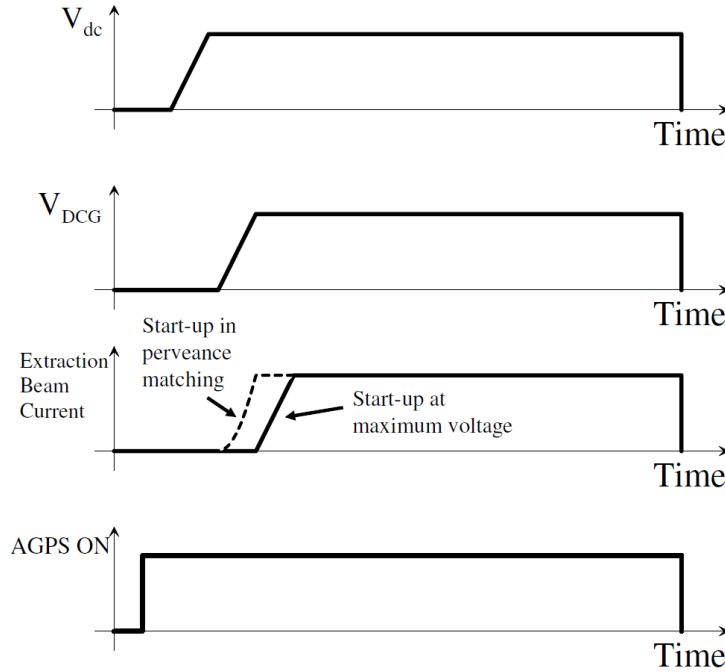
Figure 6-3 – Sequence of operation and main AGPS waveforms. Extraction beam current: in dashed line the case of perveance matching operation, in continuous line the case of voltage start-up without beam current

6.1.4 Breakdown

Due to the inherent operation of the NBI accelerator, which works close to the voltage withstand capability, frequent and unpredictable breakdowns (BD) between the acceleration grids are expected. These BD have not to be considered as faults and they have to be continuously managed by the AGPS without permanently stopping the HNB operation. From the point of view of the AGPS, these BD appear as short-circuits of the load, which result in over-currents at the output side of the AGPS dc/ac inverters. Therefore, BD shall be properly detected, in order to timely stop the inverters, the EGPS and the RFPS. This causes the extinction of the arc into the grids. After a certain time, in the order of ms, the cause of the BD is assumed to be removed, therefore the AGPS dc/ac inverters, the EGPS and the RFPS can restart, with the same sequence described in the previous section. However, it is not sure that the source of BD is really removed. If not, BD can happen again. In any case, after a maximum number of 50 consecutive BD, the AGPS is stopped permanently, and the status is recognized by the NBI-PS Control system as a fault.

GRPS is not affected by the BD and it shall continue to operate normally. The sequence of operation in case of grid BD is reported in Figure 6-4.
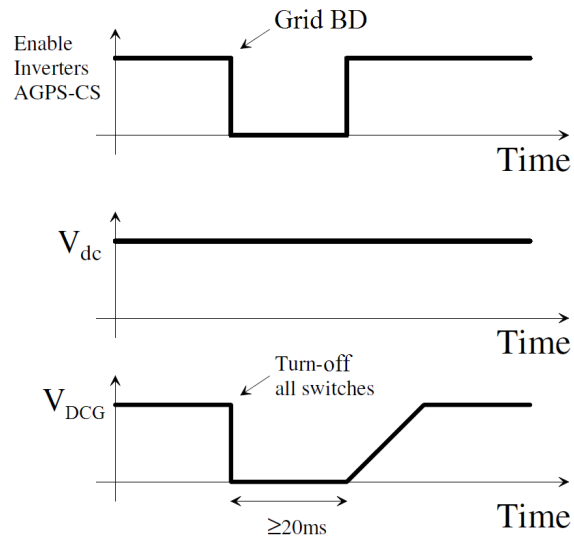
Figure 6-4 – Sequence of operation in case of grid BD

The AGPS shall be designed to withstand the stresses due to the BD. The expected total number of BD in a single pulse is reported in Table 6-4. In case a BD is detected, the AGPS dc/ac inverters shall be switched off and then they shall be ready to reapply the voltage, according to the requirements given in Table 6-4.

Table 6-4 – Operative requirements for grid BD

Parameter	Value
Maximum detection time[1]	50 μs
Maximum switch-off time[2]	100 μs
Time to be ready for restart after a grid BD	20 ms
Maximum number of grid BD for a single pulse	200 total (for the maximum pulse duration, 3600 s) 50 consecutive

1. Detection time is defined as the time between the BD and the triggering of the AGPS BD sequence.
2. The switch-off time is defined as the time between the triggering of the AGPS BD sequence and the time when all the AGPS-CS dc/ac inverter active switches are turned off.

A short circuit between the AGPS-DCG output terminals cannot be distinguished from a grid BD. Therefore, the short circuit shall be detected and managed as a grid BD by the AGPS and the NBI-PS Control system.

6.1.5   Beam-off

A beam-off (BO) corresponds to a sudden and unintentional interruption of the beam current, occurring without the contemporary and coordinated switch-off of the AGPS. The BO is equivalent to a loss of load for the AGPS, and produces an over-voltage at the output of each DCG.

To reduce the electrical stresses on the HV components and in case on other components of the AGPS, the Beam-Off event shall be properly detected and treated as a fault condition. The BO protection sequence foresees the switch-off of all the AGPS dc/ac inverters. The time

between the triggering of the AGPS BO protection and the time when all the inverter active switches are turned off shall be lower than 100 μs.

In case of beam-off, the GRPS shall not be turned off and it shall continue to supply the loads.

6.1.6 Beam modulation

The real necessity of a beam on-off modulation is not yet confirmed. This type of operative condition could be requested in support to the ITER Motional Stark Effect (MSE) diagnostic system and, in case, also in order to modulate the beam power by keeping constant the beam energy. In both cases, the modulation frequency should be sufficiently fast to avoid excessive thermal cycling of the beam-line components of the NBI.

A Design Change Request (DCR-99) has been issued in 2008 to assess the feasibility of this modulation. In support to this study, two options have been envisaged and studied by the author, as described in section 11.4 of this thesis. However, some open points should be deeply studied to complete the assessment of this working condition, as for example possible overstresses and induced EM interferences in the supplying grid.

6.2 Site conditions at ITER

This section describes the ITER site conditions that have an impact in the analyses in the scope of this thesis. In particular, the characteristics of the grid voltage, of the medium voltage and of the ITER circuit breaker for the AGPS are given.

6.2.1 400kV ac distribution system

A double 400 kV transmission line with short circuit capacity ranged from 5.6 GVA to 11.7 GVA provides electrical power to ITER. The nominal voltage of the grid is assumed 400 kV. The nominal frequency is 50 Hz. The ac power received from the grid will be distributed to the Heating & Current Drive systems at two MV levels: 66 kV and 22 kV.

Three main transformers rated at 300 MVA and 12% of short circuit impedance are installed in the pulsed ac distribution system and they energize three separated 66 kV networks. In each network, another step-down transformer rated at 50 MVA and 8% of short circuit impedance lowers the voltage down to 22 kV.

6.2.2 66kV ac distribution system

Two separated 66 kV lines of the pulsed ac distribution system are available to supply ac power to the AGPS systems of the ITER heating neutral beams. The short circuit capacity is in the range between 1.7 GVA and 2 GVA. During the operation pulse, the voltage of these lines can vary in the range 62 ÷ 72 kV (66 kV -6%/+9%). This tolerance is presently under discussion: a proposal has been made to modify it to the more standard range ±10%. Nevertheless, in this thesis the original tolerance -6%/+9% is assumed.

One 72 kV feeder circuit breaker with associated earthing switch is provided to supply the AGPS of each HNB, connected upstream the supplying cables. The main parameters of the

circuit breaker are listed in Table 6-5. The circuit breaker provides the protection function against the short circuit of the connecting cable. Moreover, the breaker can be operated on request of the AGPS in case of fault.

Table 6-5 – Main parameters of 72 kV feeder circuit breakers

Parameter	Value
Rated voltage	72.5 kV
Rated current	600 A
Short circuit rms breaking current	25 kA
Short circuit rms making current	63 kA
Total breaking time	< 100 ms
Total closing time	< 100 ms

At the other side of the cables, there is a disconnector with associated earthing switch for each HNB.

6.3   Site conditions at PRIMA

6.3.1   400kV ac distribution system

A 400 kV HV transmission line with short circuit capacity ranged from 12 GVA to 18 GVA provides electrical power to PRIMA systems. The nominal voltage of the grid is assumed 400 kV. The nominal frequency is 50 Hz.

Two main transformers rated for 50 MVA of continuous power (150 MVA of maximum peak power) and 6% of short circuit impedance are installed in the pulse power distribution system and they provide two separated 22 kV networks. The 400 kV high voltage can vary within ±10%. Therefore, a tap changer is provided for each transformer, having 25 regulation steps (-10×0.833%, +14×0.833%), with the aim to keep almost constant the 22 kV MV. MITICA and SPIDER will be fed by these MV grids. The MV is distributed with neutral insulated from earth. Also the RFX experiment [24] is supplied by the same grid, and in case from the same step-down transformer. This increases the tolerance of the MV, which is -16% ÷ +4%.

6.3.2   22kV ac distribution system

In normal operation or commissioning at nominal power the AGPS will be supplied by the 400 kV sub-station. Only for commissioning or low power operation it will be possible to feed the power supplies from the 20 kV local utility distribution board (fed by the local utility operator). The main characteristics of the 20 kV supply of the local utility operator are: nominal voltage 20 kV, short circuit current 12.5 kA, maximum power available 5 MVA.

The scheme of the MITICA MV distribution system is shown in Figure 6-5. In the MV board, a circuit breaker is foreseen for every line arriving and departing from the MV busbar. Moreover, a circuit breaker (MGQSI01) is used to allow supplying the whole system from a single line; in normal condition this circuit breaker is left open, while it can be closed to guarantee the continuity of service (at reduced power), if a fault condition occurs in one of the supplying lines.
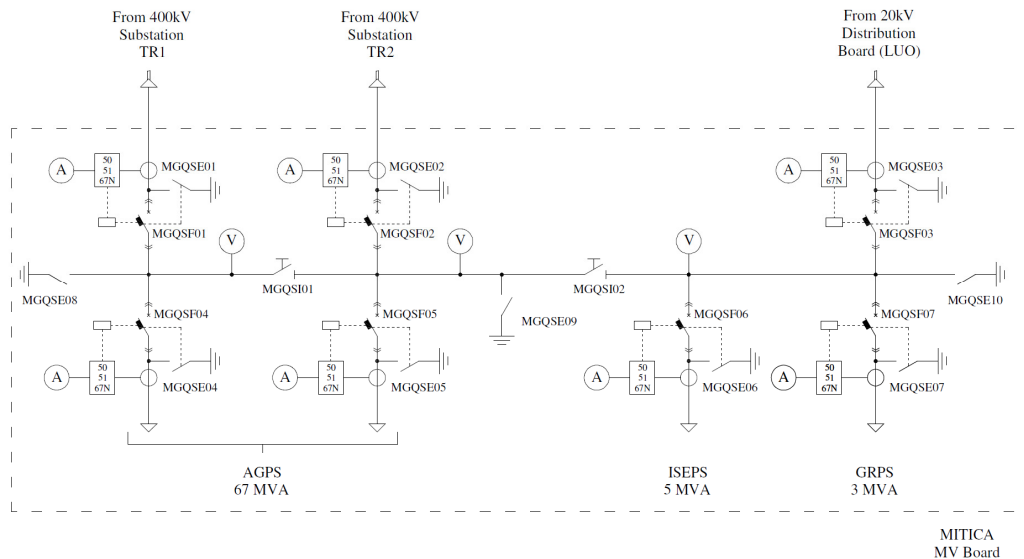
Figure 6-5 – MITICA MV distribution system

The design parameters of the circuit breakers of the MITICA MV distribution board are shown in Table 6-6. Two step-down transformers are foreseen for MITICA, to be fed through the MV circuit breakers MGQSF04 and MGQSF05. All the circuit breakers are withdrawable, so as to permit the disconnection of the line and the use of the circuit breakers as disconnecting switches. The earthing switches and the circuit breakers will be mechanically interlocked so as it is not possible to supply a line or a busbar connected to earth.

Table 6-6 – Characteristics of the MITICA MV distribution board circuit breakers and disconnecting switches

Switch	Insulation	Nominal voltage	Nominal current	Nominal frequency	Short circuit current	Breaking time / closing time
MGQSF01, MGQSF02	SF_6	24 kV	2.5 kA	50 Hz	25 kA	< 100 ms
MGQSF03	SF_6	24 kV	1.25 kA	50 Hz	25 kA	< 100 ms
MGQSF04, MGQSF05	SF_6	24 kV	2.5 kA	50 Hz	25 kA	< 100 ms
MGQSF06	SF_6	24 kV	630 A	50 Hz	25 kA	< 100 ms
MGQSF07	SF_6	24 kV	630 A	50 Hz	25 kA	< 100 ms
MGQSI01	SF_6	24 kV	2.5 kA	50 Hz	25 kA	< 100 ms
MGQSI02	SF_6	24 kV	1.25 kA	50 Hz	25 kA	< 100 ms

6.4 Electrical interface requirements between EU and JA procurements

As already mentioned in section 5.2, the AGPS-CS is part of the EUDA procurement package, whereas the AGPS-DCG pertains to the JADA procurement package. To guarantee the proper working of the overall AGPS system, a set of interface requirements between the two procurements has been formalized [25]. These parameters have been decided basing on technical considerations, regarding for example the feasibility of the step-up transformers and the minimization of the number of components of the dc/ac inverters. In particular, the turn

ratio of the step-up transformers and their short-circuit voltages shall be such to guarantee the rated accelerating voltage (200 kV for each stage) in all the operating conditions (Deuterium, Hydrogen) under stationary regime, taking into account the dc-link voltage maximum variation. The parameters listed in Table 6-7 are based on the corresponding values of [25], updated as in the latest revision of the AGPS-CS technical specifications [26]. A deeper discussion on the parameters regarding the AGPS-CS will be given afterward in this thesis, together with the assessment of the technical feasibility and of the achievement of the required performance.

The step-up transformer short-circuit inductance has been presently agreed between JADA and EUDA only for the first DCG stage. Nevertheless, in this thesis the same value will be assumed also for the other four stages.

Table 6-7- Main electrical interface parameters between AGPS-CS and AGPS-DCG

Parameter	Value
Dc/ac inverter topology	Three-phase Neutral Point Clamped
Dc-link voltage:	
- nominal value[1]	6.5 kV
- maximum variation in stationary regimes	±5%
- maximum variation in transient conditions (beam-on and beam-off)	±9%
Output voltage waveform from each dc/ac inverter	Three-level square wave with variable duty-cycle
Dc/ac inverter frequency	150 Hz
Equivalent dc/ac inverter output decoupling + stray inductance, for each phase	110 µH
Maximum output dc current component from dc/ac inverters[2]	1% of the rated output current of the inverter
Step-up transformer connections	Delta/star
Step-up transformer short-circuit inductance, measured at the secondary side[3]	0.194 H
Step-up transformer turn ratio (primary / secondary)	1/18.2

1. The reference could be set at a lower value in order to minimize the ripple amplitude of the output accelerating voltages.
2. The unidirectional component of the current could be higher than this value for time intervals less than 1 s. This component corresponds to the average value measured on 200 ms.
3. This value has been presently decided only for the first DCG stage.

7 AGPS main electrical parameters

In this section, the AGPS main electrical parameters are discussed or, in case, derived by calculation. The starting parameters either descend directly from the AGPS technical requirements, or they are consequence of technical choices taken in agreement between EUDA and JADA. The author also gave its contribution in their definition, basing on the results of calculations, described in this section, or simulations, with the models described in the next sections.

7.1 Ac/dc conversion system

In the present reference design of the AGPS [26], as shown in Figure 5-3, a step-down transformer system with 4 secondary windings feeds the ac/dc conversion system, connected at the output to the dc-link capacitor bank. The dc voltage on the capacitor bank supplies the NPC inverters of the five acceleration stages. The structure of the ac/dc conversion system shall be compatible with the NPC inverter scheme, i.e. it shall provide a central point at the output for the connection with the neutral point of the inverter. Therefore, the ac/dc conversion system shall be composed at least by two bridges connected in series at the output.

The rated value of the dc-link voltage has been proposed by EUDA basing on the available IGCT technology, in order to minimize the number of IGCT in series in the dc/ac inverters, as described in the following sections. The value presently agreed is:

V_{dc} = 6.5 kV

where V_{dc} represents the rated total dc-link voltage, i.e. the sum of the rated voltages of the two halves that compose the dc-link. The total dc-link steady-state error is ±5% (Table 6-7). In the following, it is supposed that this value includes also the control accuracy (±1% in the present assumptions).

The number of phase-shifted secondary windings of the step-down transformer system is determined by the number of pulses that the ac/dc converter should have. Of course, the more is the number of pulses, the lower is the THD of the current adsorbed from the grid network and the ripple of the dc-link voltage. Moreover, the number of secondary windings determines, for a certain short-circuit voltage of the step-down transformer, the short circuit current in case of fault.

The technical specification of the AGPS-CS [26] presently requires that at least a 12-pulse dc voltage on each half shall be available. As a consequence, the input step-down transformer system shall have at least 4 secondary windings. Previously, 2 secondary windings were foreseen for ITER, and 6-pulses dc voltage on each half was considered adequate. This is why in Figure 5-1 only 2 secondary windings are shown: the scheme has not been updated yet.

The ac/dc converter shall be based on more thyristor bridges connected in series and/or in parallel. A scheme of the ac/dc conversion system is shown in Figure 7-1. To achieve 12

pulses on each half of the dc-link, two 6-pulses thyristor bridges are put in series. The number of basic modules to be connected in series and/or in parallel and the type of semiconductor devices shall be chosen by the Supplier. Nevertheless, it is imposed in [26] that the ac/dc converter shall be composed by basic bridges connected in series. Moreover, direct connection of parallel thyristor components is preferred instead of connecting the basic bridges in parallel.

Each bridge includes all the electrical devices needed to guarantee the proper operation of the bridge itself as, for example, snubbers and over-voltage suppressors. In particular, each thyristor is individually protected by dedicated fuse.

An inductance is foreseen at the output of each half of the ac/dc converter in order to reduce the output current ripple, to improve the current sharing among the parallel-connected modules (if foreseen by the design) and to limit the current during the charge of the dc-link capacitors. Nevertheless, being the value of these inductances under the responsibility of the Supplier, depending also on the design choices on the overall ac/dc conversion system and dc-link capacitor bank (for example, the maximum charging current), they will not be included in the model of the AGPS-CS.
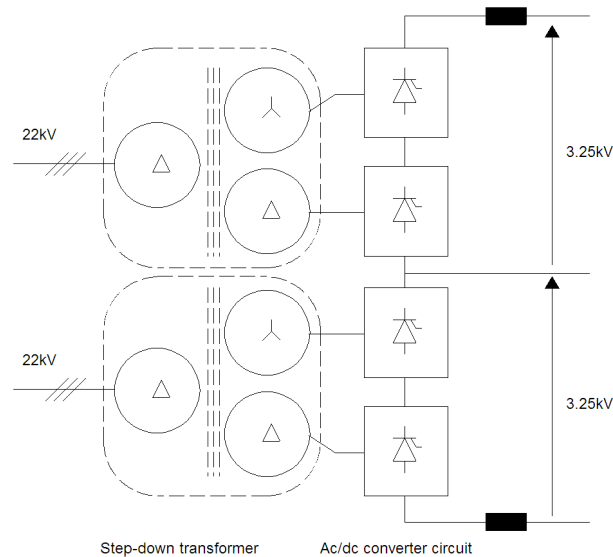
Figure 7-1 – Scheme of the ac/dc conversion system, referring to MITICA installation

In the ITER installation, the input step-down transformer shall be arranged in a single tank, which shall fit in the available area (see section 5.5). In the MITICA installation, there shall be two input step-down transformers, each one with its own tank, which shall fit in the available area (see section 5.6).

The ac/dc converter shall be able to deliver to the NPC inverters all the power that they need in the rated operating conditions, both in Deuterium and in Hydrogen operation. From the rated values of voltages and currents of the DCG reported in Table 6-1, it is possible to calculate the power requested in the worst case by the overall dc/ac inverter system.

Table 7-1 – Rated power requested by the DCG stages

	D- operation	H- operation
DCG1	12.4 MW	11.4 MW
DCG2	11.8 MW	11.1 MW
DCG3	10.8 MW	10.3 MW
DCG4	10 MW	9.7 MW
DCG5	9.6 MW	9.4 MW
Total	**54.6 MW**	**52.0 MW**

Between Deuterium and Hydrogen operation, the first one requires the highest power when all the five DCG stages deliver the rated output power. The rated output power of the ac/dc conversion system (step-down transformer and ac/dc conversion system) has been fixed in [26] to:

P_{rated} = 54.7 MW

plus the internal power losses of the AGPS-CS components connected downstream the ac/dc converter (neglected in this thesis). Basing on the rated dc-link voltage, it is possible to calculate the corresponding current when the ac/dc converter is delivering the rated power:

I_{Do} = P_{rated} / V_{dc} = 8415 A

A realistic per-unit inductive short circuit voltage of a step-down transformer rated for this power could be V_{XSC} = 10%. The exact value will be chosen in any case by the Supplier. The resistive short circuit voltage V_{RSC} is usually negligible.

Basing on these assumptions, it is possible to estimate the turn ratio of the step-down transformer system.

The maximum average value $E_{D0,ac/dc}$ of the no-load voltage at the output of the ac/dc conversion system is related to the no-load secondary winding voltage of the step-down transformer $V_{20,SD}$ by means of the following equation [27]:

$$E_{D0,ac/dc} = 1.35 \cdot V_{20,SD} \qquad (7\text{-}1)$$

For the sake of simplicity, a 12 pulses ac/dc conversion system is considered here, each 6 pulses converter supplying half of the dc-link voltage. When the system is operating at full voltage and current, each 6 pulses converter supplies the output voltage $E_{D,ac/dc}$, which corresponds to half of the dc-link voltage value V_{dc}. The relationship between $E_{D,ac/dc}$ and $E_{D0,ac/dc}$ is:

$$E_{D0,ac/dc} = \frac{E_{D,ac/dc}}{1 - \dfrac{V_{XSC}}{2} - \dfrac{V_{RSC}}{1.1}} = \frac{V_{dc}/2}{1 - \dfrac{V_{XSC}}{2} - \dfrac{V_{RSC}}{1.1}} \qquad (7\text{-}2)$$

where V_{XSC} is the per-unit inductive short-circuit voltage of the step-down transformer and V_{RSC} is the resistive one. From (7.1) and (7.2), the nominal no-load voltage of each secondary winding of the step-down transformer $V_{20,SDnom}$ can be obtained:

$$V_{20,SDnom} \cong \frac{V_{dc}/2}{1.35\left(1-\frac{V_{XSC}}{2}\right)\cdot(1-\Delta v)} \tag{7-3}$$

where the term (1-Δv) accounts for the rated minimum voltage of the distribution grid with respect to the nominal value and V_{RSC} has been neglected. By substituting the rated dc-link voltage $V_{dc} = 6.5$ kV and assuming $\Delta v = 6\%$ for the ITER site (section 6.2.2), it results:

$$V_{20,SDnom} \cong \frac{6500/2}{1.35\left(1-\frac{0.1}{2}\right)\cdot(1-0.06)} = 2696 \cong 2700 \text{ V} \tag{7-4}$$

Having $V_{20,SDnom}$, it is possible to calculate the turn ratio of the primary winding with respect to the secondary winding. Assuming a delta/delta or a star/star connection, it results:

$$n_{SD} \cong \frac{V_{MVnom}}{V_{20,SDnom}} = \frac{66kV}{2.7kV} = 24.4 \tag{7-5}$$

where V_{MVnom} is the nominal grid voltage (66 kV for the ITER site). For a delta/star or a star/delta connection, it is sufficient to multiply or divide n_{SD} by $\sqrt{3}$. For the PRIMA site, of course, the turn ratio is different, but it can be calculated with the same procedure.

The rms rated line current of each secondary winding can be calculated with the following simplified formula [27]:

$$I_{2,SD} \cong I_{Do}\sqrt{\frac{2}{3}} \cong 8415\cdot 0.816 = 6867 \text{ A} \tag{7-6}$$

in which it is disregarded the phase delay α imposed by the thyristor bridge and the load is assimilated to a constant current generator. The secondary winding equivalent short-circuit impedance of each step-down transformer can be calculated approximately as:

$$Z_{SC,SD} \cong 0.1\frac{V_{20,SDnom}}{\sqrt{3}I_{2,SD}} \cong 0.1\cdot\frac{2700}{\sqrt{3}\cdot 6867} = 0.0227 \ \Omega \tag{7-7}$$

If the resistive part of the impedance is neglected, the equivalent short-circuit inductance can be calculated as follows:

$$L_{SC,SD} \cong \frac{Z_{SC,SD}}{2\pi f} = 72.3 \text{ } \mu H \tag{7-8}$$

where f = 50 Hz is the frequency of the grid voltage (assuming a purely sinusoidal regime). The rated power for each secondary winding of the step-down transformer is:

$$P_{SD} = \sqrt{3}V_{20,SDnom}I_{2,SD} = \sqrt{3} \cdot 2700 \cdot 6867 = 32.1 \text{ MVA} \tag{7-9}$$

The total rated power of the step-down transformer system shall be therefore 64.2 MVA.

Similar calculations can be made for an ac/dc conversion system composed by two 12 pulses converters, as in Figure 7-1. The short circuit impedance would be halved and the primary/secondary turn ratio would be doubled.

To realize the AGPS ac/dc conversion system, possible thyristors available in the market to be considered could be for example the T3441N or the T2161N, both from EUPEC. The main ratings of the mentioned components are summarized in Table 7-2:

Table 7-2 – Main ratings of possible thyristors for AGPS ac/dc conversion system

Parameter	Description	T3441N	T2161N
V_{DRM}	Blocking voltage	5200 V	5200 V
I_{TAVM}	Max. average on-state current[1]	3200 A	2170 A
I_{TSM}	Max. peak non repetitive surge current[2]	79 kA	54 kA
I^2t	Max I^2t	31.0 MA^{2}s	14.6 MA^{2}s

1. Referred to half sine wave, T_C = 85°C
2. t_{peak} = 10 ms

Assuming a safety factor K_{saf} = 2.4 (as required by the Integrated Design Document, [28]), the voltage holding capability required for each rectifier supplying one half of the dc-link is (considering the maximum grid voltage, 66 kV + 9% for the ITER site):

$$V_{thy} = \sqrt{2} \cdot 1.09 \cdot V_{20,SDnom}K_{saf} = 9989 \text{ V} \tag{7-10}$$

This voltage can be sustained by two thyristors in series on each half leg of the same bridge, or by two thyristor bridges in series, each on with one thyristor on each half leg (as in Figure 7-1). The required rated average current for each phase of the rectifier is:

$$I_{thy} = \frac{I_{Do}}{3} = 2805 \text{ A} \tag{7-11}$$

which can be sustained by one T3441N or by two T2161N in parallel.

The peak fault current in case of short circuit of a rectifier leg (due to a misfiring or a thyristor fault) can be calculated for a 6+6 pulses system as follows:

$$I_{fault12} = \frac{\sqrt{2}V_{20,SDnom}}{2Z_{SC,SD}} = 84.1 \text{ kA} \tag{7-12}$$

in which it is assumed that only 2 phases are conducting at the same time and the grid voltage is equal to the nominal value. For a 12+12 pulses system (as in Figure 7-1), the applied voltage and the short-circuit impedance are halved, thus the fault current is the same. In this calculation the over-current due to the discharge of the dc-link capacitor bank on the faulted thyristor bridge is not considered, assuming that it is limited by proper output choke inductances of the ac/dc conversion system and/or by promptly acting the dc-link crowbars. Of course, when the fault occurs, the MV circuit breaker has to be operated immediately.

This fault current cannot be sustained by the thyristors of Table 7-2, therefore fuses are necessary. Considering a 6+6 pulses system, the fuse that opens should sustain two times the voltage which would appear on a 12+12 pulses system ($\sqrt{2}V_{20,SDnom} = 3818$ V, if the grid voltage is at the nominal value).

7.2   Dc-link capacitor bank

The dc-link capacitor bank is connected to the output side of the ac/dc conversion system and to the input side of the dc/ac conversion system, in order to provide reactive energy to the load of the AGPS-CS and to limit the fluctuations of the dc-link voltage during transients. The capacitor bank is rated for 6.5 kV dc nominal voltage and it is divided into two banks connected in series, with central point available to give the central potential for the NPC inverters. The central point is connected to ground and it is the reference point for all the AGPS-CS and for the primary windings of the step-up transformers.

The capacitor bank can be either single, or split among the five dc/ac inverter stages. The decision between the two options belongs to the Supplier.

The capacitance of the dc-link capacitor bank is so has to guarantee to limit the voltage fluctuations below the levels reported in Table 6-7. The following calculations give a first estimation of the minimum dc-link capacitance necessary to comply with this requirement.

At load disconnection, the firing angle of the ac/dc conversion system is increased so as to nullify the output current. The thyristors that were conducting before the increase of the firing angle keep conducting until the respective instantaneous current reaches zero. Therefore, the over-voltage on the dc-link is determined by the amount of charge flowing into the capacitor in this time interval or, from another point of view, by the energy stored in the inductances of the system (choke inductance of the ac/dc conversion system and step-down transformer leakage inductance) plus the energy coming from the grid.

Neglecting the choke inductances, the energy stored into the leakage inductances of the step-down transformer system can be calculated as:

$$E_{OFFL} \cong \frac{1}{2}4L_{SC,SD}I_{Do}^{2} = 10.2 \text{ kJ} \tag{7-13}$$

where $L_{SC,SD}$ is the short-circuit inductance of the step-down transformer (measured at the secondary side, for each winding), for a 6+6 pulses system (for a 12+12 pulses system as in Figure 7-1 the final result is the same).

Assuming that each rectifier bridge stops delivering current after a time T/6 (where T = 1 / f is the period of the grid voltage, 20 ms) from the beam-off, the energy coming from the grid can be estimated as:

$$E_{OFFgrid} \cong I_{Do} \frac{T}{6} V_{dc} = 182 \text{ kJ}$$
(7-14)

where V_{dc} has been assumed equal to the nominal value 6.5 kV and the current has been assumed constant (whereas it decreases during T/6). By knowing the maximum over-voltage ΔV_{dc} permitted on the dc-link (9% of V_{dc}), the minimum total dc-link capacitance required can be estimated as follows:

$$C_{dc} > \frac{E_{OFFL} + E_{OFFgrid}}{V_{dc} \Delta V_{dc}} = 50.6 \text{ mF}$$
(7-15)

which corresponds to about 10 mF per stage (20 mF for each half of the dc-link). This total capacitance is of the same order of magnitude of the total capacitance of the toroidal circuit of RFX-mod. This value has been used as starting point in the models to verify more precisely the dc-link voltage fluctuations during beam-off and beam ramp-up (see section 11).

To protect the dc-link against over-voltages and internal short-circuits of the dc/ac conversion system, one or more crowbars are foreseen, to be connected across the rails of the dc-link. The operation of the crowbars applies a short circuit to the upstream supplies. Hence, the crowbars must be able to handle the resulting current until the upstream short-circuit protection has operated to clear the fault. A series resistance shall be included in the crowbar circuits in order to limit the fault current to a safe level. The crowbar trigger commands may come either from the detection of faults elsewhere in the circuit, or from the measured dc-link voltage exceeding a pre-set level. In addition, a passive level-sensitive trigger (e.g. a Break Over Diode) operates the crowbars in case of over-voltage if the automatic trigger circuit fails.

The intervention of one crowbar unit triggers the intervention of all the other units and the turn-off of the ac/dc conversion system and opens the MV circuit breaker.

The capacitor bank is equipped also with safety switches for discharging, short-circuiting and earthing the bank at the end of each pulse.

7.3 Dc/ac inverters

The main aim of each dc/ac inverter is to generate the square voltage waveform to feed the primary windings of the respective three-phase step-up transformer. The primary windings of the transformers are delta connected, so the three input phases cannot be fed independently

by three single-phase inverters connected to the same dc-link. Therefore, three-phase inverters are required.

To regulate the DCG output voltage, the rms value of the primary voltage of the step-up transformer has to be modulated. To do that, the modulation index (defined as the ratio between the duration of the period in which the phase voltage is high or low and the overall period) has to be adjustable. Therefore, each dc/ac inverter has to be able to generate, on each phase, positive and negative voltages and the zero voltage. This can be done by Neutral Point Clamped (NPC) inverters. The basic scheme of a three-phase NPC inverter is represented in Figure 7-2 [29].
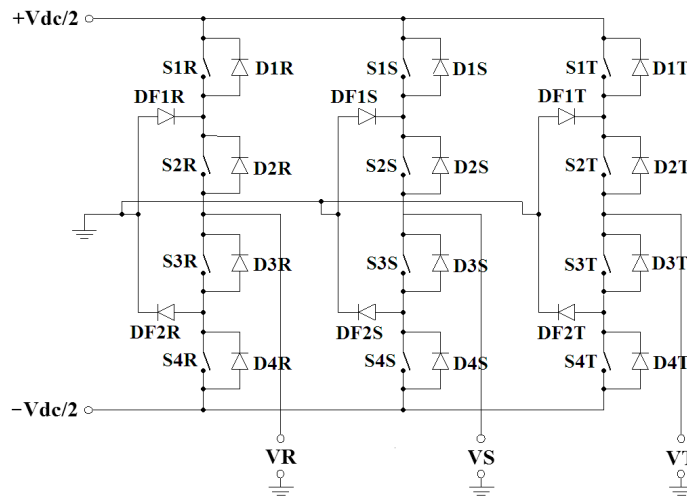

Figure 7-2 – Scheme of a three-phase NPC inverter

In this Figure, S1R, S1S, S1T, S4R, S4S, S4T are the "external active switches", S2R, S2S, S2T, S3R, S3S, S3T are the "internal active switches", D1R, D1S, D1T, D2R, D2S, D2T, D3R, D3S, D3T, D4R, D4S, D4T are the respective "anti-parallel diodes" and DF1R, DF1S, DF1T, DF2R, DF2S, DF2T are the "freewheeling diodes".

To produce the positive phase voltage at the output (+V_{dc}/2 with respect to the central point) the upper switches (S1x and S2x) are closed, vice versa to produce the negative phase voltage (-V_{dc}/2) the lower switches (S3x and S4x) are closed. To produce zero voltage, the internal active switches S2x and S3x are closed. No other combinations are permitted, to avoid to short circuit the dc-link voltage. An example of phase output voltage and phase-to-phase output voltage is shown in Figure 7-3, for a dc-link voltage equal to 6.5 kV.

Until 2008, the frequency of the output voltage waveform was not decided yet. Possible values were 150 Hz or 300 Hz. A higher frequency would have beneficial effect on the dynamic performance of the inverter and it would permit a reduction of the ripple at the output of the DCG, as it is shown afterward in this thesis. The ripple actually depends also on the HV dc-filter capacitance value. However, this capacitance is designed to limit the over-voltage in case of loss of load. Thus, once the capacitance value is set, the limitation of the ripple can be achieved by acting on the frequency value. With the analyses shown afterward in this thesis, it

has been demonstrated that the requirements in terms of ripple on the DCG output voltages (Table 6-2) can be achieved also with 150 Hz.

Once the short-circuit voltage of the step-up transformer is decided, the frequency affects also the short-circuit impedance and then the over-currents in case of short-circuit of the DCG load (for example, in case of grid breakdown). With lower frequency, for the same per-unit short-circuit voltage, the step-up transformer stray inductance is higher, thus limiting the current derivative at the output of the DCG and in the inverter switches. Also the losses in the inverter active devices are affected by the frequency of the output waveform.

In conclusion, to facilitate the design of the step-up transformers (which have to insulate for up to 1 MV), the frequency agreed between EUDA and JADA is 150 Hz [28].
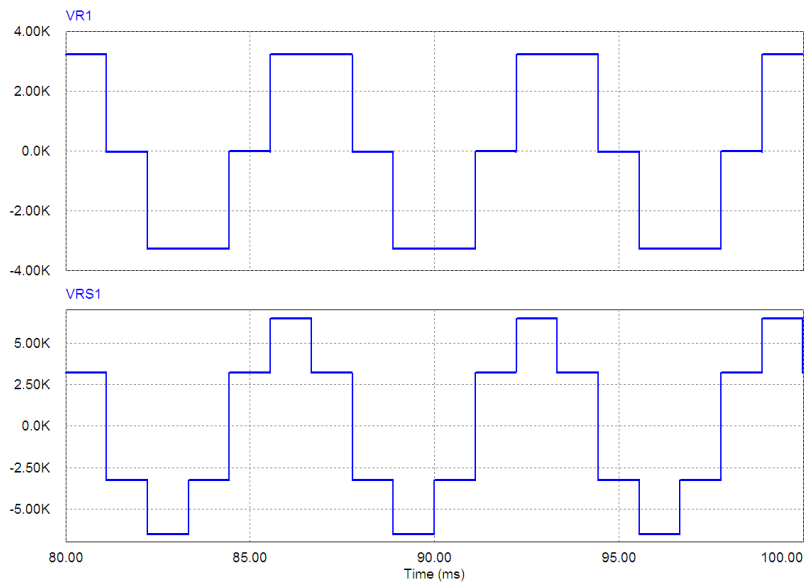

Figure 7-3 – Phase voltage and phase-to-phase voltage waveforms at the output of a dc/ac inverter stage

The dc-link voltage is one of the main design parameters of the AGPS and one of the main interface requirements between EUDA and JADA procurements. There are several reasons to keep this value as high as possible, in particular:

- the higher the dc-link voltage, the higher is the turn-ratio (primary/secondary) of the step-up transformers, and the more robust is the construction of the step-up transformer windings;
- the higher the dc-link voltage, the lower is the output current rating of the ac/dc conversion system, thus affecting the number of necessary basic rectifiers or thyristors in parallel and simplifying the dc output connections;
- the higher the dc-link voltage, the lower is the rms output current rating of the inverter, with consequent simplification of the design (for example, of the output connections).

In general, it is convenient to adopt the dc-link voltage corresponding to the highest power (voltage by current) that can be handled by a certain semiconductor technology. This permits to reduce the number of semiconductors of the converters.

Neglecting transient voltages due to the switching operation (mitigated by the snubbers of the inverter), the voltage across each switch open is equal to $V_{dcmax}/2$, so 3250 V + 9% = 3543 V in the worst case (see Table 6-7). In [26], a safety factor of 1.6 is required between the maximum repetitive peak forward blocking voltage (V_{DRM}) of the component and half of the maximum dc-link voltage. Thus, V_{DRM} shall be higher than 5670 V.

In the reference design, the main switches of the inverters are Integrated Gate Commutated Thyristors (IGCT). Presently, the only IGCT that satisfies the required V_{DRM} is the ABB 5SHY 42L6500, which is an asymmetric IGCT. The main parameters of this component are listed in Table 7-3.

Table 7-3 – Main parameters of IGCT ABB 5SHY 42L6500

Parameter	Description	Value
V_{DRM}	Blocking voltage	6500 V
V_{DC}	Permanent dc voltage for 100 FIT failure rate of GCT	4000 V
I_{TAVM}	Max. average on-state current[1]	1290 A
I_{TGQM1}	Max. controllable turn off current[2]	4200 A
I_{TSM}	Max. peak non repetitive surge current[3]	26 kA
I^2t	Max I^2t (in the same condition of I_{TSM})	3.38 MA^{2}s
$di_T/dt_{(cr)}$	Critical rate of rise of on-state current[4]	200 A/µs
$t_{d(on)SF}$	Turn-on delay time status feedback	7 µs
$t_{d(off)SF}$	Turn-off delay time status feedback	7 µs
r_T	Maximum slope resistance @T_j = 125°C	0.54 mΩ
V_{T0}	Threshold voltage @T_j = 125°C	2 V
E_{on}	Dissipated energy during turn-on @4 kV, 4 kA	2.5 J
E_{off}	Dissipated energy during turn-off @4 kV, 4 kA	44 J

1. Referred to half sine wave, T_C = 85°C, double side cooled.
2. t_{on} > 100 µs.
3. t_{peak} = 10 ms, T_J = 125°C.
4. For higher di_T/dt and current lower than 100 A an external re-trigger pulse is required.

With this rather new IGCT, it is possible to realize a NPC inverter module able to produce the full voltage with only one device for each functional switch. However, for the reasons explained afterward in this thesis, in the reference design at least two inverter basic modules are put in parallel, as in Figure 7-4. Decoupling inductances are foreseen at the outputs of each basic module, to provide the proper current sharing between the two modules and to limit the current in case of internal fault or short-circuit at the output. The value of these inductances, together with the value of the short-circuit impedance of the step-up transformer, have an impact also on the nominal voltage achieved at the output of the respective DCG. Therefore, this value is specified among the interface parameters of Table 6-7. At the output of the dc/ac conversion system, also earthing switches are prescribed, to ground the conductors of each phase.

The rms value of the output currents of the dc/ac inverters depends on the step-up transformer turn ratio (n = 1/18.2, from Table 6-7), and can be calculated as follows:

$$I_{INV} = I_{DCG} \cdot \sqrt{\frac{2}{3}} \cdot \frac{V_{20}}{V_{10}} = I_{DCG} \cdot \sqrt{\frac{2}{3}} \cdot \frac{\sqrt{3}}{n} \tag{7-16}$$

Assuming I_{DCG} = 66 A (rated current of the first DCG stage, Hydrogen operation, from Table 6-1), it results: I_{INV} = 1700 A for the first stage.

To calculate the number of inverter bridges to put in parallel for each stage, it is necessary to determine the power losses on the components corresponding to the worst operative conditions. Due to the uncommon square-wave operation of the inverter, the currents on the switches are not easy to be determined theoretically; therefore, special simulations, which are detailed in section 10.3, have been performed for two different modulation indexes (m). On this basis, the worst case has been assumed, and the number of IGCT to be put in parallel for thermal reasons is determined. However, an additional constraint is due to the maximum current that has to be interrupted in case of short-circuit of the load, for example in case of grid BD (quantified in section 11.2), which has to be lower than I_{TGQM1} of Table 7-3. This requires the use of two inverter bridges in parallel, as in Figure 7-4. In any case, the final choice about the type of solid-state devices, the number of basic bridges and the type of cooling system is left to the Supplier.
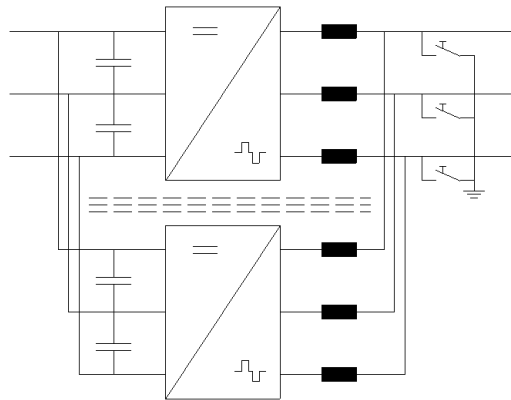

Figure 7-4 – Reference scheme of the dc/ac conversion system

7.4 Dc generators

Each DCG stage is composed by a step-up transformer, a diode rectifier and a high voltage R-C dc-filter, as shown in Figure 7-5. Their main function is to increase the ac voltage at the output of the dc/ac conversion system up to the required accelerating voltage. The primary winding connection of the step-up transformers is delta, while the secondary winding connection is star. Being the outputs of the DCG stages connected in series, the secondary side of the step-up transformer, the diode rectifier and the dc-filter of each stage have to be insulated with respect to ground (and then to the primary winding) so as to sustain the respective DCG output potential. These potentials range from -200 kV for the stage DCG5 to -1MV for the stage DCG1 (see Figure 5-3).
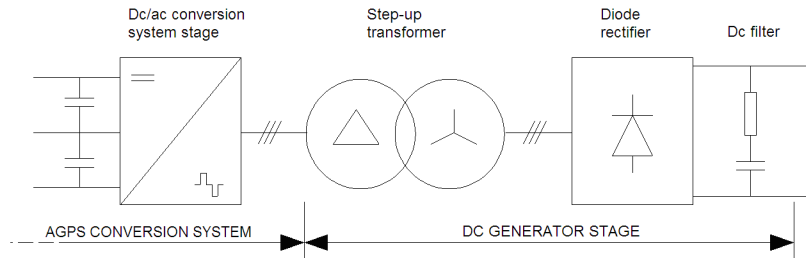
Figure 7-5 – Dc/ac conversion system stage and DCG arrangement

The step-up transformer and the diode rectifier are assembled together, as in the preliminary CAD drawing of Figure 7-6. The windings are oil-insulated inside the transformer tank, whereas the diode rectifier is insulated by SF_6 and mounted inside the cylindrical tank placed on the top of the transformer tank. The connections between the secondary windings of the transformer and the diode rectifier are realized by means of three oil/SF_6 bushings.
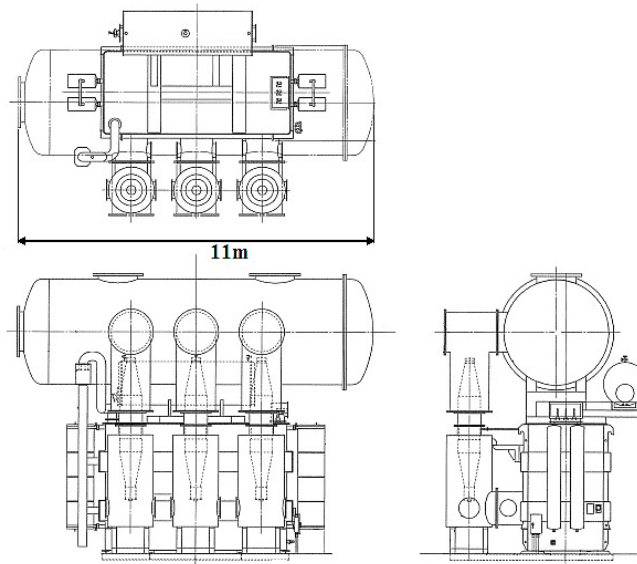

Figure 7-6 – Preliminary CAD drawing of a step-up transformer (courtesy from JAEA)

The diode rectifiers are designed to provide a 6-pulses rectified dc voltage up to 200 kV at the output. The outputs of the five diode rectifiers are put in series by means of branches of SF_6 insulated transmission line, which connect diagonally one pole of a diode rectifier to the other pole of the following rectifier, as in Figure 5-5. The pole at the lower potential of each rectifier is connected also to the high voltage dc-filter by means of a dedicated transmission line, jointed laterally to the diode rectifier tank, as in Figure 5-4.

The high voltage dc-filter is composed by five R-C filter stages, series connected and housed into a single dedicated tank. The tanks of the dc-filter and of the step-up transformers are physically connected to the local ground. The intermediate and the lower potentials of the dc-filter are available and connected on one side to the respective diode rectifier, through the

transmission line branches mentioned above. On the other side, these potentials are connected to the respective conductors of TL1.

A HV safety switch is foreseen in parallel to each R-C filter stage, to discharge the capacitor and to permit safe access for the workers to the components at the secondary side of the step-up transformers (in case of maintenance, for example). The HV safety switches are operated remotely all together at the same time and they can be operated only if the AGPS is switched off.

The primary/secondary turn ratio n of the step-up transformer has been decided in agreement between JADA and EUDA in order to achieve the nominal DCG output voltage in Deuterium operation (200 kV) when the corresponding DCG stage is delivering the corresponding rated current of Table 6-1. For example, for the first stage, assuming n = 1/18.2, the no load dc output voltage can be calculated as:

$$E_{d0nom} = \frac{2}{n} \cdot V_{dc} = 2 \cdot 18.2 \cdot 6500 = 236.6 \text{ kV} \qquad (7\text{-}17)$$

and the rms phase-to-phase secondary voltage on the step-up transformer, derived from the equivalence with a sinusoidal waveform that produces the same maximum magnetic flux in the transformer, can be calculated as:

$$V_{20nom} = E_{d0nom}/1.56 = 151.7 \text{ kV} \qquad (7\text{-}18)$$

Being L_{inv} = 110 µH the total dc/ac inverter output inductance and L_{SC2} = 0.194 H the stray inductance for each phase of the step-up transformer (Table 6-7), the total equivalent inductance seen from the secondary side is:

$$L_{tot2} = \left(\frac{\sqrt{3}}{n}\right)^2 \cdot L_{inv} + L_{SC2} = 0.303 \text{ H} \qquad (7\text{-}19)$$

The dc-link steady state precision can be assumed equal to ±5% (Table 6-7). Therefore, the minimum no load dc output voltage is E_{d0min} = E_{d0nom} · 0.95 = 224.8 kV and the average DCG output voltage achievable in this worst condition can be calculated (for the first stage, with m = 1) as [27]:

$$E_d = E_{d0min} - 6 \cdot f \cdot L_{tot2} \cdot I_{DCG1} = 207.9 \text{ kV} \qquad (7\text{-}20)$$

where I_{DCG1} = 62 A is the rated dc output current in Deuterium operation and the sinusoidal regime is assumed. Therefore, with the dc-link voltage set to the rated value, in the worst case

the nominal DCG output voltage (200 kV) can be achieved. This voltage could be achieved apparently also for a dc-link voltage equal to 6.5 kV - 6%, giving E_d = 205.5 kV, relaxing the requirement on the maximum steady state error. However, it has been considered also the fact that the modulation index cannot be exactly equal to 1, due to the dead-time between the conduction of the upper switches and of the lower switches of the same leg, to avoid short-circuit of the dc-link. After some simple calculation, considering the commutation delays of the IGCT, it has been found that a realistic maximum modulation index could be m = 0.98. By simulation, it has been verified that in the worst case m is lower than 0.98 for V_{dc} = 6.5 kV - 5%, whereas this is not true for V_{dc} = 6.5 kV - 6%, as shown in section 10.1.

The nominal resistance and capacitance of each R-C filter stage are respectively R_f = 68 Ω and C_f = 300 nF. The capacitance, in particular, has been designed to limit the over-voltage at load disconnection (in case of beam-off, for example) below 20% (maximum total voltage 1.2 MV in case of Deuterium nominal operation). The resistor is necessary to limit the peak current in case of grid breakdown. A simple calculation gives an estimation of the over-voltage on stage 1 (worst case, higher current).

$$\Delta V_{out} \cong \frac{i_{DCG} \cdot t_{delay}}{C_f} + R_f i_{DCG} \tag{7-21}$$

where i_{DCG} is the instantaneous value of the DCG output current, and t_{delay} is the time delay between the loss of load and the switch-off of all the inverter active switches. In this formula, it is assumed that, before switching off, the inverter delivers a constant current. The effect of the discharge of the stray inductances of the step-up transformer and of the inverter decoupling inductances into the dc-filter has also been neglected. Assuming for example:

- i_{DCG} = 59.4 A (nominal output current of stage 1 for Deuterium operation, Figure 6-1),
- t_{delay} = 150 μs (50 μs for the fault detection and 100 μs for the inverter switch-off, as in Table 6-4),

it results ΔV_{out} = 33.7 kV, which is lower than 20% of 200 kV. With the above assumptions, therefore, 300 nF seems a value sufficient to guarantee to limit the over-voltage below 20%. A deeper investigation, based on computer simulations and considering the peak of the instantaneous currents and all the five DCG in series, is presented afterward in this thesis.

7.5   Transmission line

The output terminals of the HV dc-filter are connected to the accelerator by means of a SF$_6$ insulated TL. As mentioned in section 5.5, the TL can be divided into three sections, namely TL1, TL2 and TL3. The TL is made of two co-axial cylinders, the inner one being at the lower potential (-1 MV) and the outer one at ground potential. Between the two cylinders, tubes at the intermediate potentials (-200 kV, -400 kV, -600 kV and -800 kV) are arranged, as shown in Figure 7-7. All these tubes and the central cylinder are supported by insulators. The maximum outer diameter of TL2 is between 2.1 m and 2.4 m. Inside TL2 and TL3, the central cylinder

contains all the cables and busbars feeding the ion source loads, which are referred to -1 MV. Inside TL3, the tubes for the intermediate potentials are duplicated, to permit the flow of the cooling water for the acceleration grids.
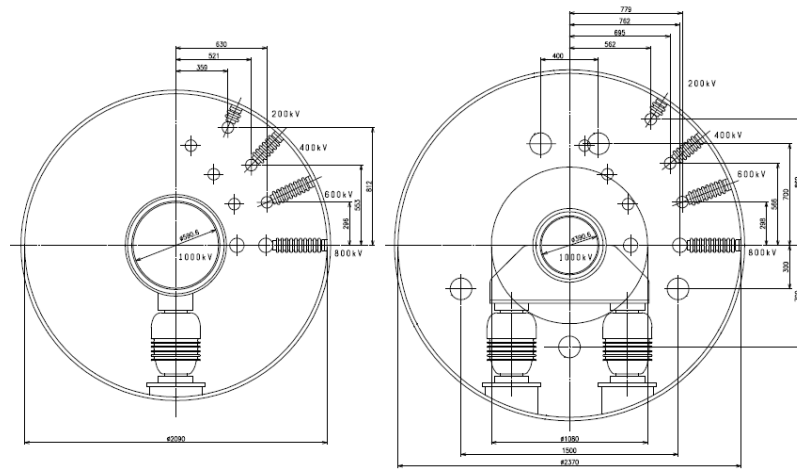

Figure 7-7 – Sketch of a section of TL2 (courtesy from JAEA)

Two core snubbers are used as surge energy adsorbing system to protect the beam source and power supply from grid BD in the accelerator. Each core snubber consists in magnetic toroidal cores and secondary circuit with a resistor. In normal operating conditions, a bias current, fed by dedicated power supplies inside HVD1, saturates the core. Then, when a grid BD occurs, the magnetic flux in the core can swing up to the value opposite in sign with respect to the bias flux. So, the bias current permits the full exploitation of the saturating flux capability of the material. The resistor on the secondary circuit helps in dissipating the surge energy due to the BD.

The outer conductor of the TL is grounded at the load side, being connected to the beam vessel. To dump the voltage oscillations across the conductors of the TL and between the outer conductor of TL and local ground, a limiting resistor R_{ret} is foreseen, the value of the resistance being presently set to 50 Ω. This resistor connects the outer conductor of the TL to the output terminal of DCG5 at the higher potential, as schematized in Figure 7-8 [28]. No other connections to ground are presently foreseen for the output terminal of DCG5.
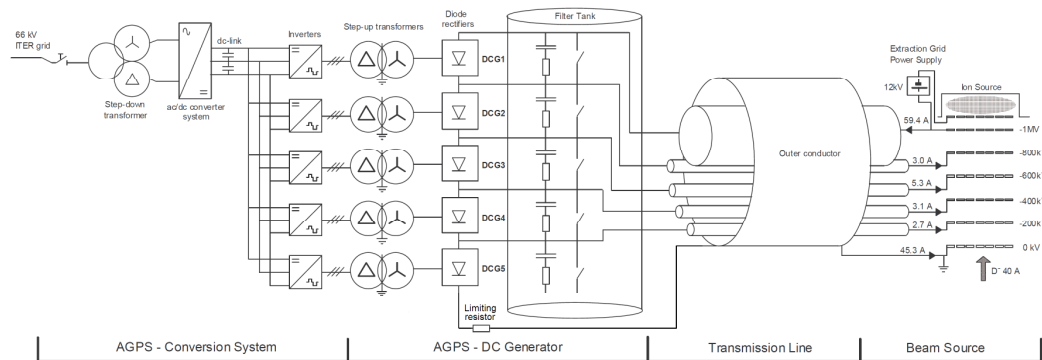

Figure 7-8 – Simplified scheme of the connections between AGPS and accelerator

Another possibility is to connect the dc-filter to the output terminal of DCG5 through the limiting resistor, and to connect the outer conductor of TL1 directly to the dc-filter, as shown in Figure 7-9 (case b). In both cases, an insulating break has to be foreseen between filter tank of the HV dc-filter (connected to local ground) and the outer conductor of TL1 (its potentials can oscillate because of grid BD). Moreover, in both cases, the terminals at the higher potential of the dc-filter and of the step-up transformer of the fifth stage have to be insulated with respect to the corresponding tank by means of proper feed-throughs, rated to sustain such voltage oscillations.
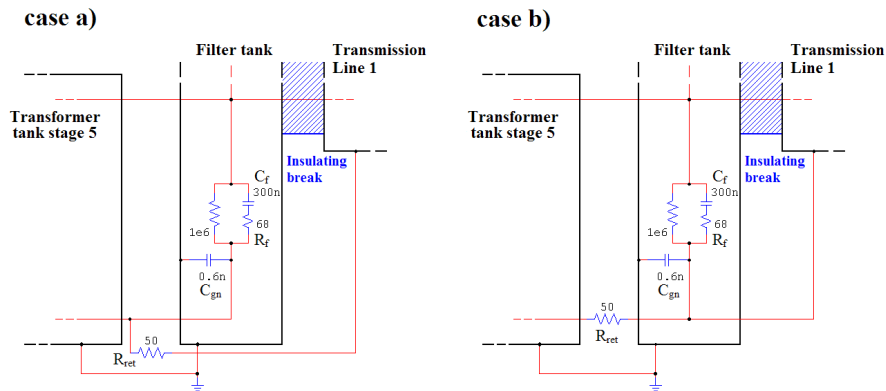

Figure 7-9 – Two possibilities to connect the limiting resistor to the return conductor of TL1

8 Design of AGPS control system

8.1 General description

The NBI plant system will be operated through an integrated management system, referred to as the NBI Control, Interlock and Safety System, that will be structured in three tiers, called NBI Plant Control System (NBI-PCS), NBI Plant Interlock System (NBI-PIS) and NBI Plant Safety System (NBI-PSS).

The task of NBI-PCS is to operate correctly and reliably the NBI. To this purpose, it will provide functions such as supervisory control, slow plant control and monitoring, fast real-time control and data acquisition for the whole NBI plant system. NBI-PIS will be responsible for the coordinated, system-wide protection of the NBI plant system, whereas NBI-PSS will guarantee the coordinated, system-wide safety of personnel and environment. The separation in three tiers reflects the ITER breakdown structure, in which ITER-CODAC, CIS and CSS are responsible for control, interlocking and safety, respectively [25].

A subsystem of NBI-PCS manages the NBI Power Supplies and it is referred to as NBI Power Supply Control Subsystem (NBI-PS Control). NBI-PS Control is interfaced with the NBI power supply units, namely AGPS, ISEPS, GRPS, TL, HVD2 and Testing Power Supply (foreseen to perform dc HV tests on site), and coordinates the integrated operation of the different PS units.

AGPS, as ISEPS and GRPS, includes its own Local Control System (LCS) responsible for reliable operation, interlocking and safety of the AGPS itself. These subsystems are located on proper Local Control Cubicles (LCC).

Figure 8-1 shows the structure of the real-time control system. The cyan blocks represent the elements of NBI-PS Control, the yellow blocks are part of the LCS (of AGPS, ISEPS and GRPS), and the white parts represent the power sections. To simplify the scheme, the power sections are integrated with the respective LCS in single blocks.

The NBI-PS Control produces in real-time the required reference waveforms to drive AGPS, ISEPS and GRPS.
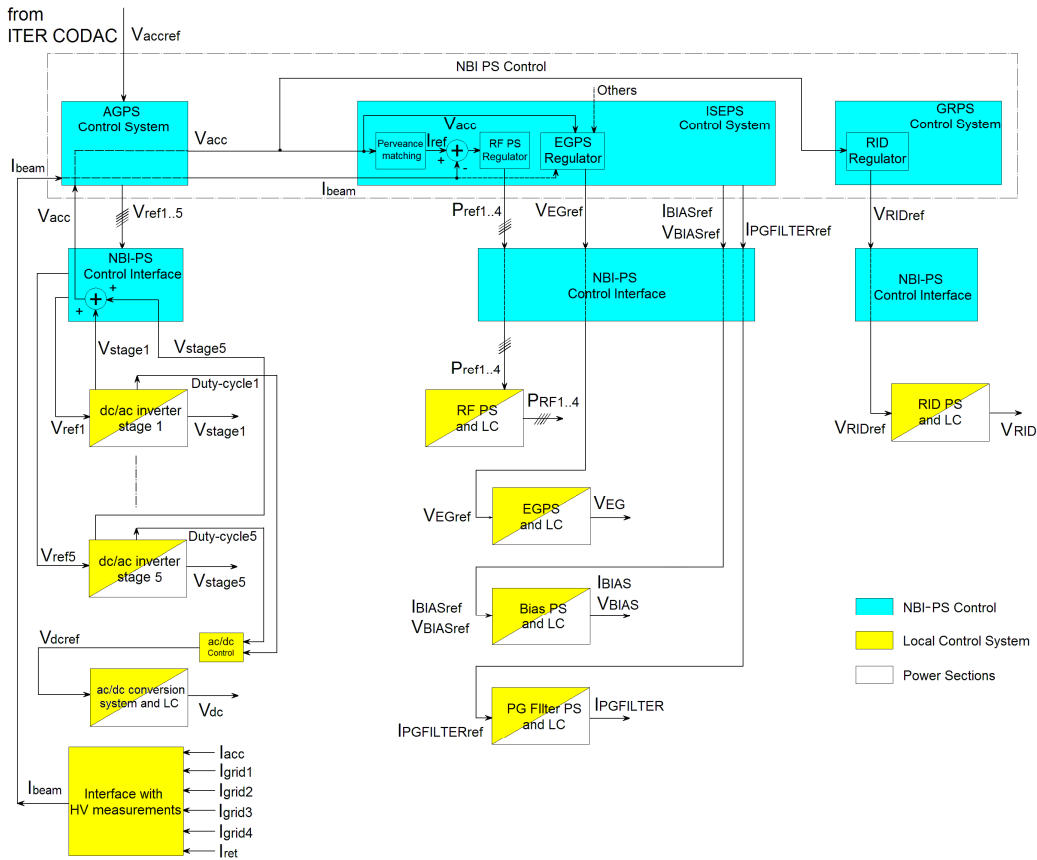
Figure 8-1 – NBI real-time control structure

A signal representing the overall accelerating voltage V_{accref} originating from ITER CODAC is distributed through NBI-PCS to NBI-PS Control. Basing on this signal, NBI-PS Control produces five voltage references $V_{ref1},...,V_{ref5}$ for the AGPS LCS, which in turn generates the duty-cycles and then the firing commands for the five dc/ac inverters. The output accelerating voltage of each DCG (or the potential of the respective output terminal with respect to ground, see next sections) is compared with the reference and the error is used in the local feedback loop to control the respective dc/ac inverter.

In general, all the parameters of the PID controllers of NBI-PS Control system are adjustable by the operator out of the pulse.

During normal operation, the measured total accelerating voltage is used to obtain the reference signal for the beam current, following the perveance matching law [eq. (4.1)]. This signal, compared with the actual beam current, is processed inside the NBI-PS Control to generate the signals representing the RF active powers requested on each RF driver of the ion source. The RF active powers requested are the input for the RF generators control cubicles, which control in feedback the active power delivered to each RF driver.

The total accelerating voltage, together with other measurements as for example the output beam current, is also used by NBI-PS Control to produce the reference voltage waveforms to drive the EGPS in feedback control loop. The proper strategy to control the EGPS will be

clarified during the experimental period of the NBI. Also the voltage reference for the RID PS is provided by NBI-PS Control on the basis of the total accelerating voltage.

As described afterward in section 8.4, the reference of the dc-link voltage is generated as a function of measured inverter duty-cycles by the AGPS LCS.

In general, each power supply can be operated locally (for maintenance, troubleshooting etc.) o remotely through NBI-PS Control system.

Each power supply has the capability of detecting internal faults and of protecting itself against them. Moreover, if a fault occurs in a power supply unit requiring coordinated protective actions to avoid damage on other PS or NBI units, a request is sent to NBI-PIS that will dispatch the necessary protection commands. If a normal or abnormal condition of a power supply unit requires coordinated actions to protect personnel or environment against hazard, this must be performed through NBI-PSS that dispatches the required protection commands. In case of a fault, NBI-PS Control performs protection or corrective actions in response to the commands generated by NBI-PIS or NBI-PSS.

In normal operating condition, the relevant AGPS quantities to be controlled are the dc-link voltage and the dc output voltage of each DCG. These quantities have to be controlled in combination in order to fulfill the requirements in terms of ripple of Table 6-2, as described afterward in this section.

8.2   Control of dc-link voltage

The dc-link voltage is controlled in feedback in real-time by the AGPS LCS. The two halves of the dc-link voltage are controlled separately by two voltage control loops, as required in the technical specifications [26]. A current limitation loop is also implemented, which take over the control whenever a limitation of the output current of the ac/dc converter is necessary, on the basis of a settable threshold.

The ac/dc converter regulation is enabled by a specific command "Charge ON" coming from the NBI-PS Control. If this is removed, the ac/dc conversion system is switched off.

The dc-link voltage shall be regulated in order to satisfy the requirements of Table 6-7. For each half of the dc-link, the dc-link voltage set-point cannot exceed 3250 V and it is settable with a resolution of 50 V.

8.3   Control of dc output voltages

The regulation of the output voltage of the single DCG stages is performed by the dc/ac inverter regulators by varying the duty-cycle of the respective square wave (modulation index).

Each dc/ac inverter has its own regulator, which implements three different control methods:

1. dc/ac inverter rms output current closed loop control;
2. modulation index open loop control;
3. DCG output voltage closed loop control.

The choice among one of these control methods can be performed only out of the pulse. In any case, whatever is the control scheme in force, the maximum rms output current delivered by each dc/ac inverter is limited in real-time to a certain settable threshold (lower than the respective rated rms current).

In normal operating conditions, the dc/ac conversion system is operated remotely and the DCG output voltages are controlled independently on the basis of the voltage references sent by NBI-PS Control system. These voltage references could represent either the desired output voltage of each DCG stage, or the desired potential of each DCG output terminal with respect to ground. The choice depends on the actual measurements available on the DCG, pertaining to the JADA procurement. The regulation is performed by varying the modulation index of each dc/ac inverter stage. For each DCG stage, the respective output voltage (in case determined as the difference of the relevant grid voltage measurements with respect to ground) is compared with the corresponding reference, and the difference is the input of a dedicated PID regulator, which gives at the output the proper modulation index necessary to nullify the voltage error.

The carrier waveform frequency for the regulation is 150 Hz, as already mentioned. In default conditions, the carrier waveforms of the five dc/ac inverter regulators are synchronized in phase. Anyway, it is be possible to select a phase shift between the carrier waveforms inside the range $[0°,360°]$.

The rms output current control loop is necessary only when the AGPS-CS is operated locally for commissioning purposes on the dummy loads. The open loop control allows controlling directly the modulation index of each dc/ac inverter stage, by means of external reference signals or values sent locally.

The output voltage regulation is enabled by a specific command generated by the NBI-PS Control (e.g. "AGPS ON"). If this is removed, the switches of the dc/ac inverters are turned off with the suitable sequence.

8.4 Control of output voltage ripple

In normal operation, the regulators of the ac/dc conversion system and of the dc/ac conversion system shall work together in an integrated control scheme aimed at controlling the DCG output voltage, limiting at the same time the output voltage ripple under the value specified in Table 6-2. A possible scheme for the overall control strategy is given in Figure 8-2. Depending on the operative conditions, to minimize the ripple of the DCG output voltages the dc/ac inverter stages have to operate at a certain modulation index m_i (i = 1..5). A dedicated closed loop regulator, called "Ripple controller" in Figure 8-2, has been proposed to regulate the dc-link voltage in order to operate at the optimal value of m_i. The "Ripple controller" receives as input the modulation indexes m_1, m_2, ..., m_5 and determines the maximum value m. This value is compared with the reference m_{ref} (adjustable out of the pulse) and the difference is the input of a dedicated PID regulator. The output of the "Ripple controller" is subtracted from the dc-link voltage set-point of the ac/dc conversion system. In this way, if the

maximum modulation index is lower than m_{ref}, the dc-link voltage set-point is decreased in order to increase the modulation indexes. Vice-versa, if the maximum modulation index is higher than m_{ref}, the dc-link voltage set-point is increased.
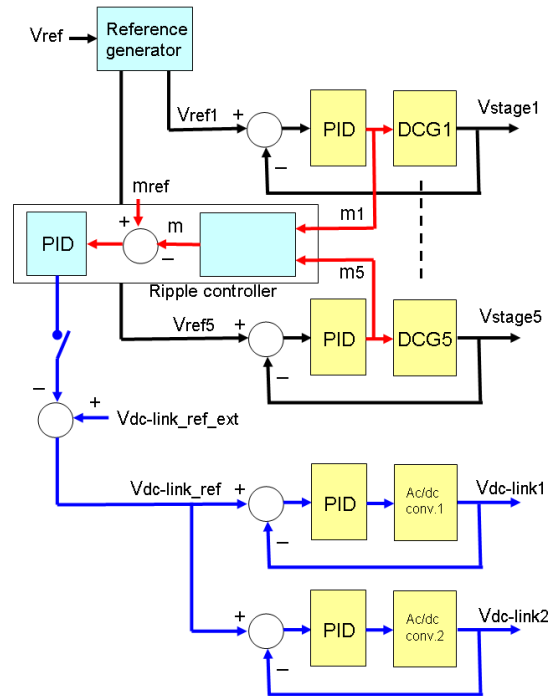

Figure 8-2 – Suggested scheme for the control of the output voltage ripple

The dynamic response of the "Ripple Controller" has to be so slow to do not interfere with the dynamic response of the other feedback controllers of the AGPS-CS. In particular, extra oscillations and overshoots in the dc-link voltage and DCG output voltages shall be avoided.
Another possibility to minimize the ripple could be to generate the dc-link voltage reference in open loop, as a function of accelerating voltage and beam current requested.
The "Ripple controller" function can be also disabled, offline. Moreover, the "Ripple controller" function has to be automatically disabled during the start-up of the AGPS (initial charge of the dc-link capacitor bank and ramp-up of the DCG output voltages). The time duration of the period during which the function is disabled is selectable offline by the operator, inside a proper range. Finally, the "Ripple controller" has to be disabled for a pre-fixed time also after a grid BD, as described afterward in section 8.6.

8.5   Control of unidirectional component of the currents on step-up transformers

Unbalances of the dc/ac conversion system output voltages may cause unidirectional current flowing into the step-up transformers, resulting in undesired magnetization of the core. If the magnetizing flux exceeds a certain threshold, the magnetic core of the step-up transformer could saturate, causing mechanical and electrical overstresses in the device and over-

currents at the inverter outputs. This is the reason why the unidirectional currents have to be limited below the value of Table 6-7.

The unidirectional current components are caused by undue dc voltage components at the outputs of the dc/ac inverters. This could happen, for example, because of asymmetries in the triggering commands of the IGCT or in the commutation and conduction characteristics of the devices, or because of the dc-link voltage ripple. Conversely, as it is easy to verify, stationary voltage differences between the two halves of the dc-link do not imply dc components on the phase-to-phase voltages at the output of the inverters.

It is easy to see that, to minimize such unidirectional currents, a dedicated control system has to be implemented. In fact, in steady-state conditions, if a dc voltage is applied for example between two phases of a the step-up transformer, the dc current is determined only by the resistance of the transformer windings. In particular, the dc resistance of the primary windings of the step-up transformers has been estimated by JADA in the order of 4 mΩ ÷ 6 mΩ. Therefore, assuming R_{pri} = 10 mΩ as the total dc resistance at the output of the dc/ac inverter (for each phase, including the cables), to comply with the requirement of Table 6-7 the dc voltage component should be lower than:

$$V_{dc\max INV} \cong 2R_{pri} \cdot \sqrt{2}I_{INV} \cdot 0.01 = 0.48 \text{ V} \qquad (8\text{-}1)$$

for the first stage (I_{INV} = 1700 A). In this formula, it is assumed that the 1% limit of Table 6-7 is referred to the peak value of the rated dc/ac inverter output current. The resulting maximum dc voltage component corresponds to 0.0073% of the nominal dc-link voltage V_{dc} = 6.5 kV. This is technically unfeasible, also by providing a feedback control of the dc voltage component. For example, 0.5 V corresponds (at V_{dc} = 6.5 kV) to a systematic error in the triggering of one IGCT of 1 µs only (where the switching period is 6.7 ms).

In conclusion, to keep the unidirectional component of the current lower than the limit of Table 6-7, a direct feedback control of this component is mandatory. Alternatively, it has been proposed to feedback control the effect of this current, so the magnetizing flux on the step-up transformers, which should be measured by proper sensors. At present, the details of the unidirectional current control loop are not yet decided.

The control of the unidirectional component poses a set of requirements also on the switching strategy of the AGPS dc/ac inverters. For example, during the ramp-up of the DCG output voltages, the voltage waveform applied to each primary winding of the step-up transformers shall be pulse-by-pulse symmetrical; this means that the duty-cycle shall be the same for the positive pulse and the negative pulse. Moreover, after a grid BD, the first voltage pulse applied by the dc/ac inverter shall have opposite sign with respect to the last pulse delivered to the step-up transformer. These two provisions permit to reset the magnetizing current some time after the grid BD, preventing any cumulative effect for the unidirectional component of the current for consecutive BD. An example of this strategy is shown in Figure 8-3.
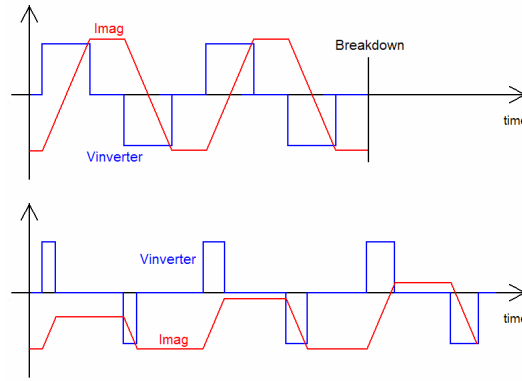
Figure 8-3 - Example of voltages applied to a primary winding of a step-up transformer before and after a grid BD event (in blue), and corresponding magnetizing current (in red)

8.6 Grid breakdown detection and intervention

As already mentioned, during normal operation of the NBI, frequent grid BD occur, which correspond to short-circuit of the load. These grid BD events cannot be considered as faults, therefore they do not have to interrupt the NBI operation. The grid BD events and the beam-off events are managed by a supervisor block called "Breakdown & Beam-Off Detector" (BBD), which coordinates the protective actions among the AGPS and the EGPS. In particular, the supervisor block switches off all these power supplies as quickly as possible, in order to satisfy the requirements of Table 6-4.

The BD event is detected by the "BD detectors" of AGPS and EGPS LCS, making use of the DCG output voltage measurements and the EGPS output voltage measurement. In particular, if one or more DCG voltage measurements fall below a threshold while the "AGPS ON" signal is active, then the AGPS LCS shall trigger the BD sequence for the AGPS. As a consequence, all the gating signals of the AGPS dc/ac inverters are stopped. At the same time, the BD event is communicated to the BBD through a dedicated digital signal and it is properly logged on the HMI (Human Machine Interface) of the LCS. The BBD communicates the BD event to all the AGPS and EGPS LCS, which take the necessary protective actions. At the same time, also the NBI-PS Control system is informed of the BD event. As a consequence, it forces to zero the voltage references for the AGPS dc/ac inverters and for the EGPS; at the same time, it forces the power references provided to the RF PS to a level from 10 to 20% of the rated power, as previously preset by the operator. The same protecting sequence is triggered if the EGPS output voltage measurement falls below a threshold while the "EGPS ON" signal is active. In addition, the BD event could be detected also by using the DCG output current measurements: if such measurements exceed a threshold while the "AGPS ON" signal is active, AGPS LCS triggers the BD protecting sequence as well. The same is possible with the EGPS output current measurements.

If the grid BD event is properly detected, the NBI PS system has to be able to restart within the time indicated in Table 6-4, without requiring the intervention of the NBI-PIS. The stopping of the gate commands of the AGPS dc/ac inverters and of the EGPS is maintained for a prefixed time (10 ms typical) by the respective LCS. After this time interval, proper signal references

are generated by the NBI-PS Control, in order to produce the electrical waveforms needed to restart (see Figure 6-4). Figure 8-4 summarizes the recovery logic for a BD event in normal operating conditions.

During all the protecting sequence, the dc-link voltage has to be maintained at the reference voltage value, which is the same as before the BD event. In particular, the "Ripple controller" function shall be disabled during the BD protecting sequence and the "Ripple controller" output shall be frozen for a pre-fixed time, lasting after the completion of the accelerating voltage ramp-up.
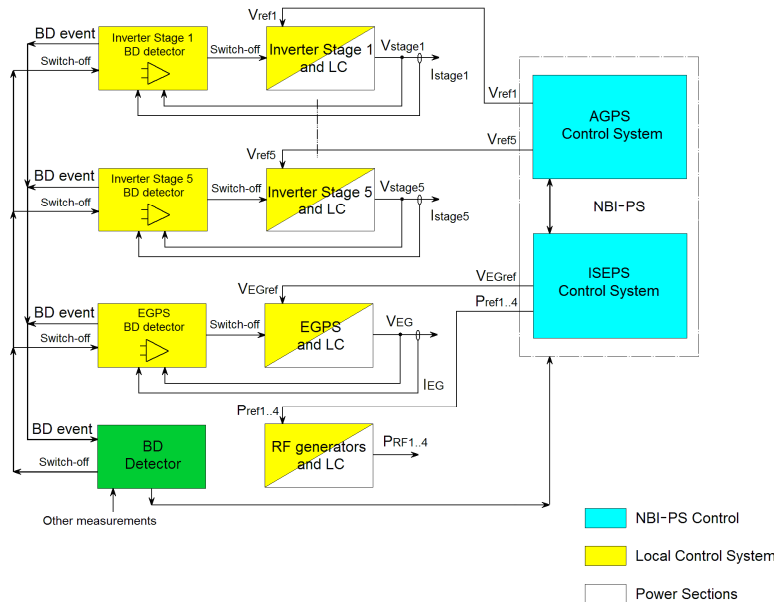
Figure 8-4 – Protection logic for a grid BD event

If the BD detection made by BD detectors fails, a second level of intervention is granted by the over-current detectors at the outputs of the AGPS dc/ac inverters and at the output of the EGPS. If one or more of these protection signals are activated, the protection is managed as a fault and the NBI-PIS is informed by proper signals. In this case, the AGPS dc/ac inverters and the EGPS are switched off as soon as possible and maintained stopped until the reset by the operator; the reset operation is made trough NBI-PIS. After that, the NBI PS system can restart with the proper sequence as specified in section 6.1.3.

If also this second level of intervention fails, a third level is provided by passive or active devices directly connected to the dc/ac inverters of AGPS and EGPS. If one or more of these protection devices are activated, this event is managed as a fault and the NBI-PIS is informed by proper signals. In particular, if one fired protection device is inside the AGPS-CS (a fuse, for example), the AGPS LCS turns off the ac/dc conversion system and commands the firing of the dc-link crow-bars and the opening of the 66 kV ITER circuit breaker (or the 22 kV distribution board for the PRIMA site).

8.7 Beam-off detection and intervention

If a large part of the beam current is switched off in a short time (beam-off), this is equivalent to a loss of load and an over-voltage appears at the outputs of the AGPS-DCG. To reduce the electrical stress on the AGPS components, the beam-off condition has to be properly detected and, on occurrence of a beam-off event, the AGPS dc/ac inverters have to be promptly switched off.

The beam-off detection can be triggered because of three alternative events:

1. switch-off of the plasma light, detected by the plasma light optical fibers. A certain number of optical fibers are inserted inside the ion source to detect the presence of the plasma light, and the respective optical signals are converted into electrical signals by means of photo-couplers. In particular, the beam-off detection is triggered if the light is off on a sufficient number of optical fibers;

2. the negative current slope of the EGPS output current exceeds a certain adjustable threshold;

3. a DCG output current measurement falls below a threshold while the "AGPS ON" signal is active and, consequently, the corresponding AGPS "beam-off detector" is triggered. Obviously, if this protection is based on the current level and not on the current negative slope, it has to be excluded during a ramp-up of the acceleration voltage without load (see section 6.1.3). In addition, the beam-off event could be detected also using the DCG output voltage measurements: if one voltage measurement exceeds a threshold while the "AGPS ON" signal is active, the corresponding AGPS "beam-off detector" is triggered as well.

If the third event happens, the AGPS protects itself against the Beam-off event by stopping all the gating signals of the dc/ac inverters, the event is logged on the HMI of the AGPS LCS and the LCS communicates the event to the BBD by a dedicated digital signal. In any case, if a beam-off is detected, the BBD coordinates the protective actions among the AGPS and the EGPS. Consequently, all the gating signals of the AGPS dc/ac inverters and of the EGPS are quickly stopped, as required in section 6.1.5. Moreover, in case of beam-off, the BBD informs also the NBI-PS Control and the NBI-PIS and the event is managed as a fault. The NBI-PIS sends a redundant fault command to AGPS and EGPS. The NBI-PS Control forces to zero the voltage references for the AGPS dc/ac inverters and the EGPS, and forces to zero also the power references provided to the RF generators.

After a beam-off event, the gate commands of AGPS and EGPS are maintained stopped until the reset by the operator, made through NBI-PIS. After that, the NBI PS system can restart with the proper start-up sequence, as described in section 6.1.3. Figure 8-5 summarizes the protection logic for a beam-off event.
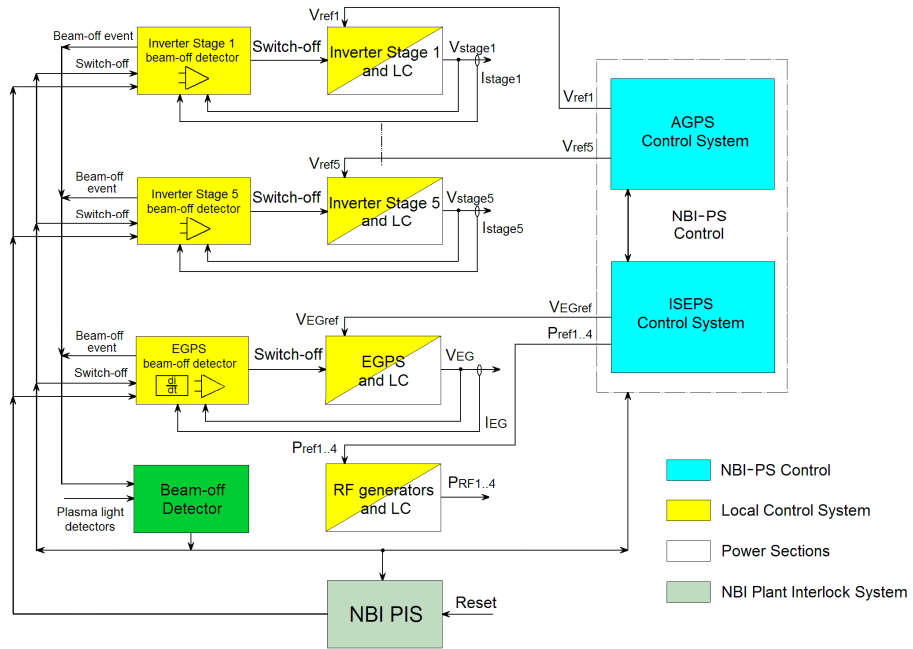
Figure 8-5 – Protection logic for a beam-off event

9   AGPS models

9.1   Introduction

In this section, the models used to simulate the AGPS are described. The main aim of these analyses is to verify the static and dynamic performance of the AGPS, and to compare these results with the electrical and functional requirements given in section 6. All the simulations have been performed with PSIM™ [30]. In general, the topologies and the electrical parameters implemented in the models reflect the technical solutions described in section 7.

Depending on the scope of the analysis, two different AGPS models have been setup, with different levels of detail. Both models implement a detailed description of the dc/ac conversion system, the DCG and the load. In addition, the first model includes also the ac/dc conversion system, with the step-down transformer, the ac/dc thyristor bridges and the dc-link capacitor bank. This model is useful to simulate the dynamic performance of the overall AGPS system, including the transient variations of the dc-link voltage. In the second model, the ac/dc conversion system is not implemented and the dc-link is schematized as two ideal voltage generators, in order to reduce the computational time. Both models are organized hierarchically in blocks and sub-blocks, most of them being shared among the models implemented. In the following, each sub-block is described.

9.2   Model of the ac/dc conversion system

To reduce the computational time, the model of the ac/dc conversion system schematizes two 6 pulses ac/dc rectifiers (instead of 12 pulses rectifiers, as foreseen in the reference design, see Figure 7-1). Therefore, it includes a single step-down transformer with two secondary windings, supplying two thyristor bridges connected in series at the output. Each thyristor bridge feeds a half of the dc-link capacitor bank and its output voltage is feedback controlled by an independent control loop. The ground reference of the ac/dc conversion system is the central point of the dc-link, which is connected to the local ground of the step-up transformers. The model of the ac/dc conversion system is reported in Figure 9-1.

Each control loop includes a PI regulator, which normally receives as input the difference between the voltage reference, ranging from 0 to 3250 V, and the actual output voltage of the respective rectifier. This difference is filtered in advance by a low-pass second order filter (cut-off frequency 300 Hz), in order to reduce the 300 Hz ripple. The output of the PI regulator represents (in radians) a phase shift, which is subtracted to the initial phase shift of 120° to obtain the firing angle α for the thyristor bridge. In this way, at the beginning of the simulation the firing angle is 120°, so the output voltage is zero, as the voltage of the dc-link capacitor bank, and no over-currents occur. The transfer function of the PI regulator can be represented as follows:

$$G_C{}'(s) = K_I{}' \frac{1 + s\tau_Z{}'}{s} \tag{9-1}$$

where $K_I' = 1/43 = 23.3 \cdot 10^{-3}$ (V s)$^{-1}$ is the integral gain and $\tau_Z' = 11.4$ ms ($f_Z = 14$ Hz) is the time constant of the zero. These values have been chosen tentatively by simulation, as a trade-off between the stability of the system and the dynamic performance. However, once the PI gains are optimized, the dynamics of the ac/dc converter is limited by the frequency of the grid network voltage (50 Hz) and by the number of pulses of the converter.

The feedback control loop includes an anti-windup circuit. In detail, when the output of the PI regulator exceeds the upper or the lower limit (120° and 0°), the difference between the output of the regulator and the limit is amplified and subtracted to the input, in order to keep constant the output of the regulator. This to avoid an excessive drift of the output of the integral regulator when the difference between the output voltage and the reference cannot be nullified quickly. The anti-windup circuit is useful to improve the dynamic performance of the regulator for example in case of restart after a loss of load which caused a dc-link over-voltage.

The time base for the gating commands for the thyristor bridge is given by the "alpha controller", represented with a triangle in Figure 9-1. On each period of the grid voltage, this block generates the triggers for the first couple of conducting switches of the bridge, basing on the actual firing angle and on the synchronization signal produced at the zero crossing of a phase-to-phase grid voltage. The thyristor bridge block generates automatically the gating signals for the other switches.

In the model of Figure 9-1, L_{S1}, L_{S2}, L_{S3} and L_{D1}, L_{D2}, L_{D3} represent the equivalent leakage inductances of the step-down transformer seen from the secondary side, as calculated in section 7.1.
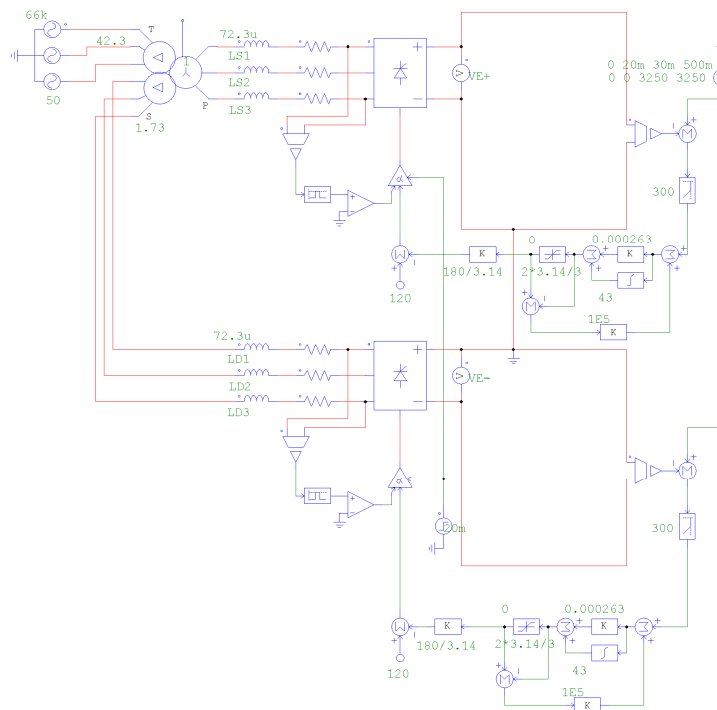

Figure 9-1 – PSIM™ model of the ac/dc conversion system

9.3   Models of the NPC inverter

The basic model used to simulate the NPC inverter is represented in Figure 9-2. This model is the reproduction of the NPC inverter topology, with four active switches for each leg, each one with anti-parallel diode, plus two freewheeling diodes per leg, as in Figure 7-2. The gate commands are generated by two-threshold PWM modulators, one for each leg, basing on the modulation index m and three triangular carriers, phase shifted each other by 120°. The gate commands are directly enabled by an external enabling signal.
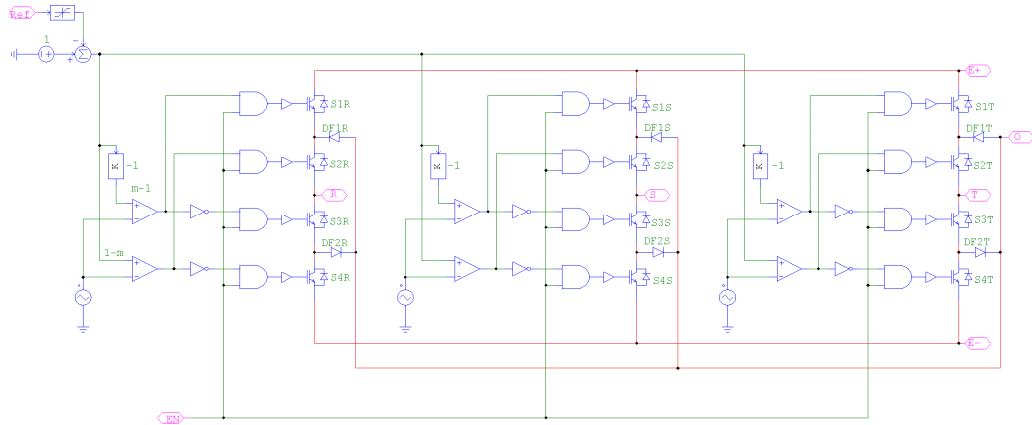
Figure 9-2 – PSIM™ basic model of the NPC inverter

The simulations carried out with the model of Figure 9-2 could be quite time consuming, because of the large number of switches. Therefore, the alternative simplified model of Figure 9-3 has been used in some cases. In this model, only 3 ideal bi-directional switches for each leg are used. The high and low phase voltages ($+V_{dc}/2$, $-V_{dc}/2$) are obtained with the switches S1x and S3x respectively (x being R, S or T), whereas the zero voltage is obtained with the switches S2x. This simplified model is less accurate with respect to the model of Figure 9-2, for example it cannot simulate the real re-circulation of the currents from the load to the dc-link through the anti-parallel diodes when all the gate commands are stopped. Therefore, this model can be used instead of the previous one for the analysis of the dynamic performance of the overall AGPS system, but not for the simulation of the AGPS protections against grid breakdowns and beam-off.
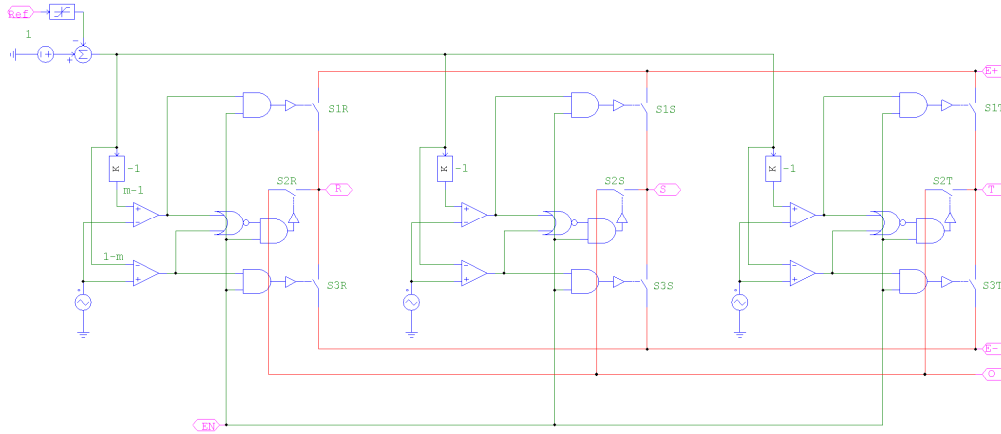
Figure 9-3 – Alternative simplified PSIM™ model of the NPC inverter

Another model for the NPC inverter has been used in some simulations, to quantify the actual maximum switch-off delay of the NPC inverter. This model is shown in Figure 9-4. With respect to the model of Figure 9-2, a system of interlocked latching chains is connected to the gates of the active switches, in order to simulate the switching delay and the timing constraints of the real IGCT, for example to keep on the internal switches while the external switches are on, as required for the NPC inverters.
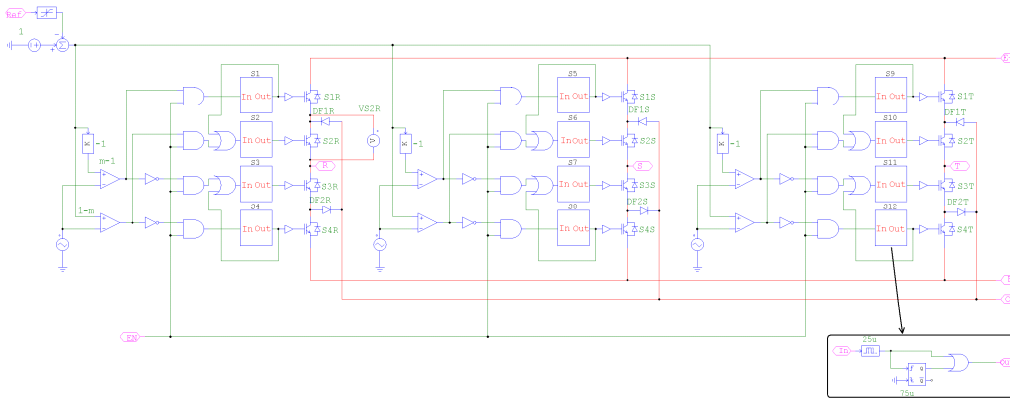
Figure 9-4 – Detailed PSIM™ model of the NPC inverter used to quantify the maximum switch-off delay

9.4   Model of the dc/dc 200 kV generation stage

The NPC inverter models are used as sub-circuits in a higher-level model, represented in Figure 9-5, where the dc/ac conversion system and the DCG are represented. The inductances at the secondary side of the step-up transformer represent the sum of the contribution of the step-up transformer leakage inductance and of the maximum inverter output inductance, as in eq. (7-19).

The model of Figure 9-5 includes also the DCG output voltage control loop. The DCG output voltage is filtered through a low pass filter (cut-off frequency 1.3 kHz) and it is compared with

the voltage reference. The difference is the input of a PI regulator, having the following transfer function:

$$G_C(s) = K_I \frac{1 + s\tau_Z}{s} \tag{9-2}$$

where $K_I = 0.5 \cdot 10^{-3}$ (V s)$^{-1}$ is the integral gain and $\tau_Z = 1.112$ ms ($f_Z = 143$ Hz) is the time constant of the zero. As for the PI regulator of the ac/dc conversion system, also these gains have been tentatively chosen by simulation as a trade-off between the stability of the system and its dynamic performance. Moreover, to improve further the dynamic response, a feed-forward component is added to the output of the PI regulator; the gain is set to add 0.5 to the modulation index when the voltage reference is equal to 200 kV. The output of the regulator is a phase shift represented in radians and limited by an anti-windup circuit between 0 and 90°. Also in this case, the anti-windup circuit is useful to improve the dynamic performance of the regulator in case of restart after stopping of the dc/ac inverter gate commands (for example in case of grid breakdown or beam-off).

In the model of Figure 9-5, an over-voltage protection has been included. This and other protections have been implemented when necessary for some specific analyses. The over-voltage protection of Figure 9-5, in particular, is latched-up when the DCG output voltage exceeds 220 kV, after a fixed time delay of 150 µs.
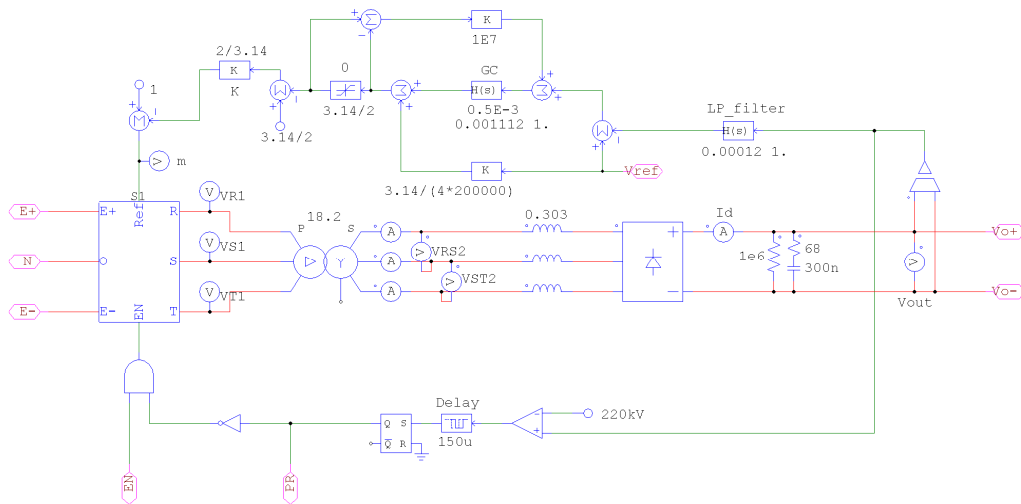

Figure 9-5 – PSIM™ model of the dc/dc 200 kV generation stage

9.5 Model of the load

The AGPS load is the NBI accelerator. The current flowing on each DCG stage is the difference of the output current of the previous DCG minus the beam current intercepted by the acceleration grid connected to the two stages. The current delivered by DCG5, which is connected to the ground of the NBI, is the sum of the accelerated beam current (gathered through the neutralizer, the RID and other structures) and the beam current intercepted by the grounded grid. All these currents depend mainly on the power delivered to the RF drivers by the RF generators, which is regulated in real time in order to achieve an accelerated beam current which should be a function of total accelerating voltage, in agreement with the perveance matching equation [eq. (4-1)]. Being the dynamics of the RF generators much faster than those of the AGPS, the load can be represented by ideal voltage controlled current generators as in Figure 9-6, the current being a function of instantaneous voltage in agreement with the perveance matching requirement. The output voltage is measured through a low pass filter (cut-off frequency 600 Hz), to dump the voltage ripple at $6 \cdot 150 = 900$ Hz.

To simulate the grid BD, each DCG output voltage can be short-circuited by an ideal switch, in series with a dc voltage generator (100 V), representing the arc voltage.
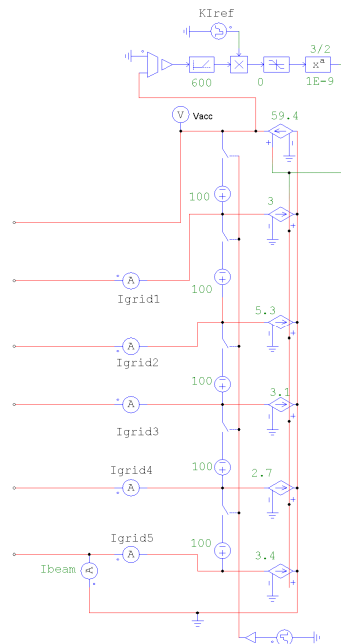

Figure 9-6 – PSIM™ model of the load. The set of currents shown here corresponds to the nominal Deuterium operation

9.6 AGPS detailed model

The models described above are collected in a comprehensive and detailed model of the AGPS, shown in Figure 9-7. The model of the ac/dc conversion system feeds the models of the five dc/dc 200 kV generation stages, and the outputs of such stages are connected in series. These outputs feed directly the model of the load: the TL, in this case, is considered as an ideal connection between DCG and accelerator. In fact, this model is used to evaluate the dynamic performance of the overall AGPS system, and no impact in the results is expected if a more detailed high-frequency model of the TL is included, as demonstrated by simulation.

The dc-link capacitor bank is split among the five dc/ac inverter stages, and the total capacitance of the overall dc-link is assumed to be 50 mF, as in section 7.2. Each dc/ac inverter stage is represented as a single NPC inverter to reduce the number of switches and consequently the computational time, whereas in reality at least two inverters in parallel are foreseeable for each stage. The decoupling inductances at the output of the inverters are lumped with the leakage inductance of the step-up transformer, as shown in Figure 9-5.
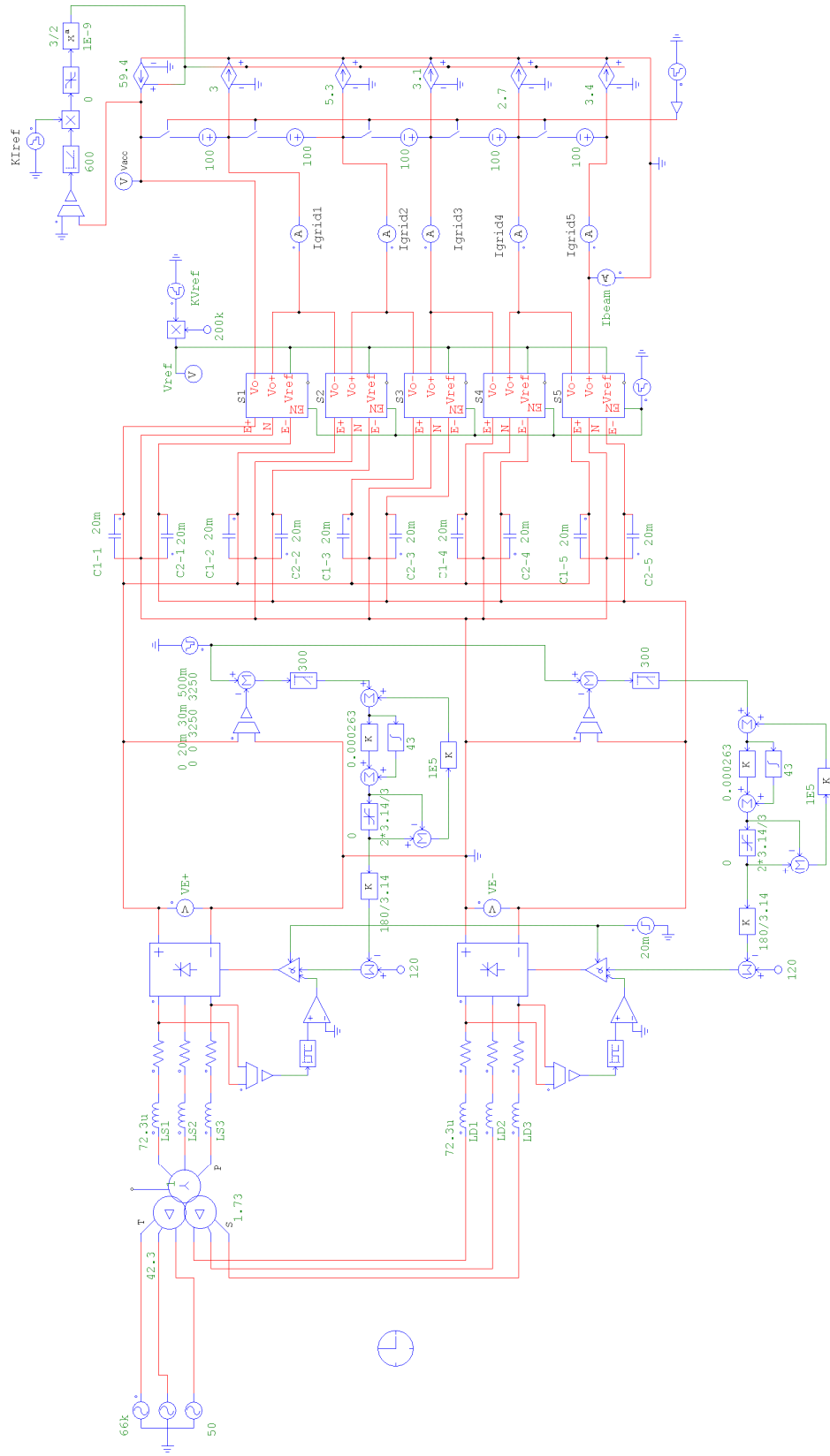
Figure 9-7 – Detailed PSIM™ model of the AGPS

9.7 Simplified model

When it is not necessary to simulate the dynamic behavior of the ac/dc conversion system, the simplified model of the AGPS shown in Figure 9-8 has been used. Here, the dc-link is schematized as two ideal voltage generators and the ac/dc conversion system is not represented, to reduce the computational time.
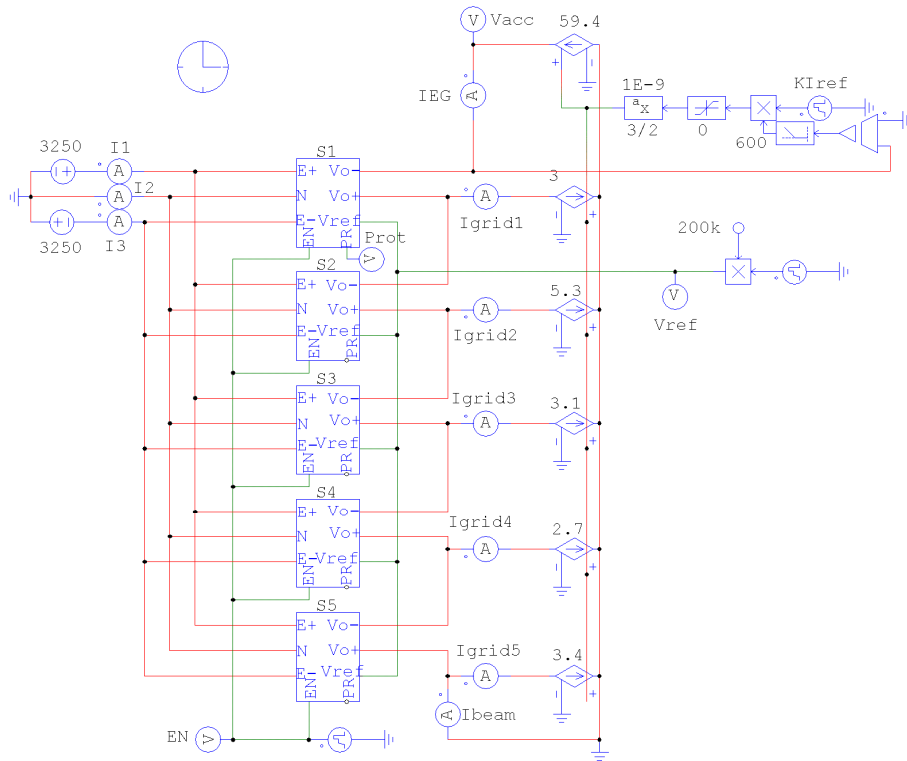

Figure 9-8 – Simplified PSIM™ model of the AGPS

10 Verification of AGPS steady state performance

In this and in the following sections, the results achieved with the AGPS models previously described are shown. This section is devoted to the simulations aiming at demonstrating the compliance of the AGPS reference design with the steady state electrical requirements. The next section is focused on the AGPS dynamic performance, both in normal operating conditions and after a grid BD or a beam-off. Previous results of these analyses can be found in [31].

10.1 Verification of the rated output voltages

To support the choice of the step-up transformer turn ratio, the simplified model of the AGPS has been simulated, both with a dc-link voltage equal to the rated value (6.5 kV) and with a reduced value to take into account the maximum steady state error. In Figure 10-1, the results for V_{dc} = 6.5 kV are shown, for DCG output currents equal to the nominal load currents for Deuterium operation of Figure 6-1. The DCG rated output voltages for Deuterium operation (200 kV) are reached, with modulation indexes lower than 0.89.
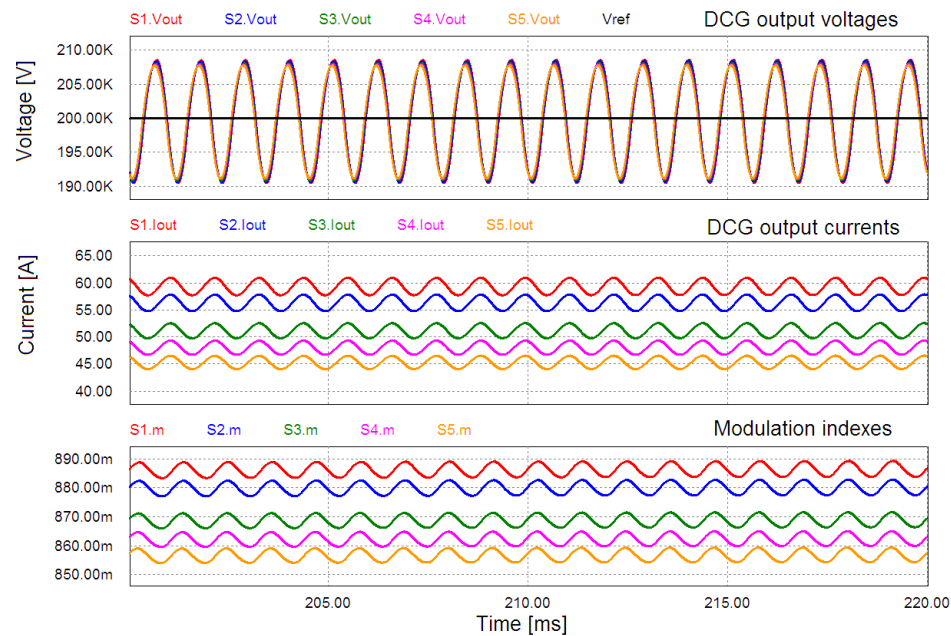

Figure 10-1 – DCG output voltages, DCG output currents and modulation indexes of the five dc/ac inverters, with the nominal currents for D- operation and the rated dc-link voltage (V_{dc}=6.5 kV), with the dc/ac inverters synchronized in phase

The simulation has been repeated for the first stage, assuming V_{dc} = 6.5 kV - 5% and a DCG output current equal to the rated current for Deuterium operation (62 A, from Table 6-1).
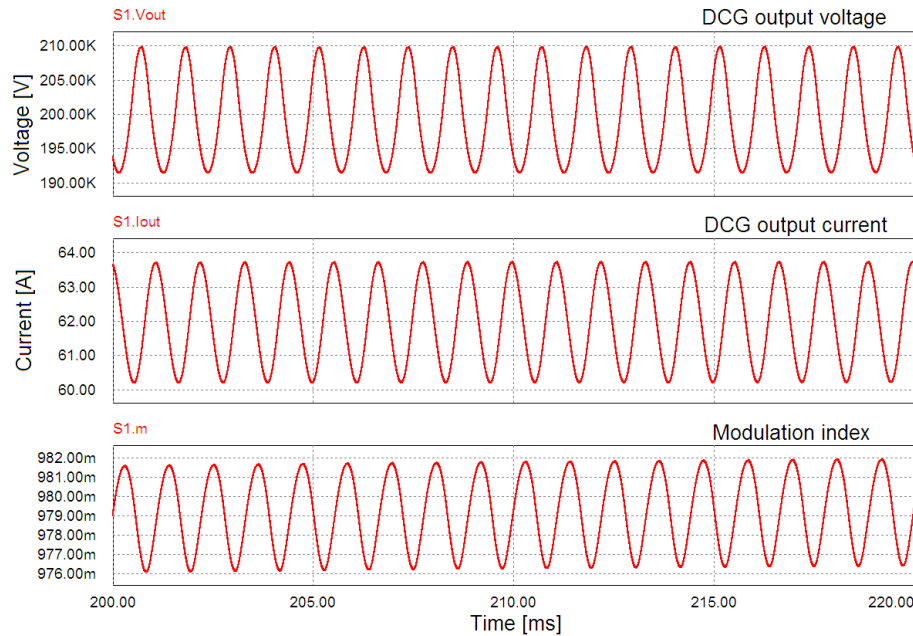
Figure 10-2 – DCG output voltage, DCG output current and modulation index of the first stage, with the rated current for D- operation (62 A) and dc-link voltage V_{dc}=6.5 kV-5%

As shown in Figure 10-2, the modulation index is lower than 0.982 ≅ 0.98, which is feasible. With V_{dc} = 6.5 kV - 6%, instead, the modulation index oscillates between 0.995 and 1, values not reachable in practice. In conclusion, to reach 200 kV with the rated DCG output current of the first stage for Deuterium operation, the steady-state error of the dc-link voltage has to be lower than 5%, including the accuracy of the voltage measurement.

10.2 Verification of the output voltage ripple

The percentage ripple of the DCG output voltage for Deuterium operation, with the nominal DCG output currents, can be calculated from Figure 10-1: it is ±4.5%, which is lower than the requirement of Table 6-2 (±5%). The simulation has been repeated with the nominal DCG output voltages and currents for Hydrogen operation of Figure 6-2, with the same dc-link voltage (6.5 kV). The result is shown in Figure 10-3. In both simulations, the carrier waveforms of the dc/ac inverters are synchronized in phase.
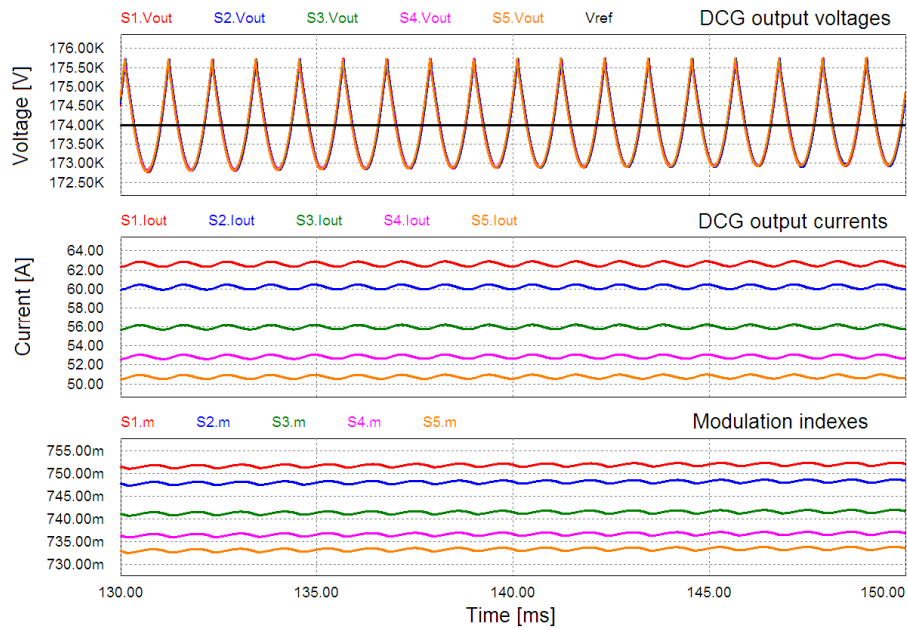
Figure 10-3 – DCG output voltages, DCG output currents and modulation indexes of the five dc/ac inverters, with the nominal currents for H- operation and the rated dc-link voltage (V_{dc}=6.5 kV), with the dc/ac inverters synchronized in phase

In this case, the voltage ripple is much lower: ±0.8%; also the waveform of the ripple is different. This because of the different modulation indexes, which are around 0.74. In fact, after repeating the simulation with a lower dc-link voltage (V_{dc} = 5386 V) in order to have m ≅ 1, the voltage ripple becomes about ±4.8%, as shown in Figure 10-4. This can be easily explained by analyzing the no-load secondary voltage of the step-up transformer, shown in Figure 10-5. Here, for a dc-link voltage equal to 6.5 kV, the modulation index has been ramped up in open loop from 0 to 1, without load and without HV dc-filter. The secondary phase-to-phase voltage of the step-up transformer shows 5 levels for m < 1/3 and 7 levels for 1/3 < m < 1 (and m ≠ 2/3) . The levels become only 4 for m = 1/3 and m = 1 and 3 for m = 2/3. For m = 2/3, the phase-to-phase voltages of the step-up transformer become square waveforms, with duty-cycle 2/3, phase shifted of 120° each other. Therefore, the rectified voltage becomes constant. For similar reasons, the rectified voltage becomes constant also for m = 1/3 and m = 1. If also the load and the HV dc-filter are included, the minimum of the ripple occurs for modulation indexes higher than 2/3 and 1/3, because of the voltage drop on the total equivalent inductance at the secondary side of the step-up transformer. For the same reason, the minimum of the ripple corresponding to m = 1 cannot be reached (and in any case the maximum realistic value for m is 0.98). In addition, the two exact values of the modulation index corresponding to the minimum of the ripple depend on the load current. It can be concluded that, in minimizing the output voltage ripple by using the "Ripple controller", generally the best reference modulation index is not the maximum one.
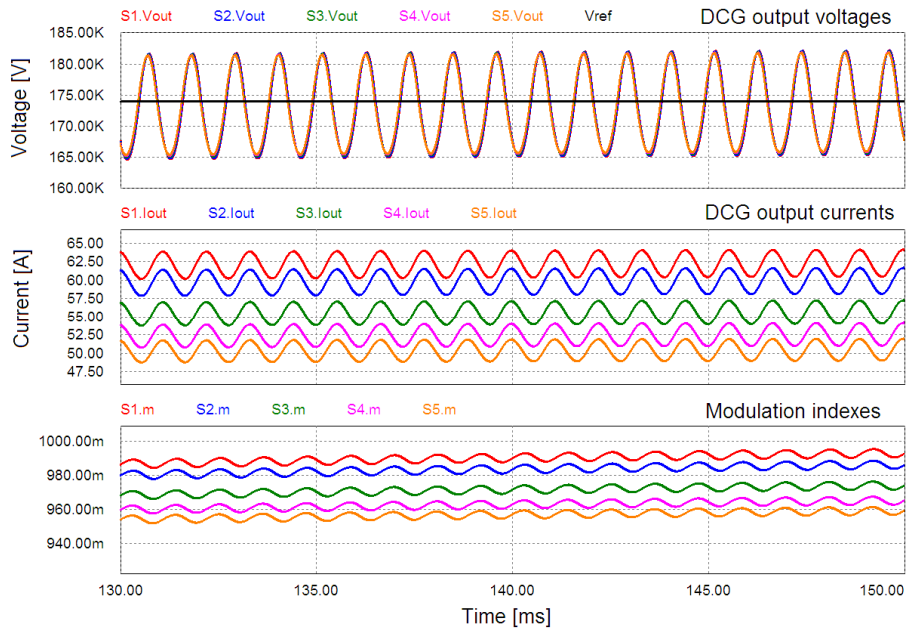
Figure 10-4 – DCG output voltages, DCG output currents and modulation indexes of the five dc/ac inverters, with the nominal currents for H- operation and V_{dc}=5386 V, with the dc/ac inverters synchronized in phase
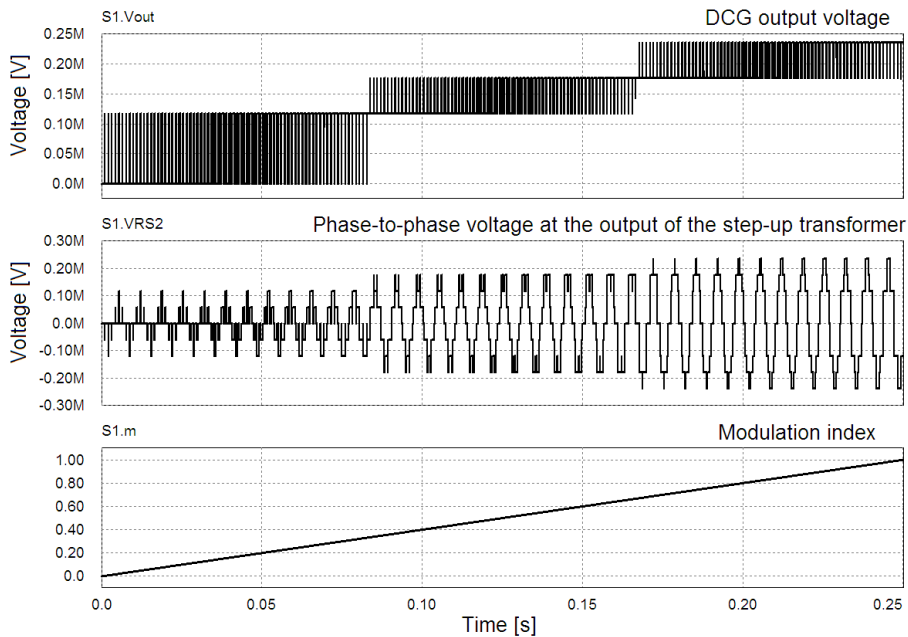

Figure 10-5 – DCG output voltage, step-up transformer output phase-to-phase voltage and modulation index, without load and HV dc-filter, with V_{dc}=6.5 kV

As mentioned in section 8.3, in default conditions the carrier waveforms of the five dc/ac conversion system regulators are synchronized in phase. Anyway, it is be possible to select a phase shift between the carrier waveforms inside the range [0°,360°]. Figure 10-6 shows the results in terms of DCG output voltages and currents for Deuterium operation, with the inverter carriers phase shifted by 72°. The ripple at the output of each DCG stage is ±4%, similar than

the one of Figure 10-1, but the ripple of the total accelerating voltage is strongly reduced, resulting less than ±0.28% from this simulation. Most of the residual ripple is due to minor differences among the DCG output voltage amplitudes. Also the ripple of the load currents is reduced, being a function of ripple of the total accelerating voltage (related with the perveance matching law and the low-pass filter for the ripple included in the model). This is the reason of the small reduction of the voltage ripple at the output of each DCG (from ±4.5% to ±4%).
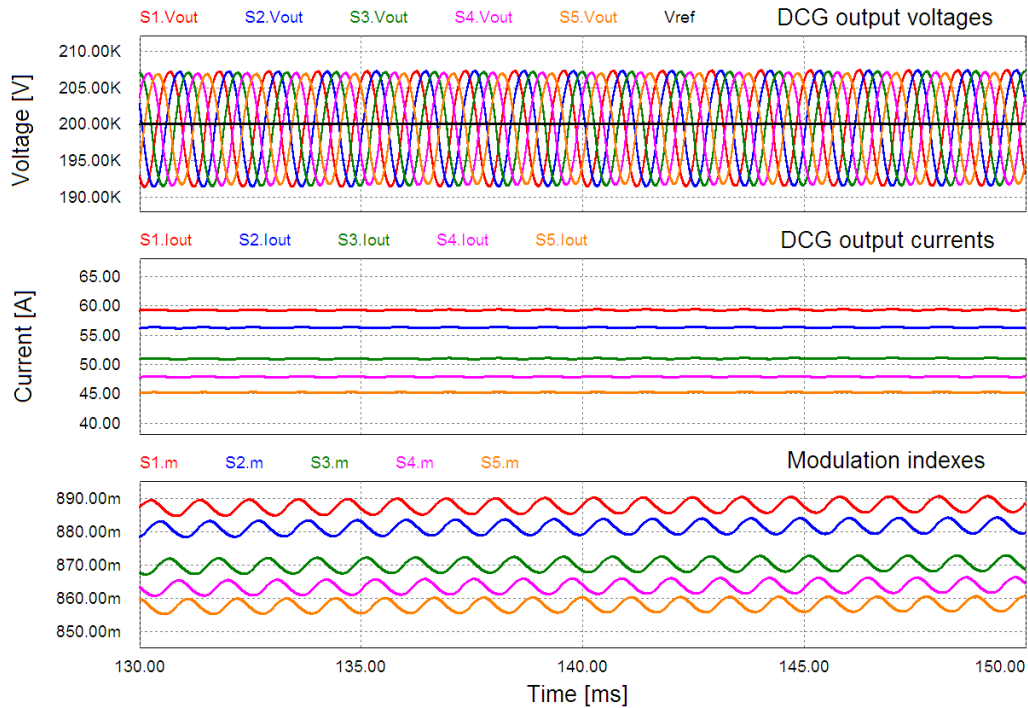

Figure 10-6 – DCG output voltages, DCG output currents and modulation indexes of the five dc/ac inverters, with the nominal currents for D- operation and the rated dc-link voltage (V_{dc}=6.5 kV), with the dc/ac inverter modulation carriers phase shifted by 72° each other

Of course, if the frequency of the dc/ac inverter output voltages is 300 Hz instead of 150 Hz, the voltage ripple at the output of the DCG is reduced. From simulation, for Deuterium operation it is found a voltage ripple of ±0.95% instead of ±4.5% on the single stage (the ripple frequency is 1.8 kHz instead of 900 Hz), the same of the total accelerating voltage if the carrier waveforms are synchronized in phase.

10.3 Verification of the currents in the dc/ac inverters

In this section, the dc/ac inverter output currents and the currents in the inverter power switches are evaluated and compared with the simplified calculation of section 7.3. The analyses have been carried out for the nominal Hydrogen operation (worst case), in the two opposite cases (m = 1 and V_{dc} = 6.5 kV, alternatively), for the first stage.

10.3.1 Hydrogen operation, with m=1 and V_{dc}=5386V

A simulation has been carried out with the simplified model of Figure 9-8 and the dc-link voltage set to V_{dc} = 5386 V, in order to achieve the dc output voltage of 174 kV (nominal Hydrogen operation) with m = 1 in the first stage, with the rated dc output current (66 A). The results are shown in Figure 10-7.
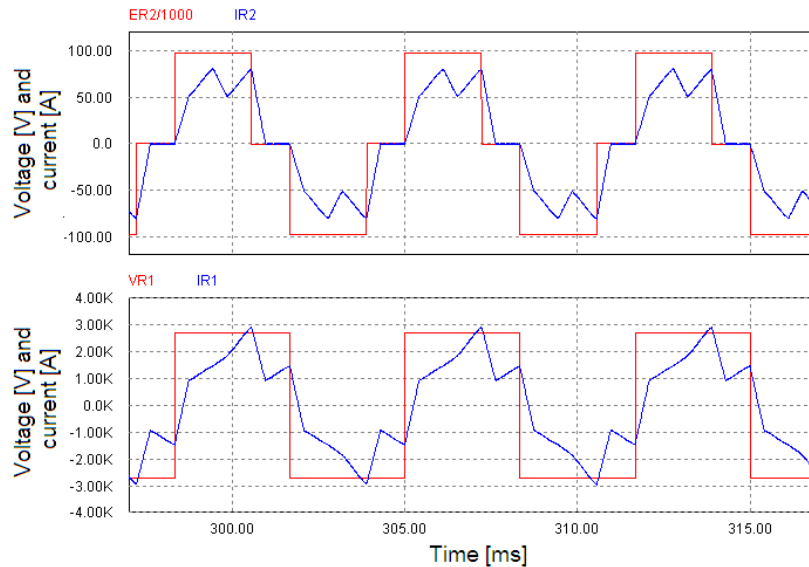

Figure 10-7 – Rated H- operation, first stage, with V_{dc}=5386 V and m=1. First row: phase to neutral voltage (red, divided by 1000) and phase current (blue) on the step-up transformer secondary side. Second row: phase voltage (red) and phase current (blue) at the inverter output

The inverter rms output current is 1666 A, very similar to the rated value found in section 7.3 (I_{INV} = 1700 A). The peak current is 2939 A.

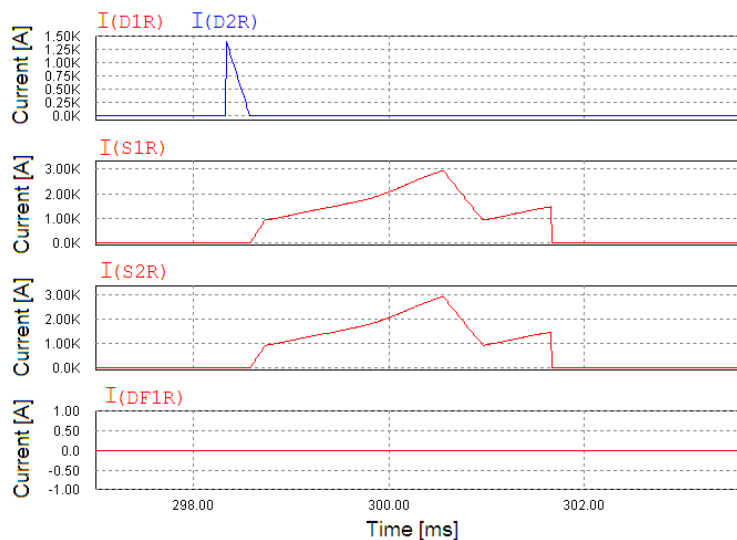The current waveforms of the inverter power switches (named as in Figure 7-2) are shown in Figure 10-8.

Figure 10-8 – NPC inverter switch currents for the rated H- operation (first stage), with V_{dc}=5386 V and m=1. First row: currents in the anti-parallel diodes. Second row: current in the external active switches. Third row: current in the internal active switches. Fourth row: current in the freewheeling diodes

From Figure 10-8, it can be noted that the external and the internal anti-parallel diodes have the same current waveforms. Moreover, also the external and the internal active switches have the same current waveforms, while the freewheeling diodes do not conduct, because the inverter operates with m = 1.

The average and rms values of the currents and the switch-off currents of all the inverter switching devices are shown in Table 10-1.

Table 10-1 – Currents in the inverter power switches with m=1 and V_{dc}=5386 V, for the rated H- operation

Device	I_{avg} [A]	I_{rms} [A]	Switch-off current [A]
Anti-parallel diodes (D1x, D2x)	27	162	0
External active switches (S1x, S4x)	739	1167	1462
Internal active switches (S2x, S3x)	739	1167	1462
Freewheeling diodes (DF1x, DF2x)	0	0	0

10.3.2 Hydrogen operation, with m=0.742 and V_{dc}=6500V

The simulation has been repeated with the dc-link voltage set to V_{dc} = 6500 V and controlling in feedback the modulation index m in order to produce a dc output voltage equal to 174 kV with the rated dc output current for the Hydrogen operation. The results are shown in Figure 10-9.
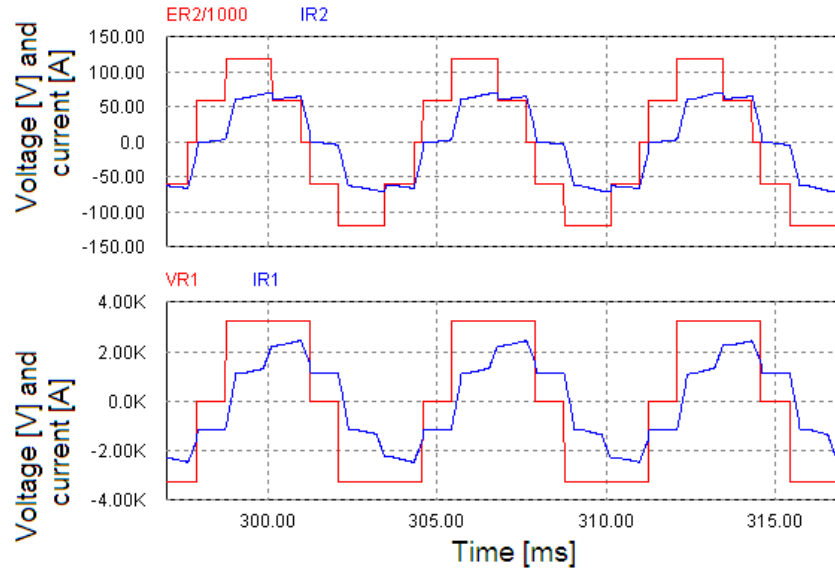

Figure 10-9 – Rated H- operation, first stage, with V_{dc}=6.5 kV. First row: phase to neutral voltage (red, divided by 1000) and phase current (blue) on the step-up transformer secondary side. Second row: phase voltage (red) and phase current (blue) at the inverter output

In this case, the inverter rms output current is 1638 A and the peak current is 2454 A. The current waveforms of the inverter switches are shown in Figure 10-10.
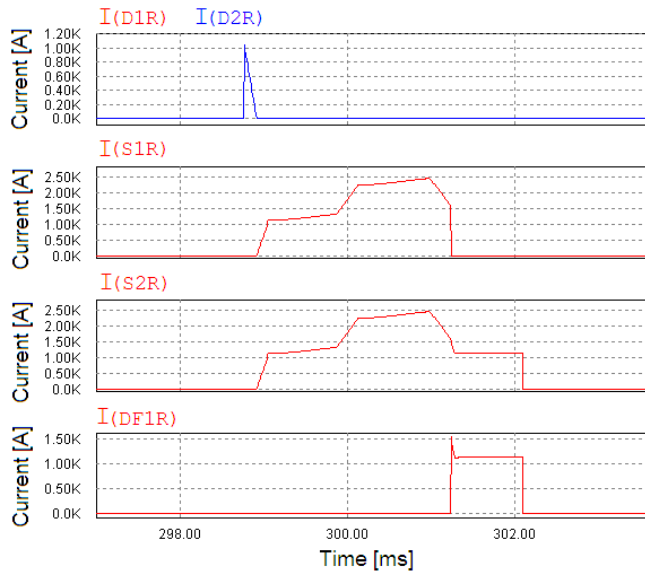
Figure 10-10 – NPC inverter switch currents for the rated H- operation (first stage), with V_{dc}=6.5 kV. First row: currents in the anti-parallel diodes. Second row: current in the external active switches. Third row: current in the internal active switches. Fourth row: current in the freewheeling diodes

From Figure 10-10, it can be noted that the external and internal anti-parallel diodes have the same current waveforms. The external and internal active switches have different current waveforms and the freewheeling diodes conduct because the inverter operates with m < 1.

The average and rms values of the currents and the switch-off currents of all the inverter switching devices are shown in Table 10-2.

Table 10-2 – Currents in the inverter power switches with V_{dc}=6.5 kV, for the rated H- operation

Device	I_{avg} [A]	I_{rms} [A]	Switch-off current [A]
Anti-parallel diodes (D1x, D2x)	12	95	0
External active switches (S1x, S4x)	601	1079	1622
Internal active switches (S2x, S3x)	748	1154	1128
Freewheeling diodes (DF1x, DF2x)	147	409	1128

Comparing Figure 10-8 and Figure 10-10, it can be noted that the switch-off currents of the active switches are similar, as the turn-on current of the anti-parallel diodes. As far as the conduction losses are concerned, the m = 1 case is the worst one for the external active switches, because they are on for a longer time, whereas the case m < 1 is the worst one for the freewheeling diodes. About the switching losses, the diodes in anti-parallel to the internal active switches are turned on at zero voltage always (the internal active switch of the opposite half leg was conducting), whereas the diodes in anti-parallel to the external active switches are turned on at V_{dc} / 2.

Assuming each inverter active switch being realized with a single IGCT, and each dc/ac inverter stage made by a single bridge, the conduction losses in the IGCT in the conditions of

Table 10-2 can be estimated on the basis of the simulation results and the parameters of the component listed in Table 7-3:

$$P_{COND} = V_{T0}I_{avg} + r_T I_{rms}^2 \cong 2 \cdot 750 + 0.54 \cdot 10^{-3} \cdot 1200^2 = 2.3 \text{ kW} \tag{10-1}$$

Assuming a maximum switch-off current of about 3 kA in the worst case (m $\approx$ 0.5), the commutation losses in the IGCT can be calculated on the basis of the parameters listed in Table 7-3:

$$P_{COMM} \cong E_{off} \cdot f \cdot \left(\frac{V_{dc}/2}{4kV} \cdot \frac{3kA}{4kA} \right) = 4 \text{ kW} \tag{10-2}$$

where, being $E_{off} \gg E_{on}$, only the switch-off losses are considered. Assuming a water cooled heat-sink having a thermal resistance $R_{th\text{-}hw}$ = 5 K/kW, the following total over-temperature of the junction of the component is obtained:

$$\Delta T = \left(R_{th-jc} + R_{th-ch} + R_{th-hw} \right) \cdot \left(P_{COND} + P_{COMM} \right) = \left(8.5 + 3 + 5 \right) \cdot \left(2.3 + 4 \right) = 104\,°C \tag{10-3}$$

Considering a maximum water temperature of 42 °C (as specified for ITER), the temperature of the IGCT junction would reach 104 + 42 = 146 °C, which is over the capability of the device. Therefore, at least two inverter bridges in parallel are necessary to sustain the current.

11 Verification of AGPS dynamic performance

11.1 Verification of voltage ramp-up performance

To verify the dynamic performance of the AGPS system, two simulations have been performed for Deuterium and Hydrogen operation respectively, using the detailed model of the AGPS of Figure 9-7. The voltage of the grid network has been set equal to the nominal value for the ITER site: 66 kV rms. In both simulations, firstly the dc-link voltage has been charged up to the rated value (6.5 kV in total), with the dc/ac conversion system switched off. Then, as soon as the dc-link voltage was quite stable, a ramp-up of the acceleration voltage reference has been applied in 80 ms, up to the respective nominal value: 200 kV per stage for Deuterium operation, 174 kV per stage for Hydrogen operation. The beam current has been controlled in perveance matching, in order to achieve the nominal currents of Figure 6-1 and Figure 6-2 on the five DCG stages in correspondence to the nominal DCG output voltages. The results are shown in Figure 11-1 and Figure 11-2. Here, the first row represents the voltage of the two halves of the dc-link, the second row shows the output voltages of the five stages together with the voltage reference (in black), and the third row represents the total accelerated beam current (ions plus electrons).

At the end of the 80 ms reference ramp-up, with the assumed controller of the dc/ac inverters (PI + feed-forward), in case of Deuterium operation the output voltage of each stage reaches 166 kV (83% of the nominal voltage), instead of 180 kV (90% of the nominal voltage, as required in Table 6-2), whereas in case of Hydrogen operation it reaches 150 kV (86%), instead of 157 kV (90%). A minor part of the delay between actual DCG output voltage and voltage reference is due to the dc-link voltage drop, which however satisfies the specification (±9%, Table 6-7). The rest is due to the regulator dynamic performance, which in turn is limited by the modulation frequency of the dc/ac inverter (150 Hz). Further optimizations seem possible in order to improve the dynamic performance up to reach 90% of the nominal voltage in 80 ms, for example by reducing the ramp-up duration of the reference voltage.

After about 30 ms since the end of the reference ramp, the output voltage is within an accuracy range of ±2% with respect to the nominal value; therefore the 50 ms settling time of Table 6-2 is satisfied. Moreover, during all the perveance-matched start-up, the ripple stays within ±5% of the nominal voltage (200 kV for Deuterium operation or 174 kV for Hydrogen operation, for each stage), with all the dc/ac inverter stages synchronized in phase (worst case). However, the requirement of Table 6-2 regarding the maximum ripple is referred to steady-state condition only.
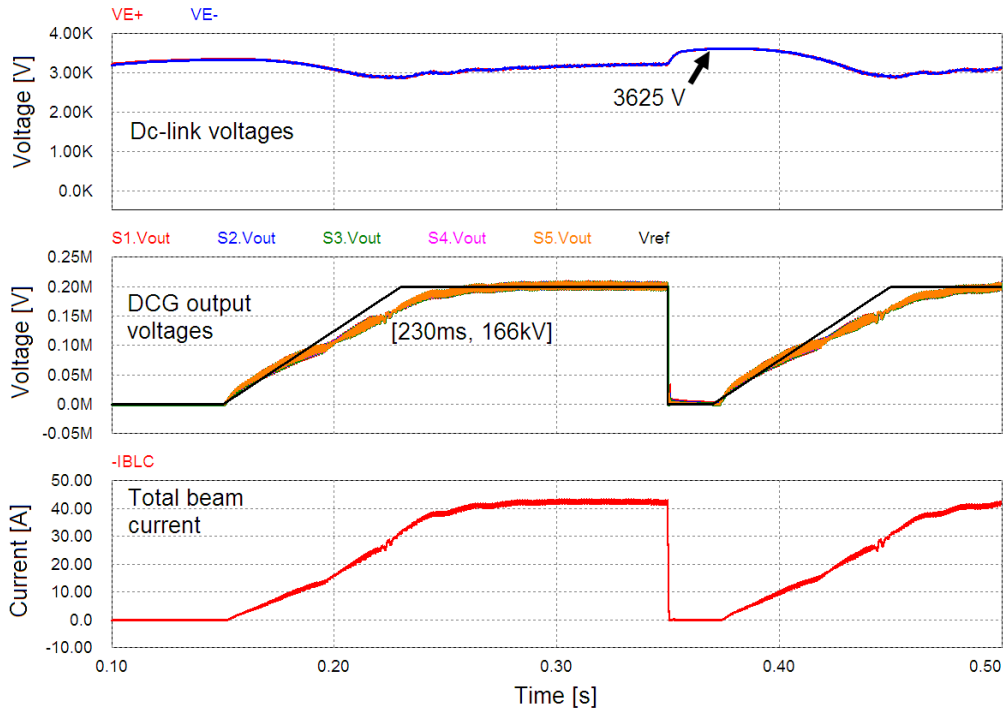
Figure 11-1 – Deuterium operation: at 150 ms, ramp-up of DCG output voltage reference up to the nominal value in 80 ms. Dc-link voltage reference set to 6.5 kV and DCG output currents controlled in perveance matching to the nominal values. Grid BD at 350 ms, switch-off of the dc/ac inverters in 150 μs. New ramp-up of the DCG output voltages starting from 370 ms
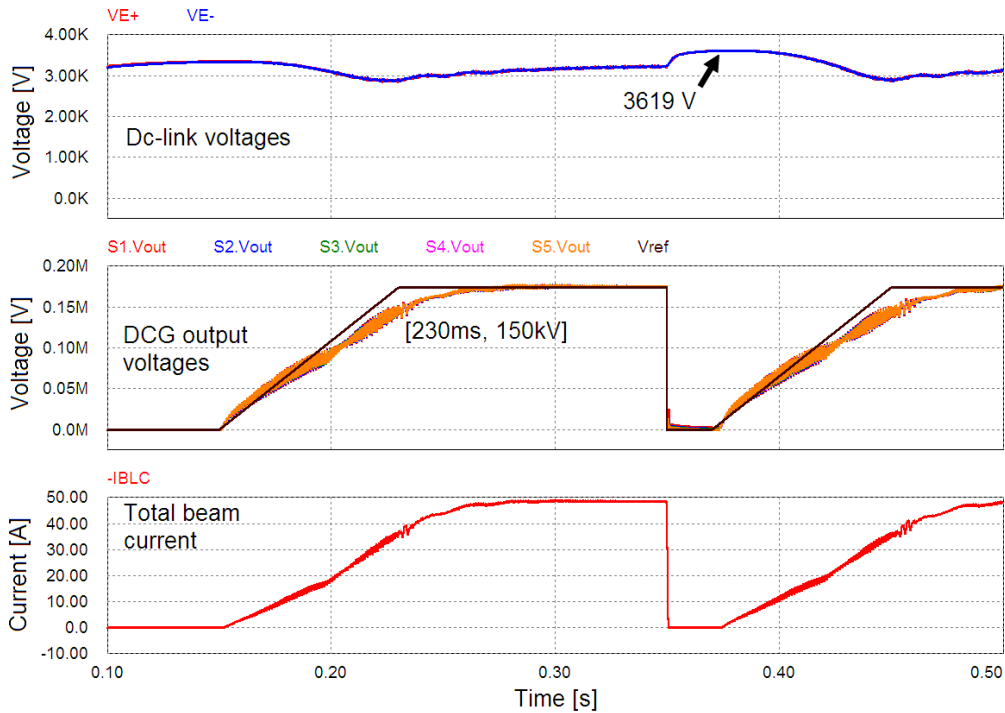

Figure 11-2 – Hydrogen operation: at 150 ms, ramp-up of DCG output voltage reference up to the nominal value in 80 ms. Dc-link voltage reference set to 6.5 kV and DCG output currents controlled in perveance matching to the nominal values. Grid BD at 350 ms, switch-off of the dc/ac inverters in 150 μs. New ramp-up of the DCG output voltages starting from 370 ms

Further analyses have been performed in order to verify the impact of the modulation frequency of the dc/ac inverters on the dynamic performance of the AGPS system. The AGPS simplified model of Figure 9-8 has been used for these simulations, considering the Deuterium operation only. In the same conditions of the previous analyses, the voltage reference is ramped up in 80 ms up to the nominal value (200 kV), with the load currents regulated in perveance matching. In Figure 11-3, the results are shown for a 300 Hz modulation frequency, with the dc/ac inverters controlled with an optimized PI regulator, without feed-forward. At t = 80 ms, the error with respect to the voltage reference is lower than 5%. Conversely, with 150 Hz (Figure 11-4), without feed-forward, the error is about -20%, which can be reduced to about -13% using the feed-forward as in the previous analyses (Figure 11-5). In conclusion, it is confirmed that a 300 Hz modulation frequency would permit better dynamic performance of the AGPS and reduced ripple of the output voltage with respect to 150 Hz. Nevertheless, 150 Hz has been chosen to facilitate the realization of the step-up transformers.
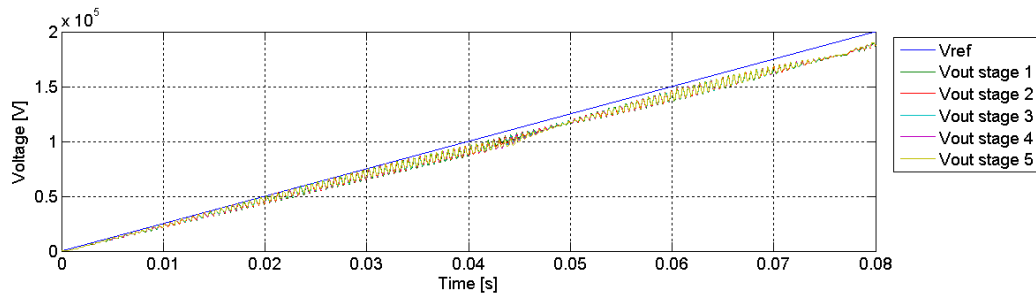

Figure 11-3 – Deuterium operation: ramp-up of the DCG output voltage reference in 80 ms, for a 300 Hz inverter modulation frequency. Dc-link voltage V_{dc} set to 6.5 kV and DCG output currents controlled in perveance matching to the nominal values. Dc/ac inverters controlled with PI regulators only

Figure 11-4 – Deuterium operation: ramp-up of the DCG output voltage reference in 80 ms, for a 150 Hz inverter modulation frequency. Dc-link voltage V_{dc} set to 6.5 kV and DCG output currents controlled in perveance matching to the nominal values. Dc/ac inverters controlled with PI regulators only
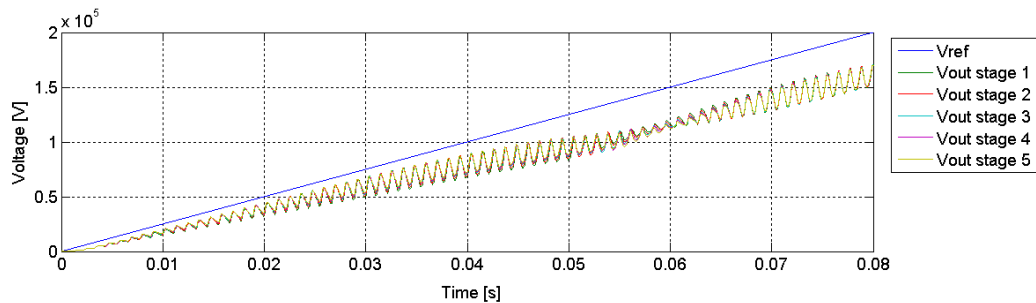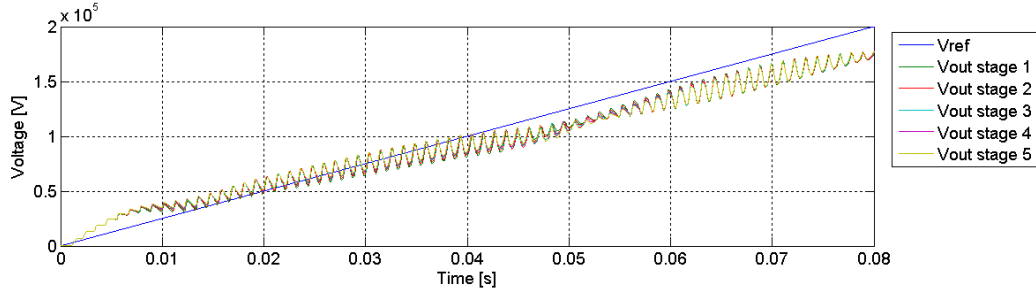
Figure 11-5 – Deuterium operation: ramp-up of the DCG output voltage reference in 80 ms, for a 150 Hz inverter modulation frequency. Dc-link voltage V_{dc} set to 6.5 kV and DCG output currents controlled in perveance matching to the nominal values. Dc/ac inverters controlled with PI regulators plus feed-forward

11.2 Simulation of a grid breakdown

In the same simulation of Figure 11-1 and Figure 11-2, at 350 ms a breakdown of the grids is applied and all the inverter switches are turned off in 150 µs by removing the gate commands. Consequently, the dc-link shows an over-voltage up to 3.62 kV × 2 = 7.24 kV (+11.4%), both in Deuterium and Hydrogen operation. This over-voltage, obtained with an equivalent total dc-link capacitance of 50 mF @6.5 kV, is a bit over the maximum specified (±9%, Table 6-7). The requirement seems however achievable with a further tuning of the thyristor bridge control and/or by increasing the capacitance. Moreover, further analyses should be performed considering the actual reference design of the ac/dc conversion system, which foresees two 12-pulses rectifiers (see Figure 7-1). It can be noted that such over-voltage is lower than the peak of the phase-to-phase secondary voltage of the step-down transformer, which can be calculated with the following formula (see also eq. (7-4)):

$$V_{20,SDnom,pk} = V_{20,SDnom}\sqrt{2} = 2700 \cdot \sqrt{2} = 3.82 \text{ kV} \qquad (11\text{-}1)$$

This means that the control is fast enough to reduce a bit the over-voltage on the dc-link.

After 20 ms (as required in Table 6-4), the acceleration voltage is re-applied, with the same ramp-up as before. The dc-link voltage decreases and finally reaches again the nominal value. The grid BD implies over-currents both in the DCG and in the dc/ac inverters, as shown in Figure 11-6. Here, the results for two different hypothesis are shown, in red for a primary/secondary turn ratio n of the step-up transformer equal to 1/18.2 and a total equivalent inductance at the secondary side equal to L_{tot2} = 0.303 H as in the present reference design (see section 7.4), in blue for a previous design in which there were n = 1/19 and L_{tot2} = 0.407 H. In these simulations, the dc load current is set to 62 A and the voltage reference is 200 kV (Deuterium operation, rated current for the first stage, Table 6-1).
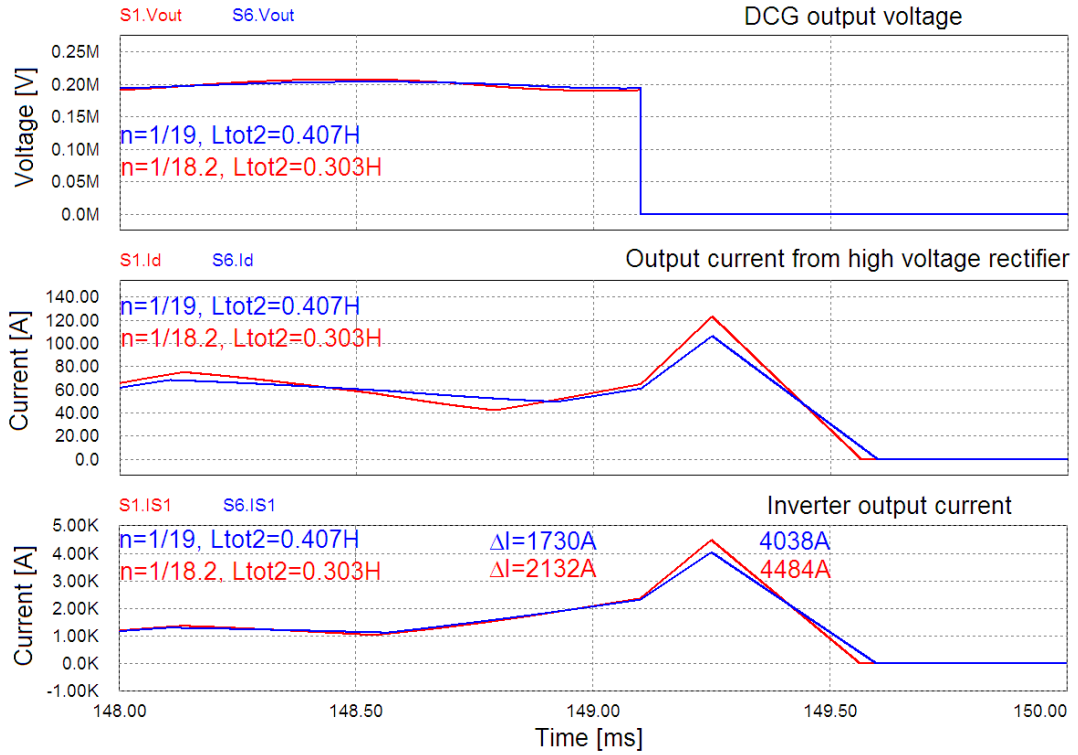
Figure 11-6 – Rated D- operation: DCG output voltage and currents at the output of the HV rectifier and of the dc/ac inverter of the first stage, in case of grid BD. Blue: n=1/19 and L_{tot2}=0.407 H. Red: n=1/18.2 and L_{tot2}=0.303 H

If all the inverter active switches are turned off after a time delay t_{delay} = 150 μs from the grid BD and the full phase-to-phase voltage is applied to a primary winding of the step-up transformer, the over-current at the inverter output can be calculated as:

$$\Delta I = \frac{V_{dc}}{1.5L_{tot1}}t_{delay} = \frac{3V_{dc}}{1.5L_{tot2} \cdot n^2}t_{delay} = \frac{2V_{dc}}{L_{tot2} \cdot n^2}t_{delay} \tag{11-2}$$

In this equation it is assumed that the grid BD appears during a time interval in which one phase to neutral voltage is $+V_{dc}/2$ and the other two are $-V_{dc}/2$ (or vice-versa); this can occur only for m > 2/3. The formula gives exactly the same result of the simulation. Of course, the actual current peak reached at the output of the dc/ac inverter depends on the instantaneous value of the output current before the application of the grid BD. In the simulation of Figure 11-6, the BD has been applied almost in correspondence to the peak of the output current (worst case), reaching an output current peak of 4.48 kA for the present reference design (n = 1/18.2).

In the previous BD simulations, the time delay between the grid BD and the switch-off of all the inverter active switches is assumed equal to 150 μs, being the sum of the maximum detection time (50 μs) and the maximum switch-off time (100 μs) specified in Table 6-4. The detection time is defined as the time interval between BD and protection request, and the maximum value has been fixed basing on the present detection technology, taking some margin. The

switch-off time is defined as the time interval between the triggering of the AGPS BD protection sequence and the time when all the inverter active switches are turned off. The maximum value has been fixed on the basis of the following considerations.

The maximum switching time of one IGCT, defined as the overall time needed to commutate, can be estimated as 25 µs for the most recent technology. The minimum on-time, defined as the minimum time between the last turn-on and the turn-off of one inverter switch, can be estimated as 50 µs for recent IGCT. These reference values have been suggested by industry as those presently used for inverter design.

The internal switches of the inverter cannot be turned off while the external switches are still on, otherwise, for a proper sign of the output line current, the internal switches would be subjected to the overall dc-link voltage (6500 V) plus the transient over-voltage. Moreover, if an inverter switch, for example an external IGCT, is turned on just before the BD protection command, it can be switched off only 50 µs after. In this case, to completely switch off the external switch, at least $50 + 25 = 75$ µs are necessary; after that, also the internal switches of the same leg can be turned off. Therefore, in total, $75 + 25 = 100$ µs is the time needed to switch off all the inverter active switches. This is the reason why 100 µs is specified as the maximum switch-off time.

However, during the switch-off time some active switches commutate in any case, which means that the phase-to-phase voltages applied to the step-up transformer change. In particular, from simulation it can be seen that during the switch-off time the time derivative of the inverter output currents decreases, as the time derivative of the DCG output current.

Two simulations have been performed, with the model of the dc/ac inverters presented in Figure 9-4 and for the most critical modulation indexes, m = 0.333 and m = 0.667, for which two legs commutate at the same time. The results are shown in Figure 11-7 and Figure 11-8, with the dc output current set to 66 A and 5 A respectively. In the first row the inverter output phase voltages are represented; the currents on the switches S1R and S2R (referring to the scheme of Figure 7-2) are reported in the second row; in the third row the three output line currents are shown, and in the fourth row the dc output current from the HV diode rectifier is represented. In these simulations, the triggering of the BD protection occurs just after the commutation of the phases R and S (Figure 11-7) and phases R and T (Figure 11-8), in order to maximize the protection delay.

In both simulations, just before 50 µs from the BD the external switch of the phase R applies $+V_{dc}/2$. Therefore, only after 125 µs from the BD (detection time + minimum on-time + switching time) the external switch of the phase R is turned off. However, after 75 µs from the BD (detection time + switching time) the phases S and T are switched off and the respective output line currents start to decrease. Consequently, the current at the output of the HV diode rectifier does not increase anymore. After 150 µs from the BD (detection time + minimum on-time + 2 × switching time) also the internal switch of the phase R is turned off.
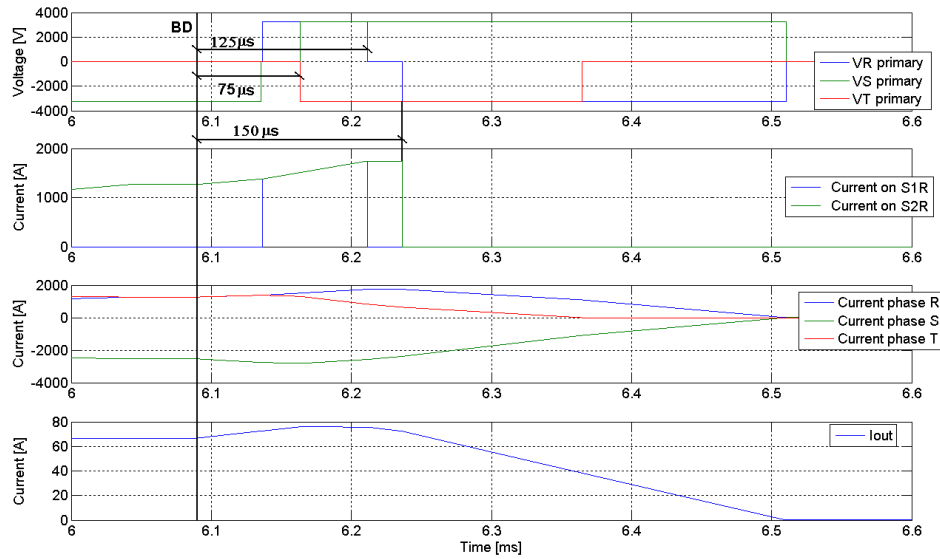
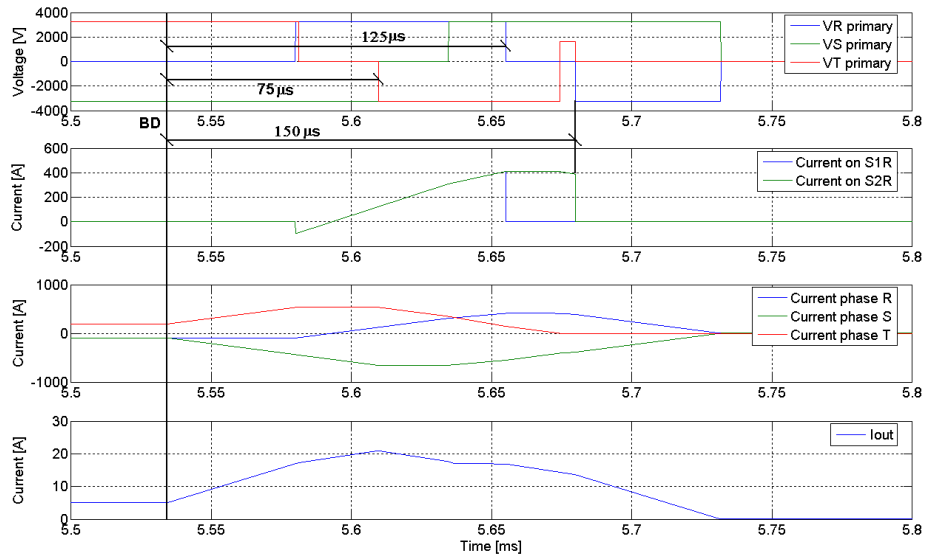*Figure 11-7 – Voltages and currents in case of grid BD with V_{dc}=6.5 kV, m=0.333 and I_{out}=66 A*

Figure 11-8 – Voltages and currents in case of grid BD with V_{dc}=6.5 kV, m=0.667 and I_{out}=5 A

From these simulations it can be noted that the over-current calculated with the eq. (11-2) is a bit overestimated, because the time derivative of the inverter output current starts to decrease 125 µs after the BD in the worst case (for the last commutating phase, R in Figure 11-7 and Figure 11-8). In addition, the time derivative of the current exiting from the HV diode rectifier starts to decrease 75 µs after the BD. In any case, eq. (11-2) can be used to estimate the over-current in the inverter switches, taking some margin. Therefore, about 5 kA (see Figure 11-6) is the current to be interrupted by the dc/ac inverter in the worst case (V_{dc} = 6.5 kV, rated dc output current for Hydrogen operation, first stage). From Table 7-3, it is clear that, considering the IGCT model ABB 5SHY 42L6500, if the reference time delays assumed here are confirmed, at least two inverters in parallel (or, alternatively, two IGCT in parallel for each switch in the same inverter) have to be used.

In addition to the current delivered by the HV diode rectifier, another contribution to the BD current comes from the HV dc-filter. In fact, because of the grid BD, the dc-filter capacitor discharges into the arc through the dc-filter resistor. Supposing the capacitor charged at 200 kV and neglecting the arc voltage, the peak of this current contribution can be easily calculated as follows:

$$I_{pk} = \frac{V_{outstage}}{R_f} = \frac{200kV}{68\Omega} = 2.94 \text{ kA} \tag{11-3}$$

After the peak, the current decays with an exponential law with a time constant $\tau_f = R_f \cdot C_f = 68$ $\Omega \cdot 300$ nF = 20.4 µs. The total charge transferred from the dc-filter to the arc can be calculated as:

$$Q_1 = C_f \cdot V_{outstage} = 300 \text{ nF} \cdot 200 \text{ kV} = 60 \text{ mC} \tag{11-4}$$

In the previous equations, C_f is the capacitance and R_f is the series resistance of the dc-filter. The charge contribution of the inverter to the arc during the time interval t_{delay} can be estimated from the time derivative of the current:

$$\frac{di_{out}}{dt} = \frac{2 \cdot V_{dc}}{n \cdot 2L_{tot2}} = \frac{6.5kV \cdot 18.2}{0.303H} = 0.39 \text{ A/µs} \tag{11-5}$$

in which V_{dc} = 6.5 kV is assumed. Considering a dc output current starting from the rated dc output current of the first stage (66 A for Hydrogen operation), without considering the ripple, the output current reaches the following peak value:

$$I_{pk}' = I_{rated} + \frac{di_{out}}{dt} \cdot t_{delay} = 66 + 58.5 = 124.5 \text{ A} \tag{11-6}$$

Starting from I_{pk}', in the second phase the output current decreases with the same slope of equation (11-5), but opposite in sign, and it is nullified after the time t' = I_{pk}' / (di_{out}/dt) = 319 µs (compare with Figure 11-6). Therefore the charge transferred from the inverter to the load can be calculated as follows:

$$Q_2 = \frac{I_{rated} + I_{pk}'}{2} \cdot t_{cut-off} + \frac{I_{pk}'}{2} \cdot t' = 14.3 + 19.9 = 34.2 \text{ mC} \tag{11-7}$$

Therefore, the maximum total charge transferred to the arc from the HV dc-filter and the dc/ac inverter can be estimated as:

$$Q_{tot} = Q_1 + Q_2 = 60 + 34.2 = 94.2 \text{ mC} \tag{11-8}$$

This result has been confirmed by simulation. However, a more precise calculation should take into account also the contribution of the core snubbers of the TL and the effect of the TL dumping resistances. In any case, this rough estimation is useful to have a first indication of the arc energy, to evaluate possible damages of the acceleration grids. It can be noted that in these calculations it is assumed the rated dc output voltage (for Deuterium operation) and current (for Hydrogen operation) at the same time. This condition could be possible in principle for a single stage, not for all the five stages together, because the rated power of the ac/dc conversion system (54.7 MW) is not sufficient.

11.3 Simulation of a beam-off

To quantify the DCG output voltages reached after a beam-off, a set of simulations has been performed with the simplified model of Figure 9-8. The nominal dc output voltages and currents for Deuterium operation (worst case) have been assumed (values of Figure 6-1). Moreover, the dc-link voltage is set to $V_{dc} = 6.5$ kV and the time delay between the beam-off and the turn off of all the inverter active switches is assumed to be $t_{delay} = 150$ μs (50 μs for the detection plus 100 μs for the switch-off, as required in section 6.1.5. The results are shown in Figure 11-9 and Figure 11-10, for two different instants of beam-off application. In the simulation of Figure 11-10, in particular, the beam-off is applied in correspondence of the peak of the step-up transformer secondary current.
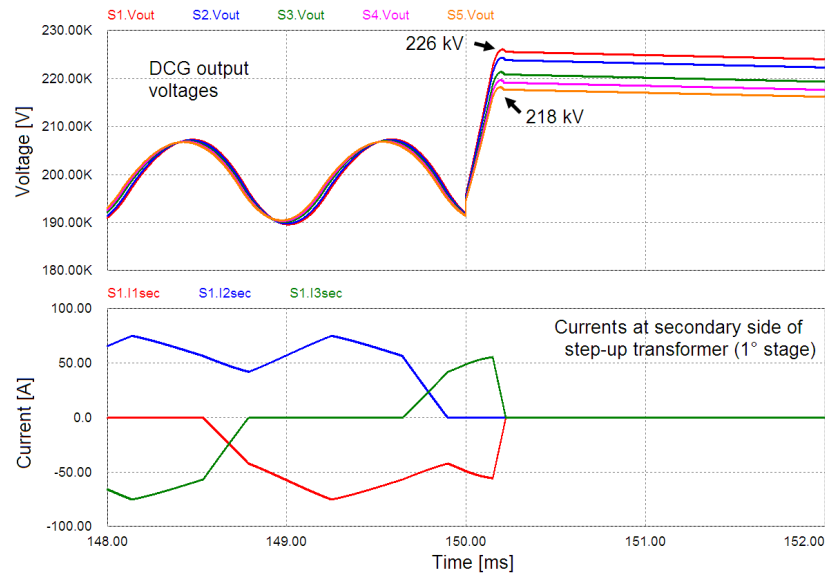

Figure 11-9 – Nominal D- operation: DCG output voltages and line currents at the secondary side of the step-up transformer caused by a beam-off applied at 150 ms. The gate commands of the inverters are removed 150 μs after the beam-off
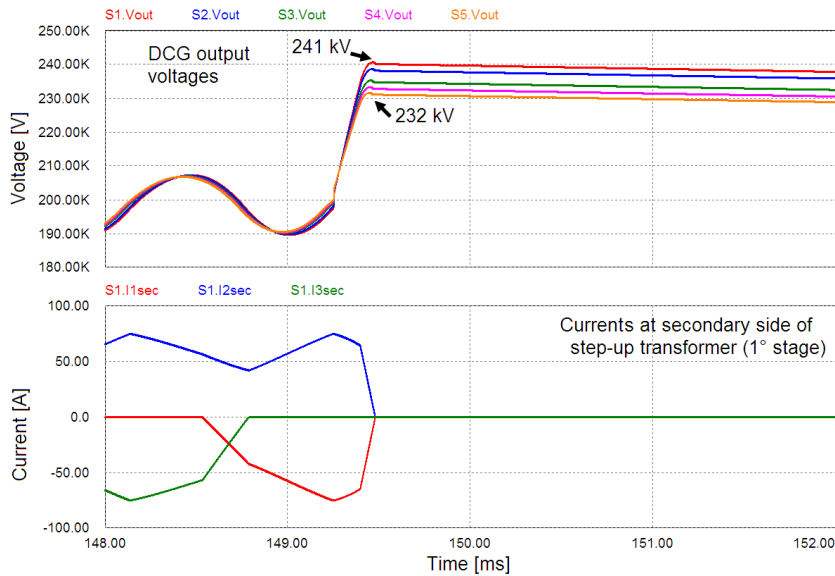
Figure 11-10 – Nominal D- operation: DCG output voltages and line currents at the secondary side of the step-up transformer caused by a beam-off. Here the beam-off is applied in correspondence to the peak of the step-up transformer secondary current. The gate commands of the inverters are removed 150 µs after the beam-off

Comparing Figure 11-9 and Figure 11-10, it is clear that the actual DCG output voltage reached after a beam-off depends on the instantaneous value of voltages and currents. In any case, the over-voltages obtained by simulation are similar to the value calculated in section 7.4 (ΔV_{out} = 33.7 kV).

The simulation of Figure 11-10 has been repeated with the AGPS detailed model of Figure 9-7, to quantify also the over-voltage on the dc-link. The results are shown in Figure 11-11.
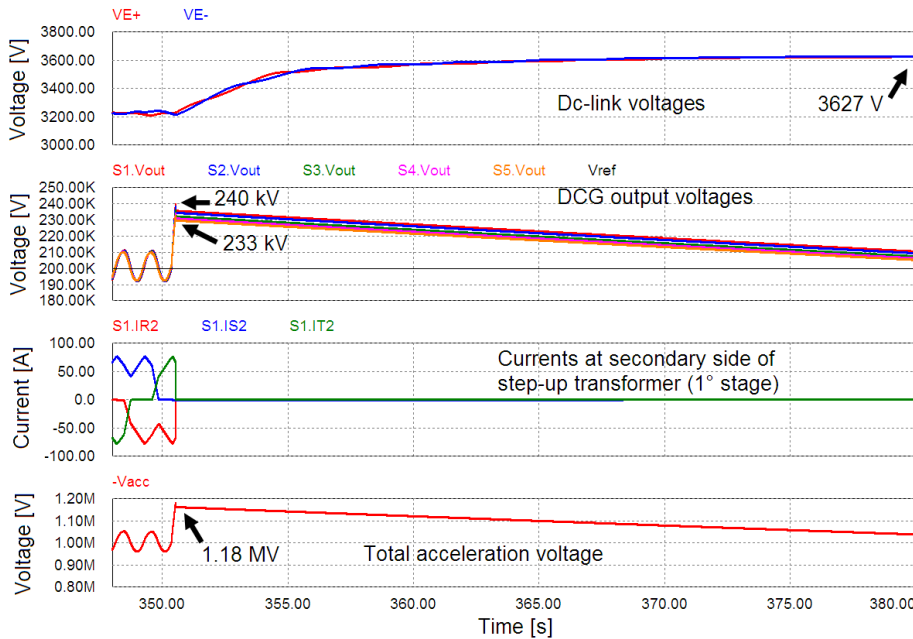

Figure 11-11 – Nominal D- operation: the beam-off is applied in correspondence to the peak of the step-up transformer secondary current. The gate commands of the inverters are removed 150 µs after the beam-off

The dc-link over-voltage is almost the same as in case of grid BD (compare with Figure 11-1). The DCG over-voltages also are almost equal to those calculated with the simplified model (Figure 11-10). The total acceleration voltage is the sum of the DCG output voltages, and it is lower than 120% of the nominal voltage (1.2 MV).

If the beam-off protection (based on plasma light, EGPS output current time derivative or AGPS current threshold) fails, a backup protection can be provided for each DCG stage based on the dc output voltage, as described in section 8.7: when the dc output voltage exceeds a certain threshold, the beam-off protection is triggered. In this case, the over-voltages can be obtained roughly by adding the threshold to the previous over-voltages. The voltage threshold has to be set sufficiently over the maximum dc output voltage in transient conditions (considering also the ripple), to avoid spurious activations of the protection. For example, it could be set at 110% of the nominal DCG output voltage, which gives a total acceleration voltage after beam-off up to 1.28 MV.

Of course, the case considered is not the worst among all the possible events (considering also the faults) in terms of over-voltages at the outputs of the DCG stages. In case of loss of control of the dc/ac conversion system, for example, the over-voltages could be much higher. A very interesting case, for example, could be the loss of control due to faulty measurements of the DCG output voltages. In the present design, in fact, these measurements are used both for the control of the dc/ac conversion system and for the over-voltage protection. For example, if the DCG output voltages are underestimated during the ramp-up of the acceleration voltages (without load), the modulation index of the dc/ac inverters could be increased up to m = 1 (single fault). Consequently, due to the resonance between the total equivalent inductances at the secondary side of the step-up transformers and the HV dc-filter capacitors, the acceleration voltage could reach 1.91 MV in 1.2 ms only, as shown in Figure 11-12.
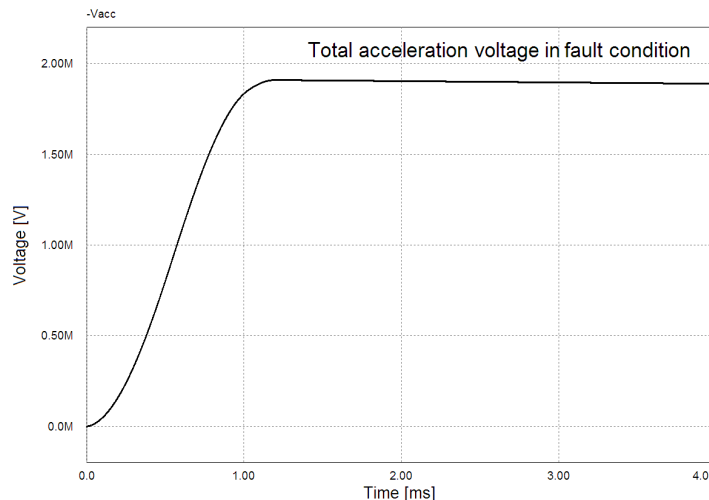

Figure 11-12 – Possible total over-voltage at the outputs of the DCG in case of faulty DCG output voltage measurements during ramp-up of the acceleration voltage without load, with V_{dc}=6.5 kV + 5%

The result is obtained with V_{dc} = 6.5 kV + 5%, being ±5% the maximum variation of the dc-link voltage in stationary regimes (see Table 6-7). Please note that, during ramp-up of the acceleration voltage without load, the beam-off protections based on EGPS output current time derivative and DCG output current threshold have to be inhibited by default.

To prevent the single fault condition described above, it would be advisable to use different voltage measurements for over-voltage protection and for dc/ac inverter control. In any case, before reaching the full over-voltage, surely some arc discharge would occur in the AGPS HV components or, more likely, between the acceleration grids. Moreover, some overvoltage passive suppressors (spark gaps, for example) could be foreseen in the AGPS HV components or inside the accelerator. The detailed design of these components is still in progress.

11.4 Simulation of beam modulation

As anticipated in section 6.1.6, the possibility to modulate the additional heating power transferred to the plasma in support to some diagnostics and/or as a tool to control in feedback relevant plasma parameters (e.g. beta parameter, rotation, etc.) has been investigated, in the framework of the ITER Design Change Request DCR-99. Two scenarios are envisaged for the modulation:

- continuous variation of the NBI operating parameters, to change by ±25% the NBI power around a nominal set-point value. Considerations regarding the energy confinement time of the ITER plasma suggest a required slew-time from +25% to -25% lower than 0.5 s. Figure 11-13 represents the concept; the precise waveform for the power modulation is not defined yet.
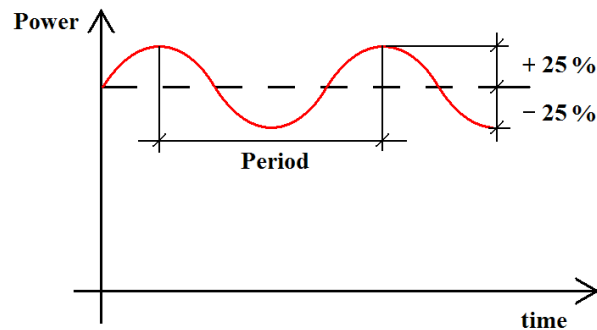

Figure 11-13 – Concept of continuous variation of the NBI operating parameters

- full on-off modulation, i.e. to turn on and turn off cyclically the beam power. In order to avoid excessive thermal cycling of the beam-line components of the NBI, the off-time has to be fixed to a value small compared with the smallest thermal time constant of such components. The on-time has to be programmable in the range spanning from the off-time up to one-third of the foreseeable ITER energy confinement time: a maximum on-time of 0.5 s can be assumed. For example, if the maximum off-time is 50 ms, then the on-time can be programmed from 50 ms (the average NBI power is

reduced by 50% with respect to the continuous operation) up to 500 ms (the NBI power is reduced by a factor 10/11).

Between the two options, the first one seems easier to obtain and less demanding for the present design of the NBI system. During this modulation, it is assumed that the optimum perveance must be preserved; therefore, the acceleration voltage and the beam current must be changed accordingly to eq. (4-1). Then, to reduce the power down to 50% with respect to the rated value, in Deuterium operation the acceleration voltage has to be decreased from 1 MV down to 750 kV and the total accelerated beam current (negative ions plus electrons) from 42 A to 27.2 A.

If during the modulation the ripple has to remain always inside ±5% of the output voltage with the dc/ac inverters synchronized in phase, the ac/dc conversion system and the dc/ac inverters must be controlled together by using the "Ripple controller" (see section 8.4). Otherwise, if a higher ripple may be accepted, it is possible to speed up the dynamics of the acceleration voltage by keeping constant the dc-link voltage. In this case, a ramp-up from 750 kV to 1 MV in 80 ms is possible, as a ramp-down from 1 MV to 750 kV in 80 ms. If a minimum on-time and off-time of 50 ms (as the maximum settling time required, from Table 6-2) is assumed, the maximum achievable modulation frequency is about 4 Hz. In Figure 11-14 the results of the simulation made with the simplified model of Figure 9-8 are reported, for a fixed dc-link voltage V_{dc} = 6.5 kV. The first row represents the output voltages of the five DCG stages together with the voltage reference (in black), and the second row represents the total accelerated beam current. The ripple measured at 750 kV is ±7.5%.
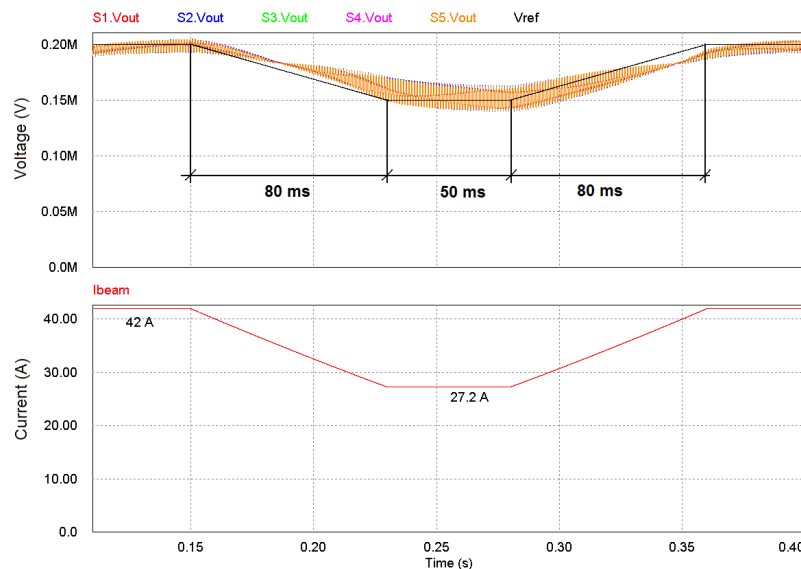
Figure 11-14 – Deuterium operation: modulation of the beam power by ±25% in perveance matching, with dc-link voltage fixed to V_{dc}=6.5 kV. First row: output voltages of the five DCG stages together with the voltage reference (in black). Second row: total accelerated beam current

Each time the acceleration voltage is varied, the resistor of the HV dc-filter is subjected to extra losses, also because of the higher ripple for lower voltages. The precise evaluation of

such extra losses depends on the waveform of the power modulation and it is not treated in this thesis.

In conclusion, from the AGPS point of view, the beam power modulation in the range ±25% by continuous variation of the NBI operating parameters seems feasible, with a maximum variation frequency around 4 Hz. In any case, the additional mechanical stresses on the beam-line components due to the modulation have to be carefully evaluated, as the impact of the modulated input power on the grid network.

The full on-off modulation is studied hereafter. To switch off the beam power, two ways can be envisaged. The first method is to switch off the inverters while maintaining the beam source current on, to discharge the HV dc-filter. With a total accelerated beam current of 42 A, a complete discharge requires about 2 ms. The situation is represented in Figure 11-15, where the first row shows the output voltage and the voltage reference of the five DCG stages, and the second row represents the total accelerated beam current. The dc/ac inverters are switched off at t = 100 ms and the beam current at t = 102 ms.

The ramp-up of the acceleration voltage to 1 MV requires 80 ms, as specified in Table 6-2. Assuming a minimum on-time of 50 ms (equal to the specified maximum settling time) and a minimum off-time of 20 ms (as the maximum time to be ready after a BD, Table 6-4), the resulting maximum modulation frequency is in the order of 7 Hz. The on-off dynamics is represented in Figure 11-16, where the first row represents the output voltage of the first DCG stage together with the voltage reference (in blue), the second row represents the total accelerated beam current and the third row shows the total beam power (approximated as the product of the total acceleration voltage by the total accelerated beam current). Both the Figures are obtained from a simulation with the simplified model of Figure 9-8, where the current during the start-up is regulated accordingly to the perveance matching law [eq. (4-1)].
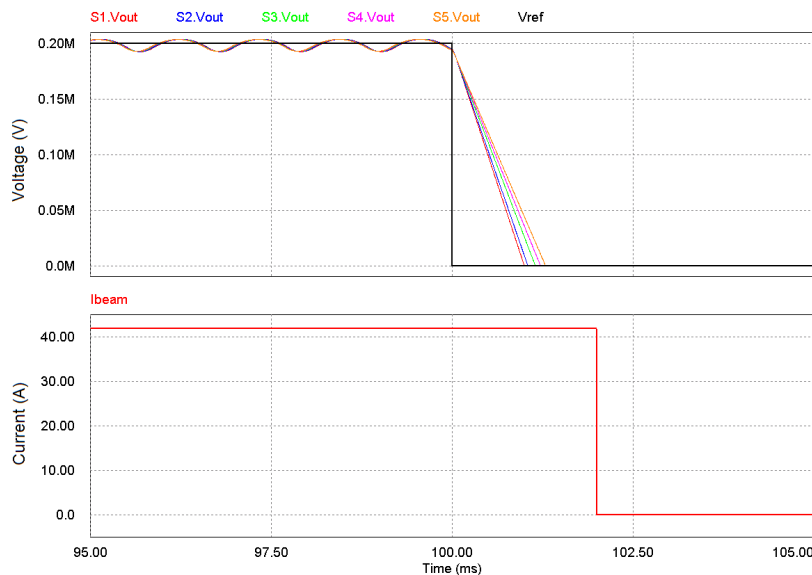

Figure 11-15 – Deuterium operation: discharge of the output HV dc-filters by means of the nominal grid currents. First row: output voltages of the five DCG stages together with the voltage reference (in black). Second row: total accelerated beam current
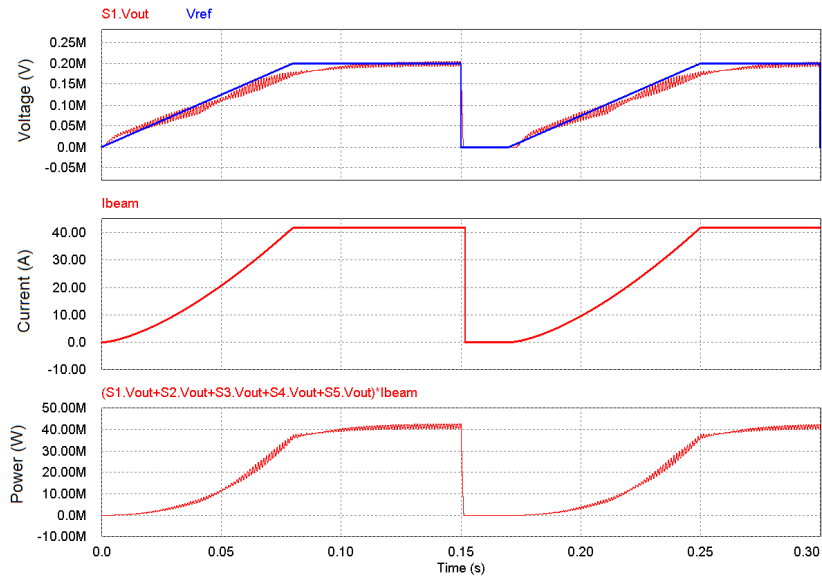
Figure 11-16 – Deuterium operation: on-off modulation of the beam power in perveance matching by discharging the HV dc-filter, with the dc-link voltage fixed to V_{dc}=6.5 kV. First row: output voltage of the first DCG stage and voltage reference (in blue). Second row: total beam current. Third row: total beam power

The second method consists in switching off the inverters, minimizing at the same time the RF power delivered to the ion source. In this way, the HV dc-filter remains charged to the same voltage value for a relatively long time. The situation is represented in Figure 11-17. The RF generator cannot be switched off completely, because the plasma inside the ion source shall remain ignited. Nevertheless, in principle the EGPS could be switched off, maybe nullifying the beam current. In the simulation of Figure 11-17 and in the following considerations, however, the extraction voltage is assumed to be kept almost constant, thus the beam current is considered to be reduced down to 10%, as the beam power.
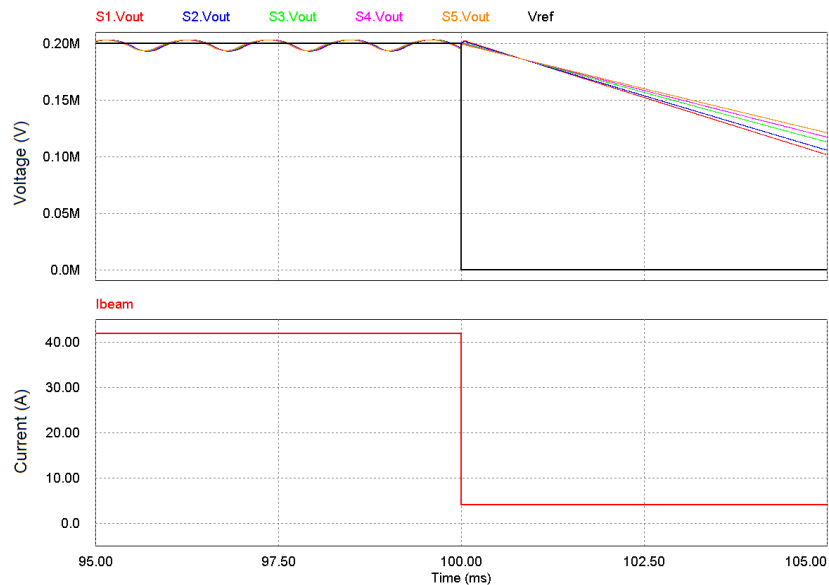

Figure 11-17 – Deuterium operation: the dc/ac inverters are switched off and the beam current is reduced to the minimum (10%) at the same time. A slow discharge of the HV dc-filter occurs. First row: output voltages of the five DCG stages together with the voltage reference (in black). Second row: total beam current

With this method, higher modulation frequencies can be achieved. In fact, the time necessary to reduce the beam power to the minimum is determined only by the dynamic performance of the ion source (and in particular the RF generators) and of the control system. This time has to be minimized, to avoid excessive discharge of the HV dc-filter. Some time after the RF power reduction (the maximum time to be ready after a BD), the RF power can be increased again, producing a ramp-up of the beam current. This corresponds to a beam start-up at maximum voltage (without perveance matching), as described in section 6.1.3. The ramp-up of the beam current may produce oscillations on the acceleration voltage, thus the rise time has to be chosen carefully. This constraint and the settling time of the acceleration voltage determine the minimum time in which the output power is higher than 10%.

An example of beam on-off modulation at fixed acceleration voltage is shown in Figure 11-18, where the total beam current is reduced to 10% for 1 ms and it ramps up to 100% in 3 ms. The actual settling time of the acceleration voltage in this case is around 6 ms, therefore, from this simulation, an on-off frequency up to 100 Hz seems achievable. However, the actual maximum frequency attainable depends on the dynamic performance of the real AGPS. In addition, it can be noted that the undershoot of the DCG output voltages during start-up of the beam current is lower than required maximum value (Table 6-2). In Figure 11-18, the first row represents the output voltages of the five DCG stages together with the voltage reference (in black), the second row represents the total accelerated beam current and the third row shows the total beam power.
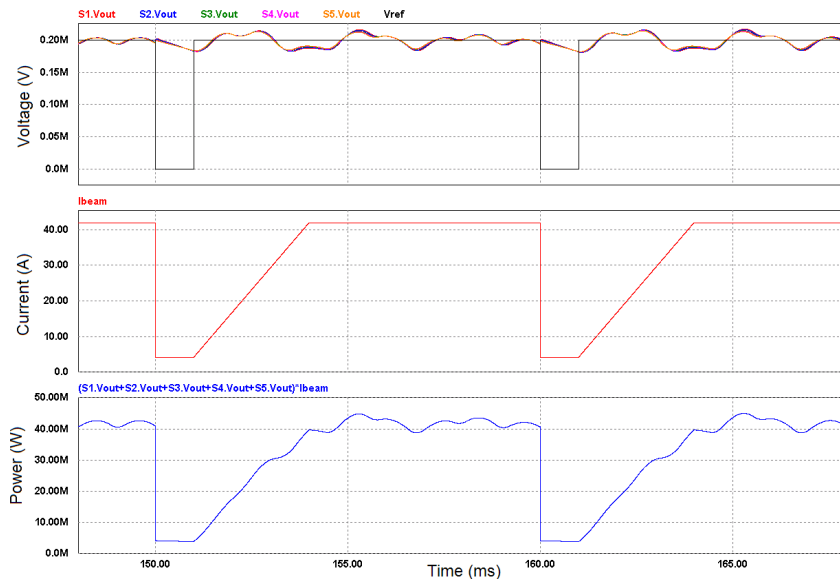
Figure 11-18 – Deuterium operation: on-off modulation of the beam power keeping charged the HV dc-filter, with the dc-link voltage fixed to V_{dc}=6.5 kV. First row: output voltage of the first DCG stage and voltage reference (in blue). Second row: total beam current. Third row: total beam power

An on-off modulation of such amount of power may produce stresses on the power supply grid. As far as the grid BD event is concerned, the fluctuations of the grid voltage were evaluated in previous studies [32] assuming 1 grid BD every 5 s. Here the situation is different, because the on-off beam modulation would be at higher frequency. A part for the voltage

oscillations, the on-off beam modulation could cause also network instabilities. For the European network, two ranges of frequency are found to be critical, since they excite intrinsic resonances in the grid: 0.3-0.4 Hz and 7-15 Hz. Although 60 MW probably would not be enough to excite instabilities, a specific analysis would be necessary.

In conclusion, the on-off modulation seems feasible from the AGPS point of view and, by keeping the acceleration voltage applied, it is possible to reach frequencies higher than 7 Hz by modulating only the beam current. Nevertheless, a quantification of the maximum performance achievable requires deeper investigations also on other components of the NBI (ion source, control system and so on).

12 Studies on CM voltage oscillations due to grid breakdowns

12.1 Introduction

During the normal operating conditions, the acceleration grids show frequent breakdowns. Consequently, high over-voltages appear across the internal conductors of the TL, and between the TL and the local ground, as demonstrated in [33]. In principle, such over-voltages could induce currents on the parasitic capacitances across primary and secondary side of the step-up transformers, and they could produce voltage and current fluctuations at the primary side, stressing the AGPS components. Therefore, it is important to assess these effects, which could have implications on some aspects as for example the protection strategy, the grounding philosophy and so on. Moreover, the results of these analyses are useful to define dedicated acceptance tests for the AGPS.

To obtain a rough estimation of such voltage and current oscillations, and the impact of the design choices, dedicated computer simulations, implemented on a high-frequency (HF) model of the AGPS-CS, have been carried out. A brief description of the model and a short discussion on the results achieved can be found also in [35].

12.2 High frequency model of AGPS-CS

In [33] a detailed model of the high voltage components has been presented, detailing the AGPS from the filter tank until the acceleration grids. With such model, the voltage oscillations of the return conductor of the TL with respect to the local ground have been calculated (CM voltage), together with the voltage oscillations across the five HV dc-filter stages (DM voltages). In the model of [33], the transient analyses have been made by charging the HV dc-filters at the nominal value, and discharging them on the arc breakdown.

In Figure 12-1, the DM voltages across the five dc-filter stages ($V_{DMstage1}$, $V_{DMstage2}$, $V_{DMstage3}$, $V_{DMstage4}$, $V_{DMstage5}$) obtained with the model of [33] are presented, together with the CM voltage oscillations (V_{GNDret}) due to a grid BD. These voltage waveforms have been obtained with the additional resistor connected as in the case a) of Figure 7-9. From this picture, it can be seen that the characteristic frequency of the oscillating voltages is in the order of some MHz. Therefore, the HF model of the AGPS-CS has been implemented including the parasitic elements that are relevant in the circuit at these frequencies.
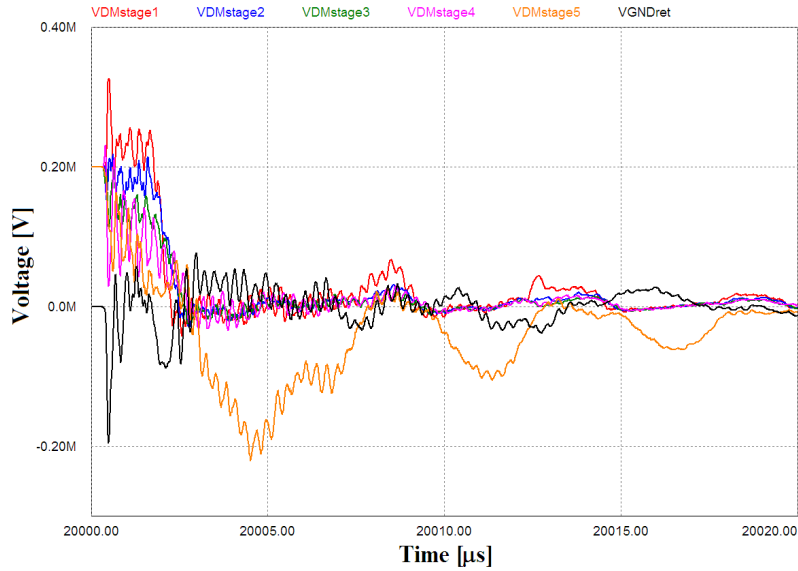
Figure 12-1 – DM (V$_{DMstage1}$, V$_{DMstage2}$, V$_{DMstage3}$, V$_{DMstage4}$, V$_{DMstage5}$) and CM (V$_{GNDret}$) voltages obtained in the HV dc-filter with the model described in [33]

The idea behind the analyses presented in this thesis is to apply these CM and DM voltages to a HF model of the AGPS-CS, in order to quantify the stresses on the components of the AGPS-CS. This process is justified by the Substitution Theorem [34] of the electrical network theory, which permits, with the provisions described in the following, to substitute all the passive components downstream the HV dc-filter terminals (TL, HVD1, accelerator and so on) with equivalent voltage generators applied at the same ports.

An overall view of the HF model of the AGPS-CS is represented in Figure 12-2. Here, the dc-link is represented by two ideal generators, 3.25 kV each. In fact, for the purpose of the transient analyses, due to the large dc-link capacitor bank, the dc-link voltage can be considered as constant. In the picture, the parasitic components are underlined.
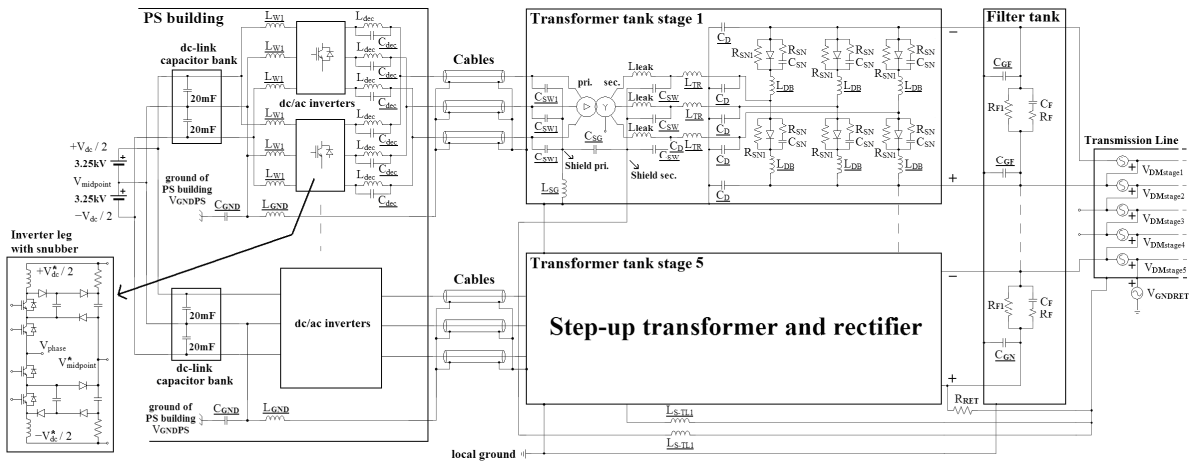

Figure 12-2 – Overall view of the HF model of the AGPS-CS. The parasitic components are underlined

In this model, all the components after the filter tank have been substituted by five DM voltage generators across the high voltage conductors ($V_{DMstage1}$, $V_{DMstage2}$, $V_{DMstage3}$, $V_{DMstage4}$, $V_{DMstage5}$) and a CM voltage generator between the return conductor of the TL and local ground (V_{GNDret}), and the voltage waveforms of Figure 12-1 have been applied.

To apply correctly the Substitution Theorem, the model here described shall represent the same load seen upstream the conductors of the HV dc-filter as in the model used to calculate the voltage waveforms of Figure 12-1. Therefore, having the model of Figure 12-2 the same topology at the secondary side of the step-up transformers of the model used to calculate the voltage waveforms of Figure 12-1, the same parameters have been used. Obviously, in the model of [33], the HF model of the AGPS-CS was not included. Nevertheless, the impact of the addition of the model of the AGPS-CS on the equivalent load seen upstream the HV dc-filter should be negligible.

To achieve the results of Figure 12-1, in the model of [33] as a first approximation the local ground near the step-up transformer tanks has been assumed connected to the ground plane of the TL through an equivalent resistance R_{ground}, quantified as 30 mΩ. In the model presented hereafter, the voltage V_{GNDret} applied downstream the filter tank (see Figure 12-1) represents the CM voltage with respect to the local ground of the transformer tanks, thus the resistance R_{ground} does not have any influence on the simulation results.

The model of Figure 12-2 has been implemented in PSIM^{TM}, resulting in the model of Figure 12-3. In this scheme, the dc/dc 200 kV generation stages (a part for the respective HV dc-filters) are represented as sub-blocks (S1, S2, S3, S4 and S5), shown in detail in Figure 12-4. Here, it is possible to identify the dc/ac inverter (S1), the connection cables (S3), the step-up transformer and the HV diode rectifier (S2), plus the stray inductances and capacitances considered in the circuit. To speed up the simulation, in the model the dc/ac inverter is not controlled in feedback, but directly from an external signal representing the modulation index.
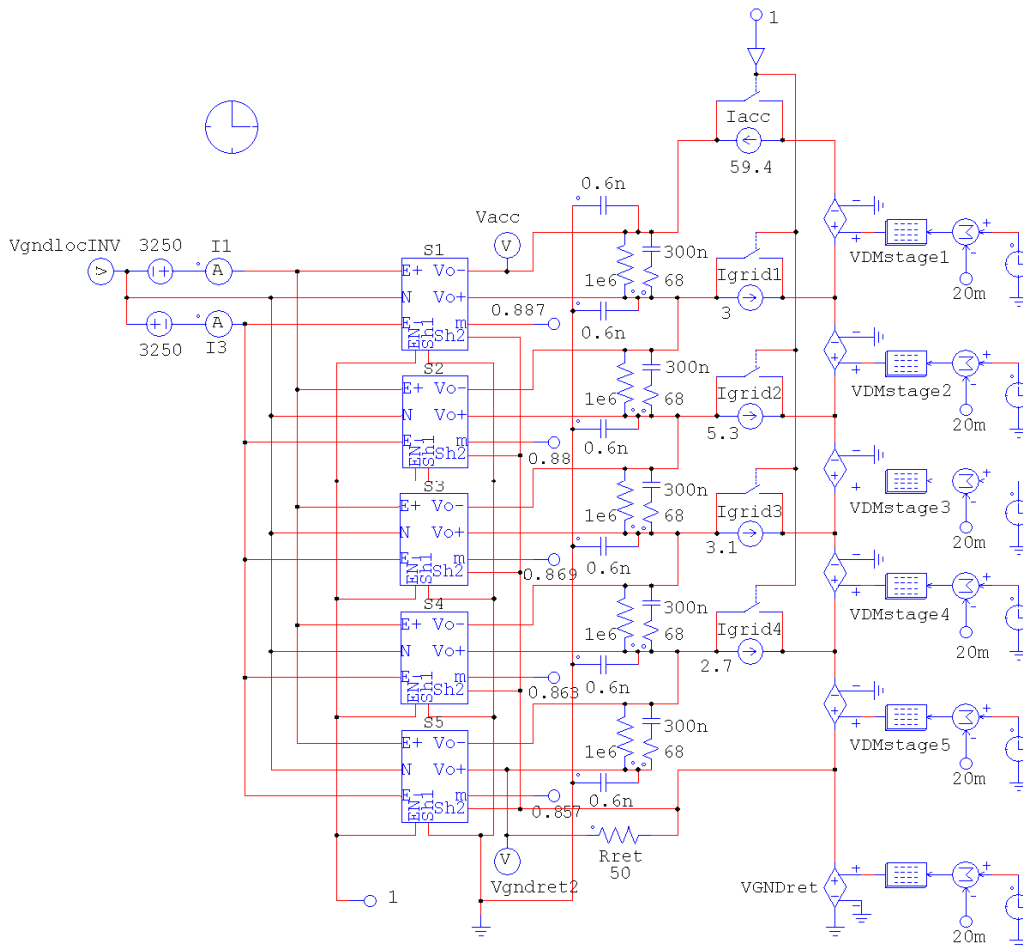
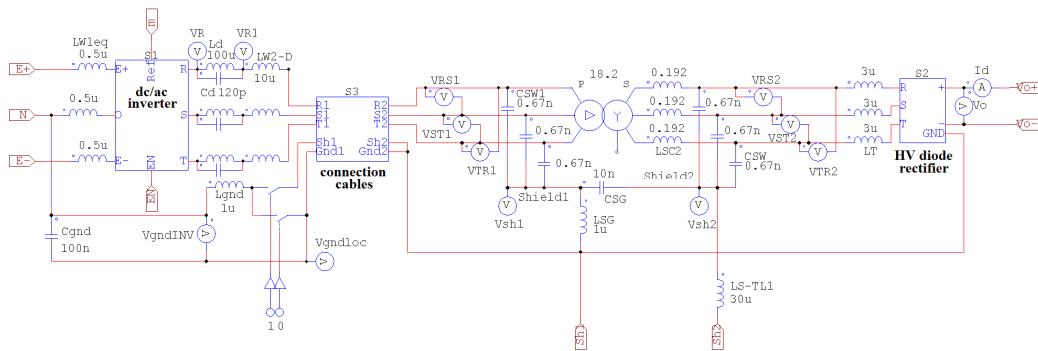*Figure 12-3 – Overall PSIM™ HF model of the AGPS-CS*

Figure 12-4 – PSIM™ HF model of a dc/dc 200 kV generation stage

In the following, the HF model is described in detail, and an estimation of the associated parameters is given.

12.2.1 AGPS layout and grounding assumptions

As already described in section 7.5, the return conductor of the TL is grounded at the tokamak building side, through the grounded grid, the beam-line vessel and the tokamak grounding. Conversely, the filter tank and the transformer tanks are connected to local ground. An insulating break is foreseen downstream the filter tank to separate the two different ground connections, as shown in Figure 7-9. In the same Figure, two possibilities are envisaged to connect the output terminal at the higher potential of the diode rectifier of stage 5 to the return conductor of the TL through the additional resistance R_{ret}: both the configurations have been simulated, and the results have been compared.

During the normal NBI operation, the central point of the dc-link and all the grounded metallic screens of the cubicles of the AGPS-CS are assumed to be connected to the local ground of the step-up transformer tanks through a certain path. The characteristics of such connection have a strong influence on the CM voltage oscillations of the AGPS-CS. To reduce the stray inductance of the grounding connection and then the CM voltage oscillations, the equivalent geometric area of the loops involved in the CM currents has to be minimized. Part of these loops is formed by the connection between the dc/ac inverters and the step-up transformers on one side, and the mentioned grounding connection on the other side. In order to minimize the geometric areas of the CM current path, it is assumed that normally the connection to ground of each stage is realized through the shields of the respective inverter output cables, connected to the AGPS cubicles on one side, and to the local ground of the step-up transformer on the other side.

For each stage, the stray inductance L_{gnd} of the connection between AGPS cubicles and the shields of the inverter output cables depends on the design of the dc/ac inverters, of the dc-link capacitor banks, of the cable trays and so on. Assuming a tentative distance between each grounding connection (five in total) and the surrounding earthed structures of about h_{gnd} = 1 m and an equivalent thickness R_{gnd} of the connecting busbar or cable of some cm, the stray inductance could be estimated with the following formula (valid for an infinite conductive plane):

$$l_{gnd} \cong \frac{\mu_o}{2\pi} \ln\left(\frac{2h_{gnd} - R_{gnd}}{R_{gnd}} \right) \cong \frac{\mu_o}{2\pi} \ln\left(\frac{2h_{gnd}}{R_{gnd}} \right) \cong 1 \text{ μH/m} \qquad (12\text{-}1)$$

If 1 m is tentatively assumed as the length of each grounding connection, the stray inductance can be estimated as L_{gnd} = 1 μH for each stage. The stray resistance of such connections has been neglected, being the inductive component probably dominant at the frequencies of interest.

The capacitance C_{gnd} in the model represents the stray capacitance of the capacitor bank of each stage with respect to the ground of the PS building. An estimation of this capacitance can be made on the basis of the measures carried out on the 40 mF capacitor banks of the power supply system for the toroidal circuit of RFX-mod. Each elementary capacitor of this

system, 1 mF rated for 4 kV, is based on paper-oil insulation and enclosed in a dedicated grounded metallic box ($35 \times 980 \times 190$ mm). Basing on the measurement (100 nF) of the real stray capacitance with respect to ground of one of such capacitor banks, the stray capacitance of each 1 mF capacitor can be calculated as 100 nF $\times$ 1 mF / 40 mF = 2.5 nF. Being the surface area of each capacitor element equal to 1.89 m^2 and assuming a relative dielectric constant of 2.5 for the oil, the internal distance between the capacitor armatures and the respective tank should be about 1.6 cm, which seems a reasonable value. Being the rated voltage and capacitance quite similar, if the same technology is assumed, a tentative estimation of the stray capacitance of the dc-link capacitor bank of each AGPS-CS conversion stage (two 20 mF banks in series, in the present assumption) could be made starting from the measurements made in RFX-mod, therefore C_{gnd} = 100 nF is assumed. This capacitance should include also the stray capacitances of the crowbars. Their values cannot be predicted now, but probably they are much lower than those of the capacitor banks, so in this study they are neglected. Nowadays, also different capacitor technologies could be envisaged, based for example on different dielectrics. Nevertheless, for this study, only the paper-oil technology is considered.

The power section of each inverter stage has to be insulated with respect to ground in order to withstand to the over-voltages that occur during a BD, estimated in this thesis. The insulation requires a certain distance, which reduces the stray capacitances of each inverter power section with respect to its cubicle, which in turn is assumed to be connected to the local ground of the step-up transformer through the shields of the inverter output cables. Moreover, these capacitances are presently very difficult to estimate, because they strongly depend on the real structure of the inverter assembly. Therefore, for all these reasons, these stray capacitances are disregarded.

About the stray inductance of the connections between the dc/ac inverters and the dc-link capacitor banks, it strongly depends on the layout of the AGPS-CS. If these connections are included into the AGPS cubicles, assuming a tentative distance between each busbar (or cable) and cubicle of 1 m, an equivalent thickness of the busbar (or cable) of some cm and a total length of the connection of 1 m, the stray inductance could be estimated with eq. (12-1), obtaining L_{W1} = 1 µH. Being two dc/ac inverters grouped in a single inverter stage, in the model of Figure 12-4 two stray inductances L_{W1} have been grouped in a single equivalent inductance L_{W1eq} = 0.5 µH (neglecting the mutual coupling between the connections).

The mutual stray inductances of the connections among the grounded parts of the AGPS cubicles are unknowns, depending on the distances among the cubicles, the type of connections (cable, busbars, grounding plane or others), the respective positions and other layout details. Probably these inductances are quite negligible with respect to the other inductances involved in the rest of the CM current path, thus they are not included in the model.

About the step-up transformers, two electrostatic shields are foreseen between the primary and secondary windings, as in [28]. The shield facing the secondary winding is connected to

the return conductor of the TL through a cable having an inductance L_{S-TL1} estimated as 30 µH. The shield facing the primary winding is assumed being connected to the transformer tank through a connection having an equivalent stray inductance $L_{SG} = 1$ µH. The transformer tanks are connected to the local ground through a path assumed having a negligible stray inductance, as in [33]. The values used for L_{S-TL1} and L_{SG} are the same used to calculate the voltage waveforms of Figure 12-1 with the model of [33]. In particular, the equivalent inductance L_{SG} is a crucial parameter, because the connection to ground of the shield facing the primary side is a major path through which the CM currents injected from the secondary windings are shunted to local ground.

12.2.2 Model for the NPC inverters

Figure 12-5 shows the HF model used for one leg of a NPC inverter. Considering the frequencies of interest, the model has to include at least the snubbers and clamps that probably will be foreseen in the final design. However, the topology and the parameters of the snubbers and clamps are under the responsibility of the Supplier and the assumptions taken here are tentative only.

In the model, the slope of the switching current is reduced by the series inductors L_1 and L_2, 6 µH each. The parasitic capacitances of these inductors are considered negligible. The capacitors C_{1-1}, C_{1-2}, C_{2-1}, C_{2-2}, together with the diodes D_{1-1}, D_{1-2}, D_{2-1}, D_{2-2}, form a clamp circuit for the voltages across the switches S_1, S_2, S_3, S_4, D_1, D_2. The energy accumulated during the clamp action is discharged through the resistances R_1 and R_2. The values of the passive components have been designed (and verified by simulation) to achieve a good compromise between the necessity to limit the over-voltages on the power switches and to minimize the power losses on the snubber.
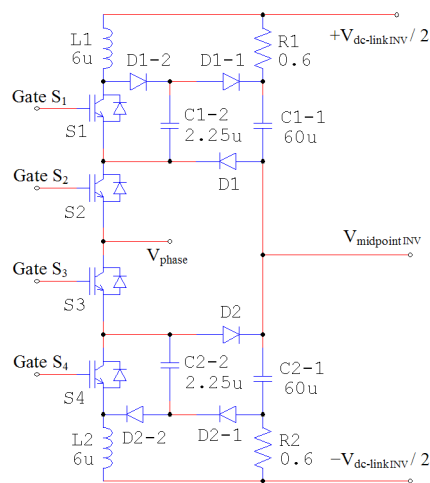

Figure 12-5 – Model of a NPC inverter leg with snubbers

The HF model of a complete AGPS dc/ac inverter stage is shown in Figure 12-6. It represents the sub-block S1 of the overall model of Figure 12-4. In the present reference design, two

inverters in parallel are foreseen for each stage. Nevertheless, to speed up the simulation, in the HF model they are represented as a single inverter. Therefore, compared to the model of a single leg of Figure 12-5, in the model of Figure 12-6 the values of the snubbers have been multiplied by 2 (for the capacitors) or divided by 2 (for the resistances and the inductances).
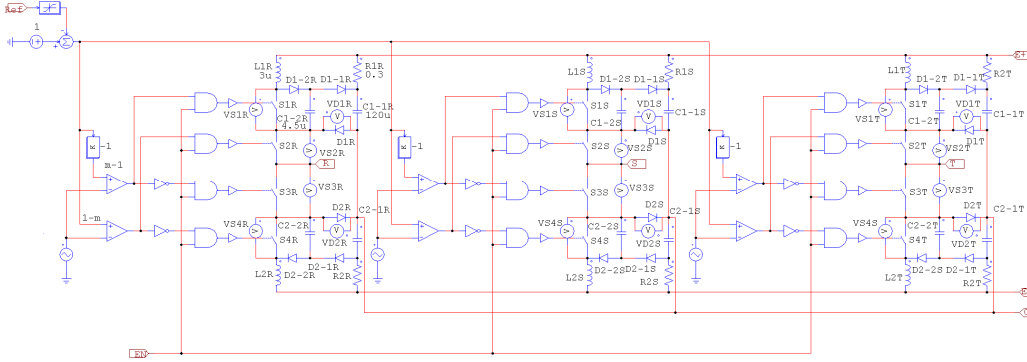

Figure 12-6 – PSIM™ HF model of a dc/ac inverter stage

12.2.3   Model for the inverter decoupling inductances

In the present reference design, two NPC inverters in parallel are foreseen for each stage, the respective outputs being decoupled by proper inductors. The total inverter output inductance is L_{inv} = 110 μH (see Table 6-7) = L_d + L_{W2-D}, in which L_d = L_{dec} / 2 = 100 μH is associated with the two decoupling inductors in parallel, and L_{W2-D} = 10 μH represents the stray inductance of the connections between the dc/ac inverter and the respective output cables plus the DM stray inductances of the cables themselves.

In transient conditions, the stray capacitances associated to the inductances L_{dec} could have an important impact on the results. To evaluate such capacitances, some simple considerations have been carried out, basing on the measured stray capacitance (about 40 pF) of the inter-phase reactances of the ac/dc converters of RFX-mod (nominal inductance 175 μH). Such capacitances have been scaled up considering the different current rating and inductance value assumed for the inverter decoupling inductors, obtaining the following value:

$$C_{dec} = 40\,pF \times \sqrt{\frac{1700/2}{290}} \times \sqrt{\frac{175}{200}} \cong 60\,pF \tag{12-2}$$

In this formula, 290 A is the rated dc current of the RFX reactances. The stray capacitance has been scaled up taking into account a linear increase of the section of the conductor with the rated current (and then the inter-turn equivalent facing area scales with the square-root) and a square-root increase of the number of turns with the inductance (and then a corresponding reduction of the stray capacitance). In this scaling law, the inter-turn insulation thickness is assumed comparable in the two cases.

The impedance of the inductance L_{dec} becomes comparable with the impedance of the stray capacitance C_{dec} for frequencies higher than some MHz.

As already mentioned, in the model of Figure 12-4 two dc/ac inverters per stage are represented with a single inverter. Therefore, the two capacitances C_{dec} are represented with a single capacitance $C_d = C_{dec} \times 2 = 120$ pF.

12.2.4 Model for the shielded cables

The inverter outputs are connected to the primary windings of the step-up transformers by means of shielded cables, as foreseen in [28]. Assuming unipolar cables for simplicity, the following parameters have been derived from the data-sheet of a commercial product [36]:

Voltage rating: U_o/U = 6/10 kV

Nominal cross-section: 1×300 mm^2

Diameter of the conductor: 20.7 mm

Insulation thickness: 3.4 mm, polymer

Current carrying: 605 A (if buried underground, for grouped cables)

Capacitance: 0.52 µF/km @50 Hz (between the active conductor and the shield)

Phase reactance: 0.095 Ω/km @50 Hz (for grouped cables)

Being 1700 A the rated rms inverter output current (see section 7.3), at least three cables in parallel for each phase have to be used. Considering the layout for ITER and PRIMA described in section 5.5 and section 5.6, a minimum cable length of about 30 m is tentatively assumed. Longer cables should reduce more the CM voltage oscillations, due to the shunting effect of the CM currents through the stray capacitance between inner conductor and cable shield, as shown in the following.

Regarding the phase inductance, the following value can be obtained for three grouped cables:

$$L_{W2-D} = \frac{0.095 \cdot 30}{1000 \cdot 2\pi \cdot 50 \cdot 3} = 3\,\mu H \quad @50Hz \tag{12-3}$$

For the frequency of interest, the more conservative value L_{W2-D} = 10 µH for each phase is used, accordingly to [28] and with the previous section (including the stray inductance of the connections between the dc/ac inverter and the respective output cables).

In the HF model, the cables have to be represented as transmission lines, having the following parameters per unit length for each cable.

- Resistance per unit length of the internal cable (@1 MHz):

$$r_{in} = \frac{\sqrt{\pi f \rho \mu}}{2\pi R_1} = \frac{\sqrt{\pi \times 1 \cdot 10^6 \times 2 \cdot 10^{-8} \times 4\pi \cdot 10^{-7}}}{2\pi \cdot 0.0104} = 4.3\ m\Omega/m \tag{12-4}$$

In this formula, R_1 is the outer radius of the internal conductor (10.4 mm) and only the skin effect is taken into account. A frequency of the current oscillations around 1 MHz and the resistivity ρ of the copper are assumed.

In the following formulas, R_2 is the radius of the shield (10.4 + 3.4 = 13.8 mm), and h is the distance between the center of the cable and an ideal conducting plane representing the earth below the cable. For h, two opposite cases have been taken into account, to evaluate its influence on the results: the case 1), in which the cables are buried underground at a distance h = 10 cm with respect to the earth; the case 2), in which the cables are suspended overhead at the same height of the bushings at the primary side of the step-up transformers (h = 4.7 m).

- Inductance per unit length associated with the flux between the internal conductor and the shield:

$$l_{in-sh} = \frac{\mu_o}{2\pi} \ln\left(\frac{R_2}{R_1}\right) = 57 \text{ nH/m} \tag{12-5}$$

- Capacitance per unit length between the internal conductor and the shield:

$c_{in-sh} = 0.52 \text{ nF/m}$

- Self-inductance of the shield with respect to an ideal conducting plane:

$$l_{sh-gnd} = \frac{\mu_o}{2\pi} \ln\left(\frac{2h - R_2}{R_2}\right) \cong \frac{\mu_o}{2\pi} \ln\left(\frac{2h}{R_2}\right) = \tag{12-6}$$

540 nH/m for h = 10 cm
1.30 μH/m for h = 4.7 m

- Capacitance of the shield with respect to an ideal conducting plane:

$$c_{sh-gnd} = \frac{2\pi\varepsilon_o}{\ln\left(\frac{2h - R_2}{R_2}\right)} \cong \frac{2\pi\varepsilon_o}{\ln\left(\frac{2h}{R_2}\right)} = \tag{12-7}$$

21 pF/m for h = 10 cm
8.5 pF/m for h = 4.7 m

To implement in PSIM™ the model of the cables, it has been supposed to discretize the TL model into five cells, as a compromise between the computational time and the accuracy of the results.

Supposing to have three 30 m parallel connected cables for each phase, the parameters for each cell can be calculated as follows:

$R_{W2} = r_{in} \times 30 / (3 \times 5) = 8.6 \text{ m}\Omega$ (12-8)
$L_{W2} = l_{in-sh} \times 30 / (3 \times 5) = 114 \text{ nH}$ (12-9)
$C_{W2} = c_{in-sh} \times 30 \times 3 / 5 = 9.4 \text{ nF}$ (12-10)
$L_{G2} = l_{sh-gnd} \times 30 / (3 \times 3 \times 5) = 360 \text{ nH for h = 10 cm, 870 nH for h = 4.7 m}$ (12-11)
$C_{G2} = c_{sh-gnd} \times 30 \times 3 \times 3 / 5 = 1130 \text{ pF for h = 10 cm, 460 pF for h = 4.7 m}$ (12-12)

The resistance R_{W2} of the inner conductors and the resistance of the shields are neglected with respect to the impedance of the inductances L_{W2} and L_{G2} at 1 MHz.

By neglecting the resistivity of the ground and by approximating the inductive coupling between inner conductor and respective shield with the self-inductance of the shield itself (as in the model used in [33] for the TL), the equivalent model of Figure 12-7 can be derived. This model represents the sub-block S3 of Figure 12-4).

It can be noted that the stray inductances L_{G2} and capacitances C_{G2} are lumped in a single component for the three phases, being the shields connected in parallel.
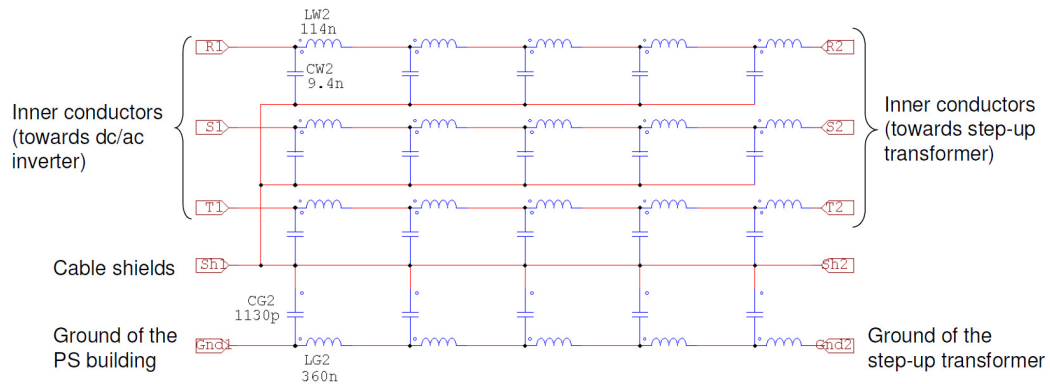

Figure 12-7 – PSIM™ HF model of the cable connections between the dc/ac inverter and the step-up transformer, for a single stage

12.2.5   Model for the step-up transformers

The equivalent leakage inductance at the secondary side L_{SC2} = 0.194 H of the step-up transformers, represented in Figure 12-4, is specified in Table 6-7.

The stray capacitance C_{SW} between each phase of the secondary winding of the step-up transformers and the secondary shield is assumed equal to 2 nF / 3 = 0.67 nF, in agreement with the model of [33]. For the sake of uniformity, also the stray capacitance C_{SW1} between each phase of the primary winding of the step-up transformers and the shield at the primary side is assumed equal to 0.67 nF. For a more precise estimation of this capacitance, a detailed electrostatic model of the step-up transformer would be necessary, which however would require information on mechanical details of the device not available at the moment. The stray capacitances between the windings and the transformer tanks are neglected, as in [33].

The capacitance C_{SG} between the two shields facing respectively the primary and the secondary windings of the step-up transformers is one of the most critical parameters, because it represents the major path through which the voltage fluctuations are transmitted from the secondary to the primary side. In the following simulations, C_{SG} = 10 nF is assumed, as in [33], basing on the indications given by JADA.

12.2.6 Model for the HV diode rectifiers

The step-up transformers are connected to the respective HV diode rectifiers by means of connections having an estimated stray inductance $L_{TR} = 3$ µH, as in the model of [33]. The diode rectifiers are represented in Figure 12-4 with the sub-block S2, shown in detail in Figure 12-8.

Each valve is assumed being composed by a series of 180 diodes (total voltage drop estimated as 270 V), having in parallel an equivalent R-C snubber composed by an equivalent resistance $R_{SN} = 3$ MΩ and an equivalent capacitance $C_{SN} = 0.42$ nF. In parallel to the diodes, also some resistances are provided, to facilitate the voltage sharing between the devices. Each diode valve is assumed having an equivalent stray inductance $L_{DB} = 1$ µH $\times$ 3 = 3 µH (in agreement with the model of [33]), which includes also the stray inductance of the connections to the filter tank. The stray capacitances C_D between the diode rectifier components and the diode tank are neglected, as in [33].
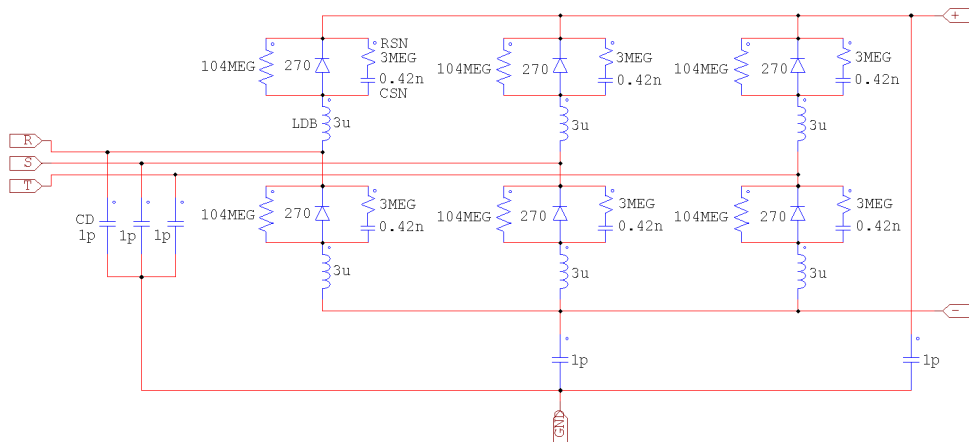

Figure 12-8 – PSIM™ model of the HV diode rectifier

12.2.7 Model for the dc-filter

The outputs of the HV diode rectifiers are connected to the HV dc-filter installed in the filter tank. The values of the R-C filter ($C_f = 300$ nF, $R_f = 68$ Ω) and of the stray capacitances between the filters and the tank ($C_{gf} = C_{gn} = 0.6$ nF) are the same assumed in the model of [33].

12.3 Results

All the following simulations have been done for nominal Deuterium operation only. In fact, this is the worst case regarding the voltage and current oscillations after a grid BD, because of the higher acceleration voltage with respect to Hydrogen operation. Moreover, in all the simulations it is assumed the additional resistance R_{ret} being connected as in case a) of Figure 7-9. Simulations with the connection as in case b) have been performed also, and the results are quite similar than for the case a).

12.3.1 Achievement of the steady-state condition

A first simulation has been carried out to reach the steady-state condition, in order to verify the proper working of the switching model and to obtain the correct initial status of the circuit for the following breakdown simulation (voltages in the capacitors, currents in the inductors). To reduce the computational time, the modulation indexes of the dc/ac inverters necessary to obtain the nominal acceleration voltage with the nominal current distribution on the grids (for Deuterium operation) have been tentatively derived and applied in the simulation. In this way, starting from dc-filter capacitors discharged, the steady state condition is reached in about 20 ms. At this time, in the simulation the switches S_{3R} and S_{4R} of the five inverters (see Figure 7-2) are off. Thus, the voltage across these switches will be analyzed in the following simulations to assess the voltage stresses on the IGCT due to a grid BD.

12.3.2 Reference BD simulation

Starting from the status of the circuit saved from the previous simulation, a new simulation has been carried out with a reduced time step (5 ns). The current generators are short-circuited by means of ideal switches, and the voltage generators $V_{DMstage1}$, $V_{DMstage2}$, $V_{DMstage3}$, $V_{DMstage4}$, $V_{DMstage5}$ and V_{GNDRET} are applied.

In this simulation, the values $L_{gnd} = 1$ µH and $L_d = 100$ µH are assumed. The AGPS-CS is grounded through the shields of the cables connecting the inverter decoupling inductances to the step-up transformers, and the cables are located at h = 10 cm with respect to ground.

The voltage oscillations resulting from the simulation are represented in Figure 12-9. Here, in row a) the DM and CM voltages applied to the filter tank are shown (same as Figure 12-1). Row b) shows the potential of the shields of the step-up transformers facing the primary side, with respect to the ground of the transformer tanks. In row c) the potentials of the phases R measured downstream the decoupling inductances are represented, whereas row d) shows the voltage oscillations measured directly at the output of the dc/ac inverters. Both the voltages of rows c) and d) are referred to the local ground of the PS building. The row e) represents the potential of the central point of the capacitor bank for each stage, with respect to the local ground of the PS building. Row f) represents the potential of the local ground of the PS building with respect to the ground of the transformer tanks.

From this simulation, it can be noted that the oscillations of the potential of the shields facing the primary side are very high, in the order of 60 kV. Nevertheless, most of the CM current is shunted to ground by the shields of the inverter output cables, therefore the oscillations of the potential of the midpoint of the dc-link capacitor bank are small, in the order of 60 V.

Rows g) represents the voltages across the switches S_{3R} (referring to Figure 7-2) for the five stages. It can be seen that the over-voltages are clamped by the clamp circuits across the components. By simulation, the voltage oscillations across the switches S_{4R} are equal to zero.
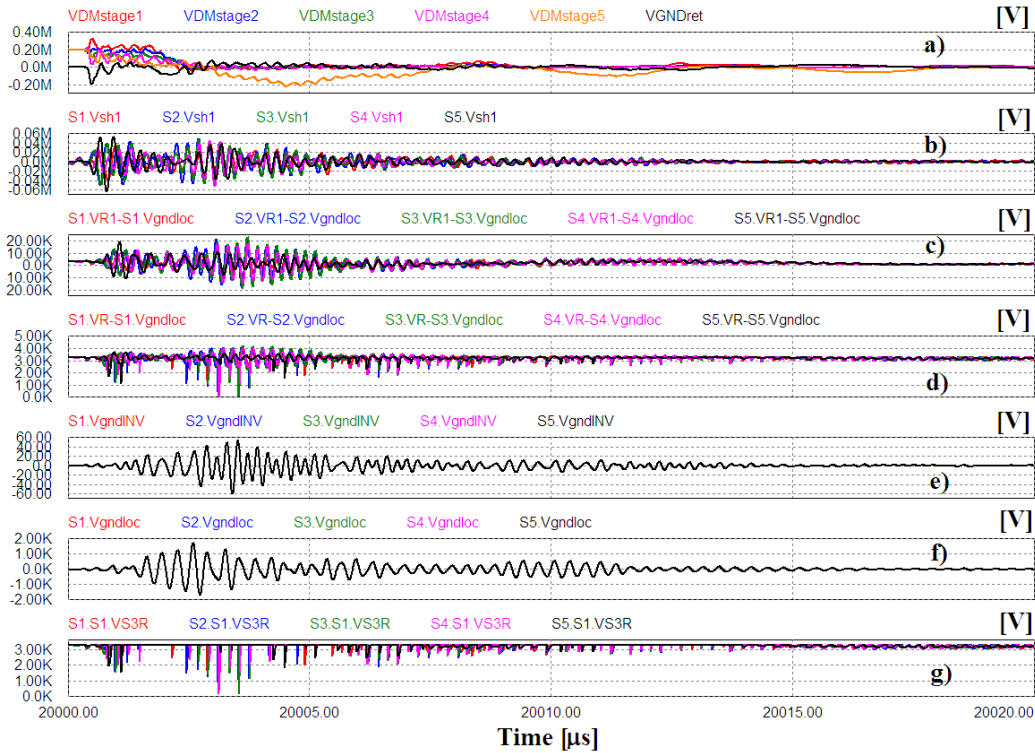
Figure 12-9 – Voltage and current waveforms after a BD with L_gnd=1 μH, L_d=100 μH, h=10 cm, AGPS-CS grounded through the cable shields and additional resistance R_ret in the position of case a). Row a): CM and DM voltages applied across the dc-filter terminals. Row b): potentials of the shields of the step-up transformers facing the primary side, with respect to the ground of the transformer tanks. Row c): potentials of the phases R measured downstream the decoupling inductances, with respect to the ground of the PS building. Row d): potentials of the phases R measured directly at the output of the dc/ac inverters, with respect to the ground of the PS building. Row e): potential of the central point of the capacitor bank for each stage, with respect to the ground of the PS building. Row f): potential of the local ground of the PS building with respect to the ground of the transformer tanks. Row g): voltages across the switches S_3R for the five stages

The following table resumes the estimation of the amplitudes of the CM voltage oscillations measured at different points of the circuit in the reference case, with all the assumptions made in this section.

Table 12-1 – Maximum voltage stresses on different positions of the AGPS-CS caused by a BD, in the reference case

Row of Figure 12-9	Maximum absolute value [V]	Description
c)	21 kV	Voltage downstream the decoupling inductances of the dc/ac inverters with respect to the ground of the PS building
d)	4.2 kV	Voltage at the output the dc/ac inverters with respect to the ground of the PS building
e)	60 V	Voltage of the central point of the dc-link capacitor bank with respect to the ground of the PS building
f)	1.7 kV	Voltage of the ground of the PS building with respect to the local ground of the step-up transformers

12.3.3 Study of the impact of the shields and the position of the inverter output cables

To verify the influence of the height of the inverter output cables with respect to ground, a simulation has been carried out with h = 4.7 m, leaving all the other parameters unchanged. With respect to the previous case, the equivalent impedance of the CM current path through the ground is increased. However, most of the CM current flows through the shields of the inverter output cables, therefore only small changes in the voltage oscillations are foreseen. In fact, by simulation it is visible just a little reduction in the voltage oscillations of the central point of the dc-link capacitor bank with respect to the ground of the PS building (now 48 V), because of the little reduction of the CM current. At the same time, the small increase of the impedance of the connection of the central point of the dc-link to the ground of the step-up transformer produces a small increase of the voltage oscillations across the two grounds (now 2.2 kV).

A further simulation has been carried out after disconnecting the shields of the inverter output cables at both ends. It is assumed that such cables are located at h = 10 cm from the ground, and that the shields of the three phases are still connected each other. Moreover, the AGPS-CS is assumed being grounded through a connection to the ground of the PS building, having an equivalent stray inductance L_{gnd} = 1 μH for each stage.

The results are shown in Figure 12-10. Here, the shunting effect of the cable shields to the CM current is missing and, at the same time, the impedance of the connections of the AGPS-CS to the local ground of the step-up transformers is increased. Therefore, for similar voltage oscillations of the transformer shields facing the primary side, the oscillations of the ground of the PS building with respect to the local ground of the step-up transformers (row f) are very high, in the order of tens of kV. Moreover, being increased the CM currents flowing through the AGPS-CS, also the voltage oscillations of the reference points of the AGPS-CS with respect to the ground of the PS building is increased, up to 490 V (row e). The situation is similar also for h = 4.7 m, as proven by simulation.
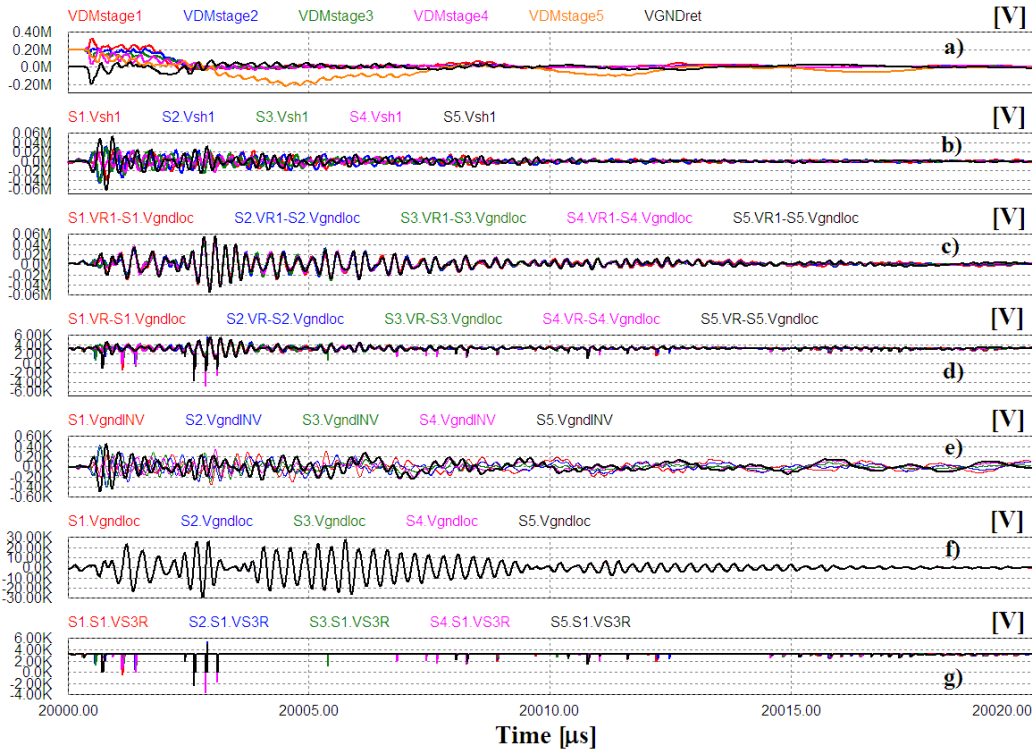
Figure 12-10 – Voltage and current waveforms after a BD with L_{gnd}=1 μH, L_d=100 μH, h=10 cm, cable shields disconnected at both ends and additional resistance R_{ret} in the position of case a). AGPS-CS grounded through a connection to the ground of the PS building, having an equivalent stray inductance L_{gnd}=1 μH for each stage. Row a): CM and DM voltages applied across the dc-filter terminals. Row b): potentials of the shields of the step-up transformers facing the primary side, with respect to the ground of the transformer tanks. Row c): potentials of the phases R measured downstream the decoupling inductances, with respect to the ground of the PS building. Row d): potentials of the phases R measured directly at the output of the dc/ac inverters, with respect to the ground of the PS building. Row e): potential of the central point of the capacitor bank for each stage, with respect to the ground of the PS building. Row f): potential of the local ground of the PS building with respect to the ground of the transformer tanks. Row g): voltages across the switches S_{3R} for the five stages

12.3.4 Study of the impact of the inverter output decoupling inductances

To verify the impact of the decoupling inductances, a new simulation has been produced after removing such inductances, thus assuming L_d = 0 μH. All the other parameters are the same as in the reference simulation of Figure 12-9. The results are shown in Figure 12-11: they are quite similar to those of Figure 12-9. This means that the value of the decoupling inductances has not a great impact on the CM current amplitude, due to the respective stray capacitances, which reduce the actual impedance of the device at the characteristic frequency of the CM currents.
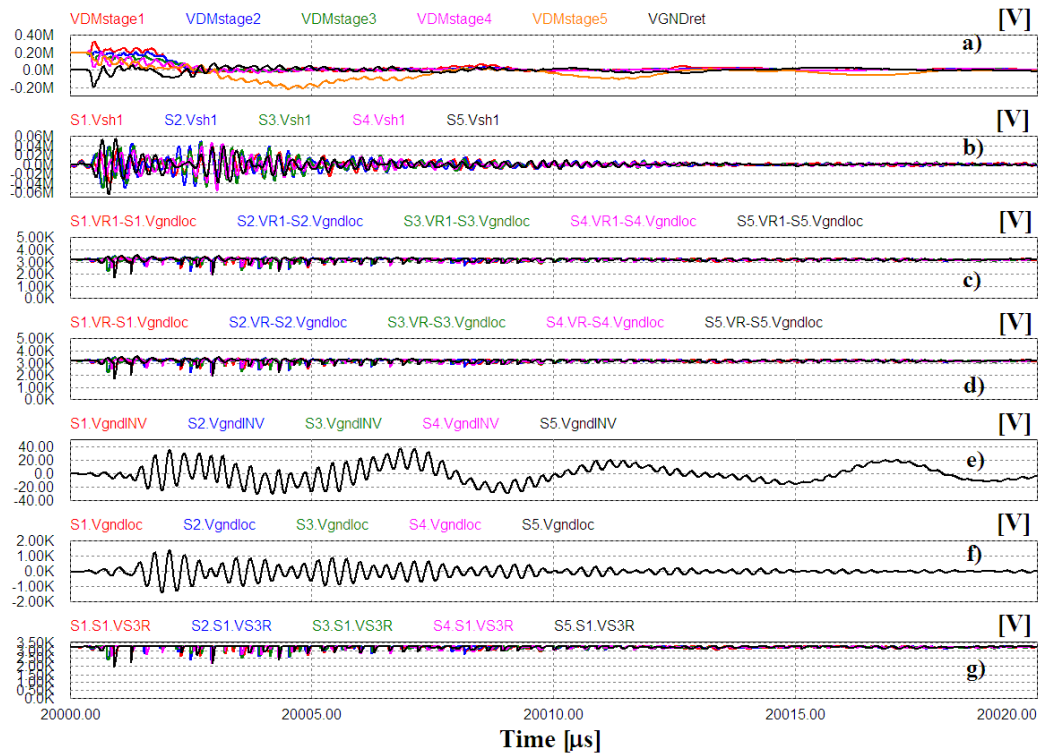
Figure 12-11 – Voltage and current waveforms after a BD with L_{gnd}=1 µH, L_d=0 µH, h=10 cm, AGPS-CS grounded through the cable shields and additional resistance R_{ret} in the position of case a). Row a): CM and DM voltages applied across the dc-filter terminals. Row b): potentials of the shields of the step-up transformers facing the primary side, with respect to the ground of the transformer tanks. Row c): potentials of the phases R measured downstream the decoupling inductances, with respect to the ground of the PS building. Row d): potentials of the phases R measured directly at the output of the dc/ac inverters, with respect to the ground of the PS building. Row e): potential of the central point of the capacitor bank for each stage, with respect to the ground of the PS building. Row f): potential of the local ground of the PS building with respect to the ground of the transformer tanks. Row g): voltages across the switches S_{3R} for the five stages

12.4 Conclusions

From the analyses and the results of the simulations carried out with the HF model of the AGPS-CS presented in this section (including the results of other simulations not shown here for the sake of brevity), the following conclusions can be derived.

To reduce the CM voltage oscillations of the AGPS-CS with respect to the local ground of the step-up transformers, it is important to minimize the impedance of the connections of the AGPS-CS to such ground. Therefore, the stray inductance of these connections, represented in the model as L_{gnd}, have to be minimized. Moreover, in this sense it is useful to minimize the geometric area of the loops involved in the CM current return path. To do that, a good way is to ground the AGPS-CS through the shields of the inverter output cables. This solution would permit also to shunt part of the CM current directly to the local ground of the step-up transformers through the stray capacitances between the conductors and the respective shields. A similar effect could be achieved also by means of bypass capacitors connected between the primary windings of the step-up transformers and local ground.

If the AGPS-CS is grounded through the shields of the inverter output cables, the position of such cables with respect to ground does not have an important impact in the CM voltage oscillations.

The electrostatic shields facing the primary side of the step-up transformers are very useful to shunt to local ground most of the CM currents induced by the voltage oscillations at the secondary side. However, these shields are effective only if they are grounded through a low impedance connection.

The snubbers on the dc/ac inverters are very useful and effective in clamping any over-voltage across the switches caused by a grid BD. The use of snubbers with voltage clamping action is recommended.

The decoupling inductances at the output of the inverter stages could be not so effective in reducing the CM voltage oscillations at the inverter side due to a grid BD. In fact, depending on the mechanical design, the respective stray capacitances could strongly reduce the actual impedance of the device at the characteristic frequencies of the voltage oscillations (some MHz).

The position of the additional resistance that connect the return conductor of the TL to the output terminal of the HV diode rectifier (case a) or b), referring to Figure 7-9) does not influence so much the voltage oscillations on the AGPS-CS caused by a grid BD.

13 Studies on tests to be performed on AGPS

13.1 Design of AGPS dummy loads

13.1.1 Introduction

The AGPS-CS will be delivered before the DCG system. Therefore, the AGPS dc/ac inverters have to be tested without having the DCG. For this reason, proper dummy loads (DL) have to be provided. In [25], three-phase inductive DL are foreseen, including three-phase short-circuiting devices based on three making switches, to simulate the grid BD. The scheme of one of these DL is represented in Figure 13-1.
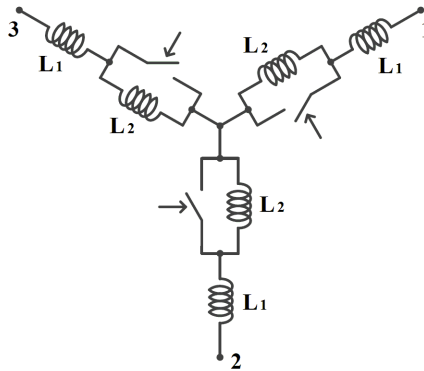

Figure 13-1– Scheme of one AGPS-CS inductive DL

In [25] it is specified that the value of the equivalent impedance with the making switches open ($L_1 + L_2$), shall be selected so that the inverter stage supplies the nominal current. The value of the equivalent impedance with the making switches closed (L_1) shall be selected so that the time derivative of the inverter current is equal to that supplied in case of a short-circuit downstream of the DCG. L_1 is selected on the basis of the short-circuit impedance of the step-up transformers, the impedance of the connections between the transformers and the inverters and the inverter decoupling inductances.

From [25], the short-circuiting devices shall be triggerable by an external source. The trigger command shall be given both manually and by the AGPS-CS control.

To limit volume and cost of the DL, the specified duty cycle is 5 s every 600 s, at the nominal current. Clearly, this means that the steady-state temperatures in the power components of the AGPS dc/ac inverter cannot be reached. Therefore, an exhaustive thermal test of the inverters with DL is impossible.

13.1.2 Calculations for inductive dummy loads

In the following, the electrical parameters of the inductive DL will be calculated and verified by simulation.

In order to test the AGPS inverters at the rated operating conditions, the inductance of the inductive DL should be designed in order to achieve the inverter rms rated output current (H-operation). Instead, for the sake of simplicity, in this study the inductive DL is designed to have

the same equivalent impedance of the inverter nominal load, for m = 1. After calculation, it is verified by simulation that also the rms currents with the inverter rated load and with the DL are similar. In these simplified calculations, the inverter decoupling inductances, the transformer leakage inductances and the HV dc-filter are neglected.

With m = 1, the rated dc output voltage (174 kV) and current (66 A) for the first stage (H-operation) are reached with V_{dc} = 5386 V. The voltage and current waveforms at the primary and secondary sides of the step-up transformer with this dc-link voltage and m = 1 are shown in Figure 13-2.
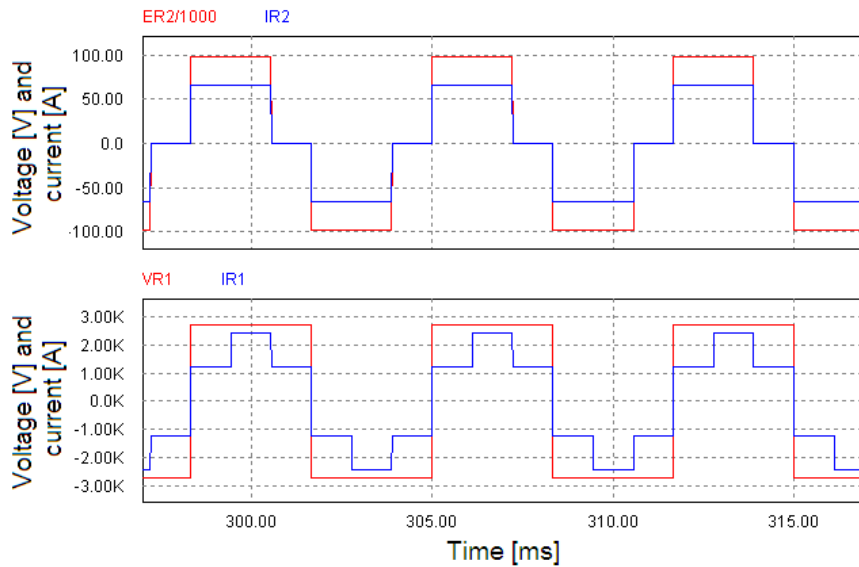

Figure 13-2 – Voltage and current waveforms for m=1 and V_{dc}=5386 V, rated H- operation, first stage. First row: phase to neutral voltage (red, divided by 1000) and line current (blue) at the step-up transformer secondary side. Second row: phase voltage (red) and phase current (blue) at the output of the AGPS inverter. The inverter decoupling inductances, the transformer leakage inductances and the HV dc-filter are neglected

The equivalent impedance of the rated load for the first stage (at the secondary side of the step-up transformer) can be calculated as the ratio between the plateau values of voltage and current (which have the same waveform, in phase):

$$Z_2 = \frac{V_{dc}}{n \cdot I_d} = \frac{98025}{66} = 1485 \ \Omega \qquad (13\text{-}1)$$

This obviously corresponds also to the ratio of the first harmonic amplitudes of voltage and current at the secondary side. In the ideal case considered here (the inverter decoupling inductances and the transformer leakage inductance are neglected), this impedance is a pure resistance. Then, it can be translated to the primary side:

$$Z_1 = Z_2 \cdot \frac{n^2}{3} = 1.494 \ \Omega \qquad (13\text{-}2)$$

From this impedance, the equivalent DL inductance for the first stage can be derived as:

$$L_{DL} = \frac{Z_1}{2 \cdot \pi \cdot f} = \frac{1.494}{2 \cdot \pi \cdot 150} = 1.586 \text{ mH} \qquad (13\text{-}3)$$

where f = 150 Hz is the fundamental frequency of the output voltage and current waveforms. In the following, it is assumed that this inductance includes also the total output inductance of the AGPS inverters (110 µH, inverter decoupling inductance plus cable leakage inductance).

Verification of the rms current with m=1 and V_{dc}=5386V

To verify that the inductive DL (having the inductance value calculated above) produces a rms current very similar to the rated inverter rms output current, a simulation with inductive DL has been carried out with the PSIM™ model represented in Figure 13-3.
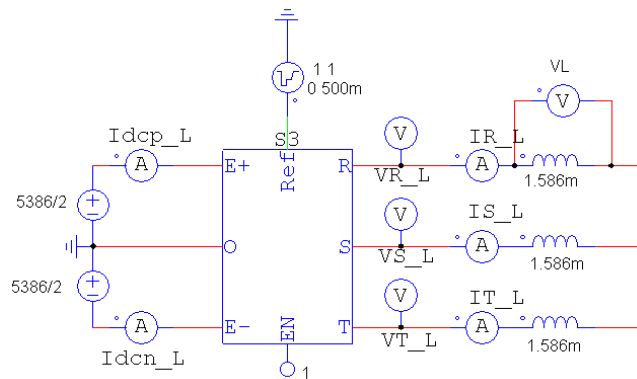

Figure 13-3 – PSIM™ model with the inductive DL, for the first stage

To avoid high dc current component on the load, caused by the absence of dissipative elements, the modulation index m shall be slowly ramped up from 0 to 1 (in 100 ms, in the simulation). This fact shall be taken into account also in case of a test on the real system.

The inverter output currents (for m = 1, V_{dc} = 5386 V, rated H- load) are compared in the first line of Figure 13-4. The rms value of the inverter output current with inductive DL is 1628 A, which is very close to the value corresponding to the rated H- operation (1666 A, as from the simulation of section 10.3.1).
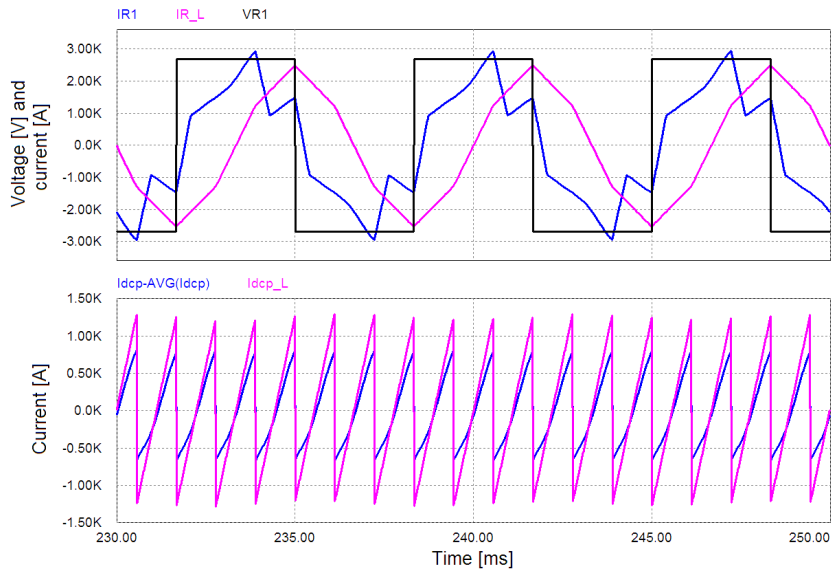
Figure 13-4 – Comparison of the currents with inductive DL (pink) and for the rated H- operation (blue), with m=1 and V_{dc}=5386 V, for the first stage. First line: inverter output currents and, in black, inverter output phase voltage. Second line: dc-link output current ripple (from the positive terminal)

From the first line of Figure 13-4, it is evident the phase lag of the inverter output current in case of inductive DL, with respect to the rated Hydrogen operation. The corresponding reactive power is provided by the dc-link capacitors, which in fact have to deliver higher rms currents, as shown in the second row of Figure 13-4 (726 A rms against 450 A rms).

Currents in the switches with m=1 and V_{dc}=5386V

In Figure 13-5, the currents in the inverter power switches in case of inductive DL are compared with those for the rated Hydrogen operation (same as 10.3.1), for m = 1 and V_{dc} = 5386 V. The currents in the freewheeling diodes are zero in both cases.
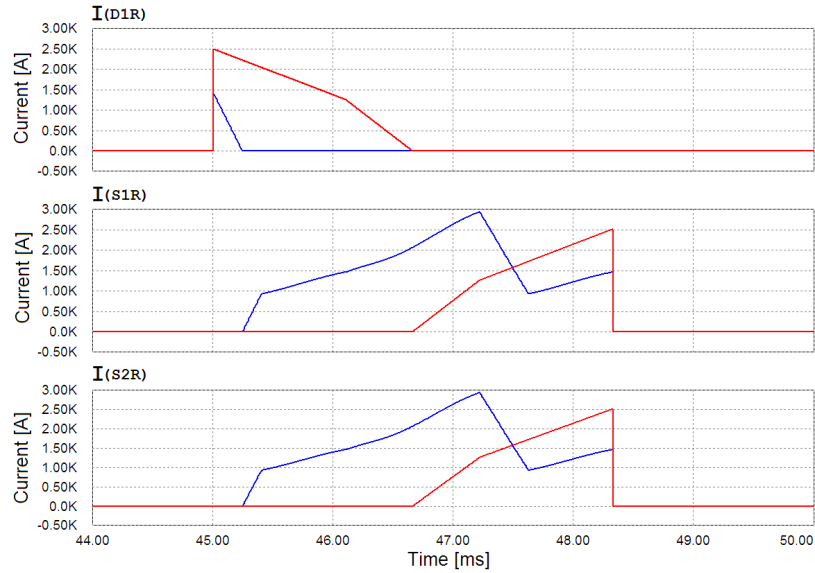
Figure 13-5 – NPC inverter switch currents for m=1 and V_{dc}=5386 V, first stage. First row: current in the anti-parallel diodes. Second row: current in the external active switches. Third row: current in the internal active switches. In blue, the rated H- operation. In red, the case of inductive DL

The respective average, rms and switch-off currents are compared in Table 13-1.

Table 13-1 – Currents in the inverter power switches with m=1 and V_{dc}=5386 V, for the first stage

Device	I_{avg} [A]		I_{rms} [A]		Switch-off current [A]	
	Inductive DL	Rated H-operation	Inductive DL	Rated H-operation	Inductive DL	Rated H-operation
Anti-parallel diodes (D1x, D2x)	366	27	810	162	0	0
External active switch (S1x, S4x)	366	739	810	1167	2500	1462
Internal active switch (S2x, S3x)	366	739	810	1167	2500	1462
Freewheeling diodes (DF1x, DF2x)	0	0	0	0	0	0

Comparing the waveforms and the values, it can be noted that the anti-parallel diodes are much more stressed in case of inductive DL with respect to the rated H- operation. The higher current is due to the reactive power delivered to the inductive DL. Conversely, the average and rms currents in the active switches are lower, but the switch-off current is higher.

Therefore, it can be concluded that the inductive DL cannot reproduce the same current waveforms as in the rated H- operation, resulting in overstresses of the components, especially the anti-parallel diodes. Consequently, to reproduce similar transient thermal stresses on the anti-parallel diodes, higher inductance values should be used for the DL, reducing consequently the value of the inverter rms output currents delivered to the DL itself.

13.1.3 Calculations for resistive/inductive dummy loads

In this chapter, a set of resistive-inductive (R-L) DL is proposed. These DL should be able to reproduce the rated operative conditions of the respective AGPS dc/ac inverter stage, i.e. the same rms output currents and similar switching conditions for the inverter power switches. In particular, the inductance is chosen to reproduce the same voltage/current phase shift at the load.

To reduce the power requested to the grid network and to limit its volume and cost, it is proposed a R-L DL rated for a reduced duty-cycle: 1 s every 900 s. Therefore, as for the inductive DL, with these devices would not be possible to test exhaustively the AGPS dc/ac inverters from the thermal point of view.

As for the inductive DL, the reference scenario is the rated H- operation, with m = 1.

The inductive component L_1 of each DL can be chosen as equal to L_{tot1} (see section 7.4 and section 11.2), which represents the total equivalent inductance at the primary side of the step-up transformer.

$$L_1 = L_{tot1} = L_{inv} + L_{SC2} \frac{n^2}{3} = 110 \cdot 10^{-6} + 195 \cdot 10^{-6} = 305 \text{ µH} \tag{13-4}$$

The L_1 inductance includes also the inductance L_{inv}, which represents the parallel of the inverter decoupling inductances and the cables stray inductances. Should these inductances be present in the real case, their value has to be subtracted from L_1 to obtain the effective value of the DL inductance.

The equivalent phase resistance of the load can be calculated starting from the equivalent load impedance at the secondary side calculated with eq. (13-1) (for the first stage), as follows:

$$R_2 = \sqrt{Z_2^2 - (2\pi \cdot 150 \cdot L_{tot2})^2} = 1457 \ \Omega \tag{13-5}$$

From R_2, the resistive component R_1 of the DL can be chosen as:

$$R_1 = R_2 \cdot \frac{n^2}{3} = 1.47 \ \Omega \tag{13-6}$$

The active power to be dissipated by the DL of the first stage (at the inverter rated rms output current) is:

$$P_{DL} \cong 3R_1 \times I_{INV}^2 = 3 \cdot 1.47 \cdot 1700^2 = 12.7 \text{ MW} \tag{13-7}$$

Verification of the rms current with m=1 and V_{dc}=5386V

To verify that the R-L DL having the resistance and inductance calculated above produces a rms current very similar to the rated inverter rms output current, a simulation with R-L DL has been carried out with the PSIM™ model represented in Figure 13-6.
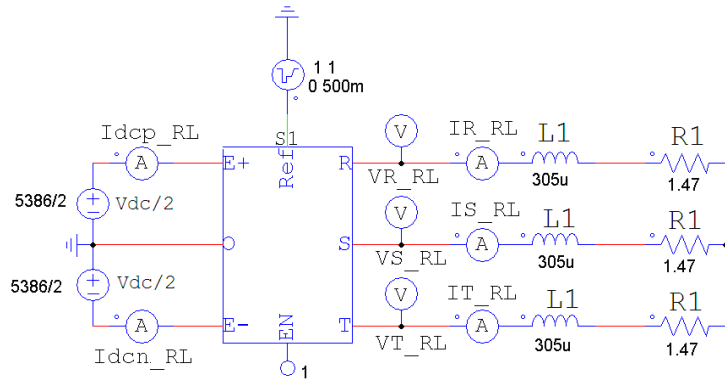

Figure 13-6 –PSIM™ model with the R-L DL, for the first stage

The inverter output currents with R-L DL and for the rated H- operation, first stage (for m = 1, V_{dc} = 5386 V) are compared in the first line of Figure 13-7. The rms value of the inverter output current with R-L DL is 1644 A, which is very close to the value corresponding to the rated H- operation (1666 A, as found in section 10.3.1).
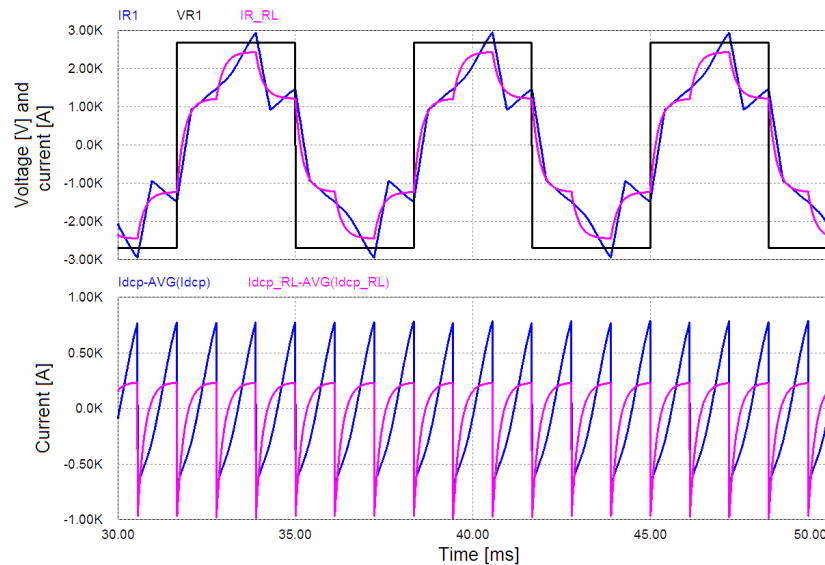

Figure 13-7 – Comparison of currents with R-L DL (pink) and for the rated H- operation (blue), with m=1 and V_{dc}=5386 V, for the first stage. First line: inverter output currents and, in black, inverter output phase voltage. Second line: dc-link output current ripple (from the positive terminal)

On the first line of Figure 13-7, a part for the over imposed oscillations due to the HV dc-filter, the output currents in the reference case and with R-L DL seem comparable. Moreover, the

current ripple from the dc-link capacitors is also lower (297 A rms against the 450 A rms of the reference case).

Currents in the switches with m=1 and V$_{dc}$=5386V

In Figure 13-8, the currents in the inverter power switches in case of R-L DL are compared with that for the rated H- operation (same as section 10.3.1), for m = 1 and V$_{dc}$ = 5386 V (first stage). The current in the freewheeling diodes is zero in both cases.

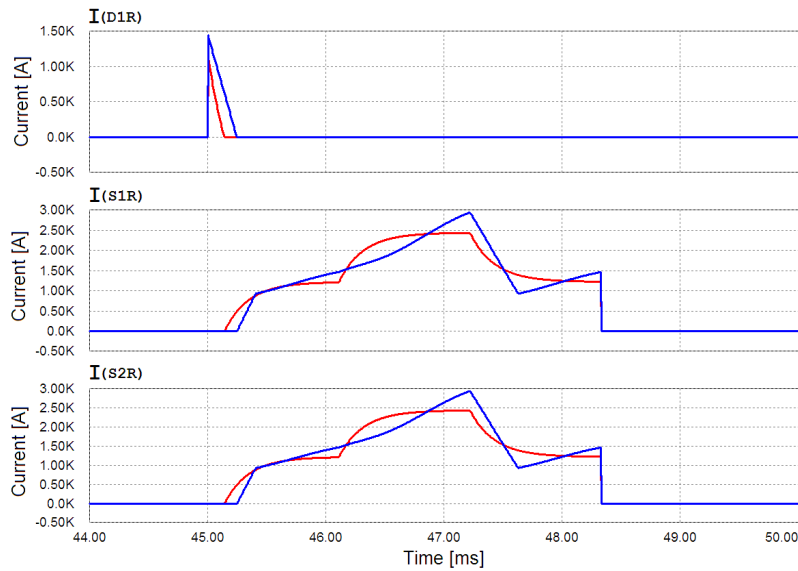*Figure 13-8 – NPC inverter switch currents for m=1 and V$_{dc}$=5386 V, first stage. First row: current in the anti-parallel diodes. Second row: current in the external active switches. Third row: current in the internal active switches. In blue, the rated H- operation, first stage. In red, the case of R-L DL*

The respective average, rms and switch-off currents are compared in Table 13-2.

Table 13-2 – Currents in the inverter power switches with m=1 and V$_{dc}$=5386 V, for the first stage

Device	I$_{avg}$ [A]		I$_{rms}$ [A]		Switch-off current [A]	
	R-L DL	Rated H-operation	R-L DL	Rated H-operation	R-L DL	Rated H-operation
Anti-parallel diodes (D1x, D2x)	11.3	27	92	162	0	0
External active switch (S1x, S4x)	749	739	1158	1167	1227	1462
Internal active switch (S2x, S3x)	749	739	1158	1167	1227	1462
Freewheeling diodes (DF1x, DF2x)	0	0	0	0	0	0

Comparing the waveforms and the values, it can be noted that the anti-parallel diodes are less stressed in case of R-L DL with respect to the rated Hydrogen operation. Conversely, the average and rms currents in the active switches are very similar, but the switch-off current is a bit lower. The differences in the current peaks between reference H- case and R-L DL operation (for m = 1) is due to the current oscillations produced by the HV dc-filter in the reference case, which obviously cannot be reproduced by a R-L DL.

In conclusion, the R-L DL can reproduce similar current stresses (and then transient thermal stresses) in the active switches with respect to the reference case, thus it seems suitable to test the AGPS inverters.

Estimation of the volume of the resistor of the R-L dummy load

In this paragraph, the volume of the resistor of the R-L DL for the first stage is estimated, assuming a resistance of 1.47 Ω (three-phase), a nominal operational time of the DL equal to t_{MAX} = 1 s and a rms line current I_{INV} = 1700 A (rated inverter current).

The energy to be dissipated by the R-L DL can be calculated as follows:

$$E \cong 3 \times R_1 \times I_{INV}^2 \times t_{MAX} = 12.7 \text{ MJ} \tag{13-8}$$

It is assumed that the maximum over-temperature in the resistor is ΔT = 200 °C (a usual value for resistor of these size and characteristics). It is considered that the resistor is made of AISI 310 stainless steel, which has the following typical parameters:

Density: $\rho_{AISI} = 8000 \text{ kg/m}^3$
Specific heat: $cs_{AISI} = 500 \text{ J/(kg K)}$
Resistivity: $r_{AISI} = 78 \cdot 10^{-8} \text{ } \Omega\text{m}$

Considering an adiabatic heating of the resistor when the inverter is operating, in order to limit the maximum over-temperature to ΔT = 200 °C, the minimum mass of the stainless steel shall be:

$$m_{AISI} = \frac{E}{cs \cdot \Delta T} = 127 \text{ kg} \tag{13-9}$$

To satisfy this condition and to have at the same time the correct resistance value, the section S_{AISI} and the total length l_{AISI} of each resistor phase have to satisfy the following equation system:

$$\begin{cases} R_1 = r_{AISI} \cdot \dfrac{l_{AISI}}{S_{AISI}} \\ m_{AISI} = 3\rho_{AISI} \cdot S_{AISI} \cdot l_{AISI} \end{cases} \qquad (13\text{-}10)$$

The solution of the equation system is the following:

l_{AISI} = 100 m

S_{AISI} = 53 mm^2

In order to estimate the total resistor volume, it is assumed that the resistor is composed by a number of elemental resistors, having the following dimensions: 1 mm × 26.5 mm × 500 mm (which are very similar to those of the basic resistors of the poloidal circuit of the RFX experiment [24]). It could be noted that the section of the elementary resistor is half of S_{AISI}. The resistance of such element can be calculated as:

$$R_{elem} = r_{AISI} \frac{l}{S} = 14.7 \text{ m}\Omega \qquad (13\text{-}11)$$

To achieve the desired total resistance, 2 · l_{AISI} / 0.5 m = 400 basic resistors are needed for each phase. A possible configuration of such elements is represented in Figure 13-9. The block represented here is formed by 10 basic elements in series. Such blocks can be connected in parallel two by two. In total, 40 blocks for each phase are needed. Assuming a distance d_i = 20 mm between the elemental resistors, each block would have the following dimensions: (20 × 9 + 1 × 10) × 26.5 mm × 500 mm. The electro-dynamic forces on two conductors with a 20 mm gap in between, with a current peak I_{pk} = [6500 / (1.5 × R_1)] / 2 = 1.47 kA are:

$$F = \frac{\mu_0 \cdot I_{pk}^{2} \cdot l}{2\pi \cdot d_i} = 10.9 N \qquad (13\text{-}12)$$

This force is quite low, also considering that a thickness of 1 mm has been assumed for the basic resistor. Probably the elements could be mounted also closer each other.

Assuming to place the blocks taking a gap in between of 100 mm in the horizontal direction and 30 mm in the vertical direction, and to place them as 1 × 2 horizontally and 20 vertically, each phase of the DL resistor would have the following volume:

V_{phase} = 0.5 × (0.19 × 2 + 0.1) × (0.0265 × 20 + 0.03 × 19) = 0.5 × 0.48 × 1.1 = 0.26 m^3 (13-13)

The 3 phases can be assembled together. Assuming a distance of 10 cm between the resistor phases, for the total three-phase resistor the following total volume can be calculated:

$$V_{tot} = 0.5 \times (0.5 \times 3 + 0.1 \times 2) \times 1.1 = 0.5 \times 1.7 \times 1.1 = 0.94 \text{ m}^3 \qquad (13\text{-}14)$$
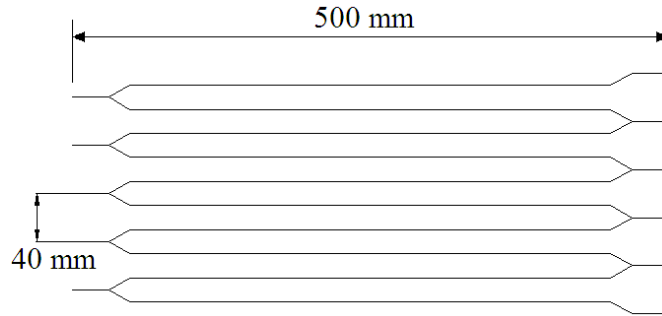

Figure 13-9 – Basic block of the resistors of the R-L dummy-load

The useful surface of the resistor as far as the heat exchange is concerned can be calculated as: $A_{AISI} = 200 \times 0.055 \times 3 = 33 \text{ m}^2$ for the three phases, whereas the total thermal capacitance is $C_{AISI} = m_{AISI} \times c_{sAISI} = 127$ kg $\times$ 500 J/(kg K) = 63500 J/K. Supposing that the heath exchange with the ambient is due to natural air convection only, the thermal resistance between resistor and surrounding ambient can be calculated with the following equation:

$$R_{air\_nat} = \frac{1}{\alpha_{air} \cdot A_{AISI}} = 2.73 \cdot 10^{-3} \text{ K/W} \qquad (13\text{-}15)$$

where $\alpha_{air} = 15 \text{ W/(m}^2\text{K)}$ is the coefficient for the heat exchange here assumed. Therefore, the time constant for the heat exchange can be calculated as:

$$\tau_{th} = R_{air\_nat} \cdot C_{AISI} = 173 \text{ s} \qquad (13\text{-}16)$$

Thus, starting from an initial over-temperature of 200 °C, the over-temperature would decay below 1.3 °C after $5\tau_{th}$ = 865 s = 14 minutes, a time which should be acceptable for the tests. If not, it could be possible to improve the heat exchange by using fans.

13.1.4 Studies on the dummy load making switches

The DL has to permit also to simulate the grid BD. To do that, the DL is provided with making switches, to short circuit part of the impedance on each phase. When the making switches are shorted, the residual impedance of each phase shall be inductive and equal to L_{tot1}, to simulate the short-circuit impedance of the step-up transformer and the decoupling

inductances of the AGPS inverters, which limit the current derivative during the grid BD. For the R-L DL, this corresponds to short circuit the resistive part of the DL.

In principle, the making switch system can be constituted by 2 or 3 making switches, as represented in Figure 13-10 for the R-L DL.
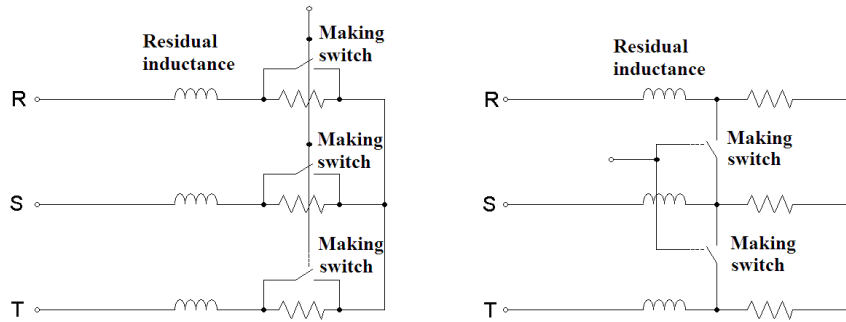

Figure 13-10 – Possible schemes for the R-L DL making switches

These two schemes are electrically equivalent, but the second requires one switch less. In both cases, the maximum over-current during short-circuit appears when the short is applied during a time interval in which one phase to neutral voltage is $+V_{dc}/2$ and the other two are $-V_{dc}/2$ (or vice-versa). This can occur only for m > 2/3. In this case, the maximum current derivative can be calculated with eq. (11-2) if $L_1 = L_{tot1}$. Then, it can be concluded that a making switch system having the scheme of Figure 13-10 can reproduce the same over-current which occurs as a consequence of a grid BD.

If 1/3 < m < 2/3, this worst case cannot occur, and the maximum over-current has to be calculated with the following equation:

$$\left. \frac{di_1}{dt} \right|_{max} = \frac{V_{dc}}{2 \cdot L_1} \qquad \text{for } 1/3 < m < 2/3 \qquad (13\text{-}17)$$

The inverter output current should increase for less than 150 μs, which is the maximum time delay specified between the BD and the opening of all the inverter active switches (Table 6-4). During this time, however, some active switches commutate, so the time derivative of the current decreases (as shown in section 11.2).

In case of R-L DL, for the same rms output current (1644 A), between the two cases $V_{dc} = 5386$ V (m = 1, [eq. (11-2)]) and $V_{dc} = 6500$ V (m ≅ 0.64 < 2/3, [eq. (13-17)]), the first one is the worst, in the sense that it can produce higher over-currents than the second one (1766 A against 1598 A, for a 150 μs short-circuit duration).

To reduce the number of making switches, it could be possible to partially simulate a BD by short-circuiting two phases only, as in Figure 13-11. In the same Figure it is represented the equivalent scheme when the making switch is operated, considering the case of a R-L DL.
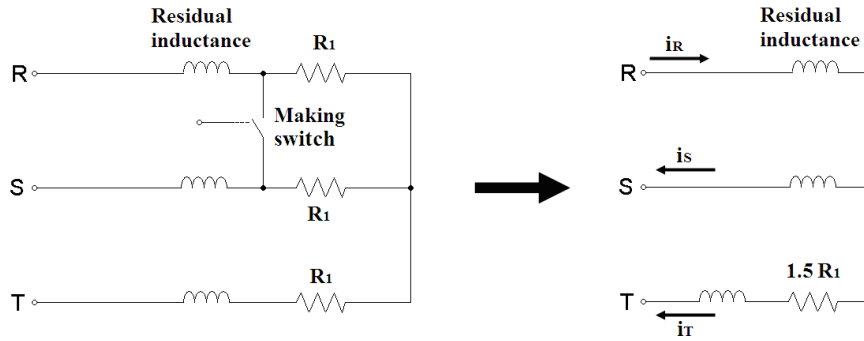
Figure 13-11 – Scheme with single making switch and equivalent scheme after short-circuit

For m > 2/3, if, as before, the phase to neutral voltage of the phase R is $+V_{dc}/2$ and the other two are $-V_{dc}/2$, the current derivative of the phase R can be calculated as:

$$\left.\frac{di_1}{dt}\right|_{max} = \frac{V_{dc}}{2 \cdot L_1}\left(1 + e^{-t\frac{R_1}{L_1}}\left(\frac{1}{3} + \frac{I_T R_1}{V_{dc}}\right)\right) \qquad \text{for m > 2/3} \qquad (13\text{-}18)$$

where I_T is the initial current on the phase T not short-circuited. The time constant L_1 / R_1 (207 µs) is comparable to the maximum foreseeable switch-off delay after a grid BD (150 µs). Therefore, the maximum over-current with a single switch, for V_{dc} = 5386 V, I_T = 0 and m > 2/3, is 1639 A (-7.2% against 1766 A of the full making switch). If I_T < 0 (exiting from phase T), the over-current is lower, if I_T > 0 it is higher.

In conclusion, the implementation of a single making switch is simpler (because no synchronization among the switches is needed), but the produced over-current is different from the real case, depending on the initial current in the phase not short-circuited. Therefore, a making switch system based on the scheme of Figure 13-10 (with two switches) is recommended as reference design.

With the R-L DL proposed before in this section for the first stage (R_1 = 1.47 Ω, $L_1 = L_{tot1}$), when the rms output line current of the inverter is 1700 A, the maximum peak of the inverter output current is 2615 A, which occurs for $V_{dc} \cong 5850$ V (m > 2/3). If the making switch system proposed here is associated with this R-L DL, and the short-circuit is applied in correspondence of the peak of the inverter output current, assuming a time delay of 150 µs before the opening of all the active switches, the current can increase up to:

$$I_{MS\,max} \cong 2615A + \frac{5850V}{1.5 \cdot L_1} \cdot 150 \mu s = 4533 \text{ A} \qquad (13\text{-}19)$$

This value is confirmed by simulation, as shown in Figure 13-12. Taking some margin, the making switch should be rated for a maximum current peak of at least 5.2 kA. This margin

takes into account for example the malfunction of the BD protection and the intervention of the inverter over-current protection. In this case, an additional time delay of 50 µs has been taken into account.
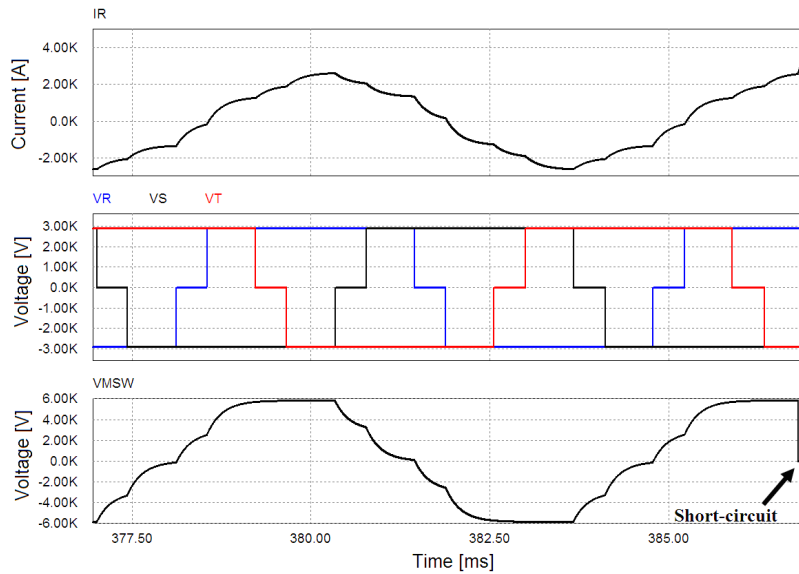

Figure 13-12 – Results for the making switch system of Figure 13-10 (2 switches), applied to the R-L DL with R_1=1.47 Ω and L_1=L_{tot1} (first stage), for V_{dc}≅5850 V. First row: line current at the inverter output, controlled to achieve 1700 A rms. Second row: phase to neutral voltages at the inverter output. Third row: voltage across the making switch placed across the phases R and S. The short-circuit is applied near the peak of the line current (on the right), for 150 µs

The maximum voltage across the making switches when they are open is equal to V_{dcmax} = 6.5 kV + 9% = 7085 V. It would be 7085 V × 2/3 = 4723 V if a making switch system based on three switches was used.

In conclusion, the requirements proposed for the making switch (based on two switches) are summarized in Table 13-3. A solution based on thyristors (two in anti-parallel for each branch) seems feasible for this device.

Table 13-3 – Main requirements proposed for the making switch of each stage (based on 2 switches, in case of R-L DL)

Type	Bidirectional three-phase making switch
Number of switches	2 bidirectional switches
Rated peak current	5.2 kA
Maximum current duration	200 µs
Rated peak voltage	7.1 kV
Maximum di/dt	20 A/µs

13.1.5 Conclusions

To test the AGPS dc/ac inverters at the rated rms current (H- operation) without having the DCG, a set of DL is required. In [25], three-phase inductive DL are foreseen, to avoid the need of high active power from the grid network.

By simulations, the rms, average and turn-off currents in the switches have been calculated both for the reference case and with inductive DL. Due to the phase shift between load voltage and current, important differences have been identified, showing for example that the anti-parallel diodes are much more stressed by the inductive DL. Moreover, all the inverter reactive input power is exchanged with the dc-link capacitors, causing much higher rms current to be delivered by the dc-link itself. To achieve similar transient thermal stresses on the anti-parallel diodes and to reduce the electrical stress on the dc-link capacitors, the DL inductance should be increased, resulting in lower rms current for the same dc-link voltage.

To reproduce switching conditions similar to that of the real case, a resistive-inductive (R-L) DL has been proposed. Current waveforms and values close to the reference case have been calculated by simulation. Differences are due to the HV dc-filter, which in the real case produces current oscillations over imposed to the ideal waveforms. An estimation of the volume of the resistors has been derived, showing reasonable values if the maximum on time of the DL is reduced to 1 s every 900 s. Obviously, using R-L DL, high pulsed active power shall be available from the grid.

To simulate the over-currents at the output of the AGPS inverters due to grid BD, in [25] a three-phase making switch is required. In this section, possible schemes for these making switches have been compared, showing the possibility to use only two or even one making switches. Nevertheless, with one making switch only, the over-current cannot be reproduced accurately, depending also on the load currents before the short-circuit. Therefore, a making switch system based on two switches has been proposed as reference design, and a set of electrical requirements has been derived.

13.2 Tests on the inverter voltage control loop

13.2.1 Introduction

To test the AGPS dc output voltage control loop, the dc output voltage measurements are necessary. Being the DCG not available during the acceptance tests of the AGPS-CS, to generate voltage measurements similar to those produced by the DCG in the same electrical conditions (dc-link voltage, modulation index), the dedicated DCG simulator of Figure 13-13 is proposed.

The DCG simulator, connected directly at the output of a dc/ac inverter under test, reproduces the scheme of the DCG circuit (represented in Figure 7-5), but with proper scaling of the dc output voltage and current, to simplify the voltage insulation requirements and to reduce the power flowing into the simulator with respect to the real DCG, minimizing therefore the cost.
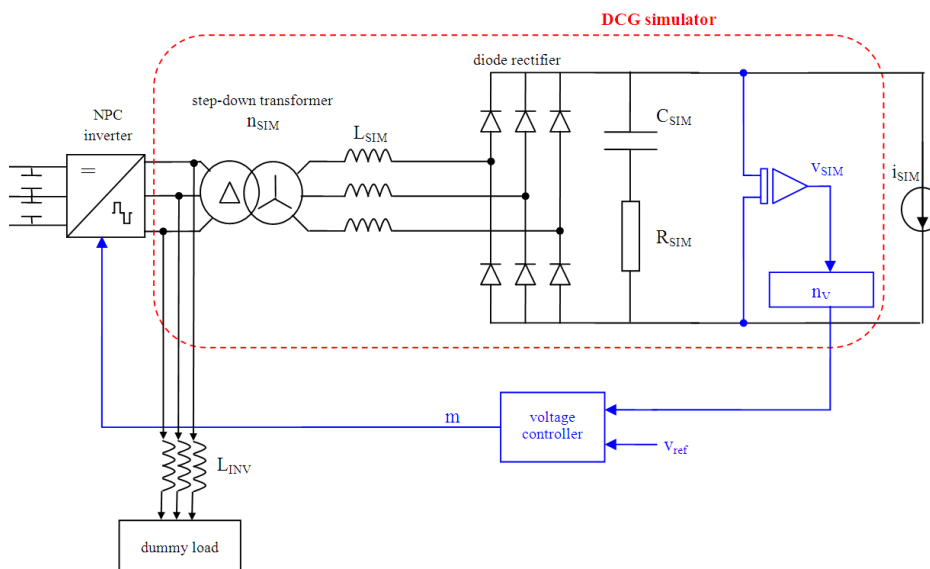

Figure 13-13 – Block diagram of the circuit proposed for testing the AGPS voltage control loop

To work properly, the DCG simulator has to receive as input the same phase voltages that would be produced by the AGPS dc/ac inverters connected to the respective DCG. Therefore, the inverter active switches shall commutate correctly. To do that, probably a certain minimum current shall flow in the switches and the related circuitry (snubbers, for example). Therefore, a minimum load shall be connected at the inverter outputs, downstream the decoupling inductances. This load could be for example the DL foreseen for the AGPS tests at high power (see section 13.1) or, alternatively, a dedicated high impedance DL. In the latter case, the need to have five high power (and costly) DL to test the voltage control loops of the five stages together is removed. The final choice could be left to the Supplier. In fact, the main impact of the DL in the test with DCG simulator is just the dc-link voltage drop due to the discharge of the dc-link capacitor bank during the load current ramp-up.

13.2.2   Calculation of the DCG simulator parameters

The DCG simulator has the same topology of the DCG, but different values of the parameters. A step-down three-phase delta-star transformer (with primary/secondary turn ratio n_{SIM}) is connected directly to the inverter output terminals, upstream the inverter decoupling inductances. At the secondary side, this transformer is connected to a three-phase low voltage diode bridge. The total equivalent series inductance of the step-down transformer (at the secondary side, including cable leakage inductance) is L_{SIM}. This inductance should simulate the total equivalent inductance at the secondary side of the DCG step-up transformer L_{tot2}. At the dc side of the diode bridge, a low voltage dc-filter is connected, in parallel to a low power load.

To design the DCG simulator, two scaling factors are considered: the dc output voltage scaling factor, n_V = 5000, and the dc load current scaling factor, n_C = 5. In any case, the Supplier could make also a different choice for n_V and n_C; the values assumed here are tentative, with the only aim of demonstrating the principle of the DCG simulator. In any case, n_V and n_C shall be chosen so that the second order effects, such as the voltage drop on the diode rectifier or the magnetizing current of the step-down transformer, are negligible, as in the real DCG.

With the values assumed for n_C and n_V, the dc output voltage, current and power of the DCG simulator, if the nominal D- operation is reproduced, are (for the first stage):

$$V_{SIM} = V_{stage1} \, / \, n_V = 200000 \, / \, 5000 = 40 \text{ V} \tag{13-20}$$
$$I_{SIM} = I_{stage1} \, / \, n_C = 59.4 \, / \, 5 = 11.9 \text{ A} \tag{13-21}$$
$$P_{SIM} = V_{SIM} \times I_{SIM} = 40 \times 11.9 = 476 \text{ W} \tag{13-22}$$

where V_{stagen} and I_{stagen} are respectively the dc output voltage and current of the n-th DCG (n = 1 in this case). The voltage scaling factor n_V has been chosen as a compromise between a reasonable turn ratio of the step-down transformer and the minimization of the power flowing in and dissipated by the DCG simulator. In particular, the step-down transformer turn ratio can be calculated with the following equation:

$$n_{SIM} = n \times n_V = (1/18.2) \times 5000 = 274.7 \tag{13-23}$$

The total equivalent series inductance of the step-down transformer L_{SIM} is calculated in order to have the same per unit voltage drop due to the total equivalent series inductance L_{tot2} on the real DCG. The voltage drop on the inductance L_{tot2} is proportional to the product L_{tot2} x

I_{DCG}. Being the dc output voltage reduced by the factor n_V and the dc output current reduced by the factor n_C, L_{SIM} can be calculated as follows:

$$L_{SIM} = \frac{L_{tot\,2} \cdot I_{stagen}}{V_{stagen}} \cdot \frac{V_{stagen}}{n_V} \times \frac{n_C}{I_{stagen}} = \frac{L_{tot\,2} \times n_C}{n_V} = \frac{0.303 \times 5}{5000} = 303 \text{ μH} \qquad (13\text{-}24)$$

With the present choice of n_C and n_V, the value derived for L_{SIM} seems reasonable. In any case, if (for technical reasons) this value is higher than the real leakage inductance of the step-down transformer, a proper three-phase series inductance shall be added at the secondary side.

The dc-filter capacitance C_{SIM} is calculated in order to keep the same ratio between the DCG output power and the energy stored in the dc-filter of the real DCG. Therefore, the following equation can be derived:

$$\frac{V_{stagen} \times I_{stagen}}{\frac{1}{2} C_f V_{stagen}^2} = \frac{V_{SIM} \times I_{SIM}}{\frac{1}{2} C_{SIM} V_{SIM}^2} \qquad (13\text{-}25)$$

which gives:

$$C_{SIM} = C_f \frac{V_{stagen}}{V_{SIM}} \frac{I_{SIM}}{I_{stagen}} = C_f \frac{n_V}{n_C} = 300 \times 10^{-9} \frac{5000}{5} = 300 \text{ μF} \qquad (13\text{-}26)$$

The dc-filter resistance R_{SIM} is computed in order to have the same time constant $R_f \times C_f$ of the real DCG, as follows:

$$R_{SIM} = \frac{R_f \times C_f}{C_{SIM}} = \frac{R_f \times C_f}{C_f \times \dfrac{n_V}{n_C}} = R_f \times \frac{n_C}{n_V} = 68 \times \frac{5}{5000} = 68 \text{ mΩ} \qquad (13\text{-}27)$$

To reproduce accurately the real load of the DCG, the load of the simulator should be a constant current generator, where the current is controlled in order to reproduce the perveance matching law [eq. (4-1)], as specified for the definition of the voltage rise time in Table 6-2, note 4.

$$I_{SIM} = kV_{SIM}^{1.5} \qquad (13\text{-}28)$$

Various feasible technical solutions can be devised to realize such a generator. In any case, it could be possible also to test less precisely the AGPS dynamic performance by using a simplified load, as for example a resistor.

The voltage across the load is measured and it is multiplied by the voltage scaling factor n_V. The result is the simulated dc voltage measurement for the AGPS voltage control loop.

13.2.3   Simulation of the DCG simulator

The principle and the design of the DCG simulator have been verified with the PSIM™ model represented in Figure 13-14. In this model, the AGPS inverter is connected at the output to the R-L DL proposed in section 13.1.3 for the first stage and to the DCG simulator. Here, the AGPS inverter is controlled with the same voltage control loop used to verify the AGPS dynamic performance and described in section 9.4. This control loop includes a PI regulator with feed-forward contribution from the voltage reference.
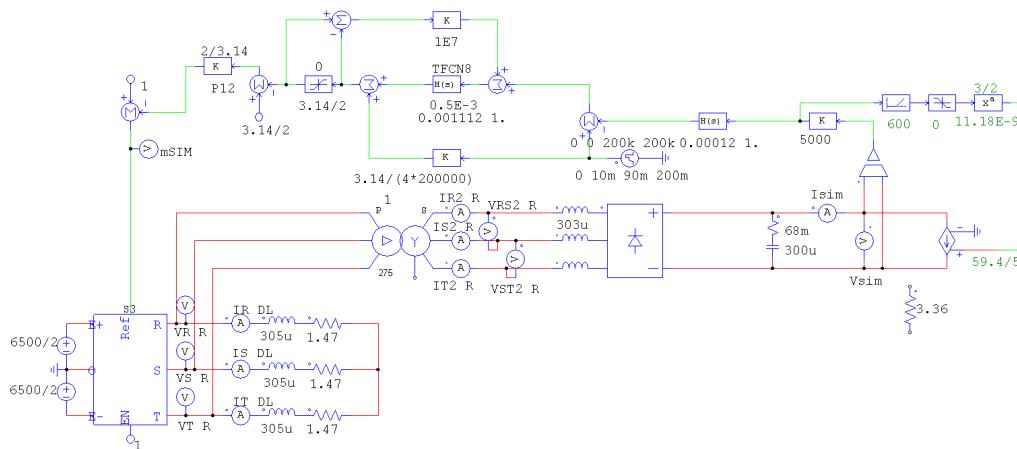

Figure 13-14 – PSIM™ model of the assembly for testing the AGPS voltage control loop for the first stage. The block S3, representing the AGPS dc/ac inverter, is detailed in Figure 9-2

In the model of Figure 13-14, the load of the DCG simulator is a current generator, controlled to simulate the nominal DCG output current for the first stage (D- operation) in agreement with the perveance matching law [eq. (13-28)], as in the simulations of the dynamic performance of section 11.1.

The results obtained with this model are compared with those of the simplified model of the first dc/ac inverter stage connected to the real DCG (similar to that described in section 9.7). In both models, the dc-link is represented as two ideal voltage generators. This means that the dc-link voltage drop during the ramp up of the output current is neglected. Of course, this voltage drop is almost zero if a high impedance DL is used for testing the voltage control loop using the simulator.

In the simulation, the voltage reference ramps up to the rated value (corresponding to 200 kV, D- operation) in 80 ms, as in section 11.1. The time evolutions of the dc output voltages and currents achieved with the model of Figure 13-14 and the model of the real first dc-dc conversion stage are compared in Figure 13-15. The instantaneous values, normalized with the respective factors n_V and n_C, are identical.
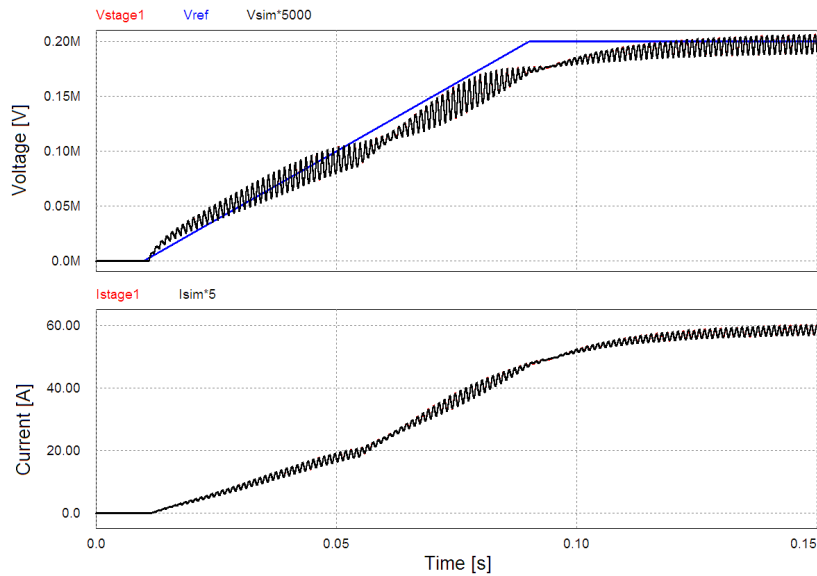

Figure 13-15 – First row: dc output voltage reference (blue), dc output voltage from the model of the real DCG (red) and of the DCG simulator (black, multiplied by 5000). Second row: dc output current from the model of the real DCG (red) and of the DCG simulator (black, multiplied by 5). In both models, the output current is controlled in agreement with the perveance matching law

The simulation has been repeated considering a simple resistor as low power load for the DCG simulator. The resistance value has been assumed as 40 V / 11.9 A = 3.36 Ω. The result is shown in Figure 13-16. Clearly, if the load is changed, also the dynamics of the overall conversion stage changes. However, the difference in the output voltage is little, and maybe it could be accepted, with the aim to simplify the test set-up.
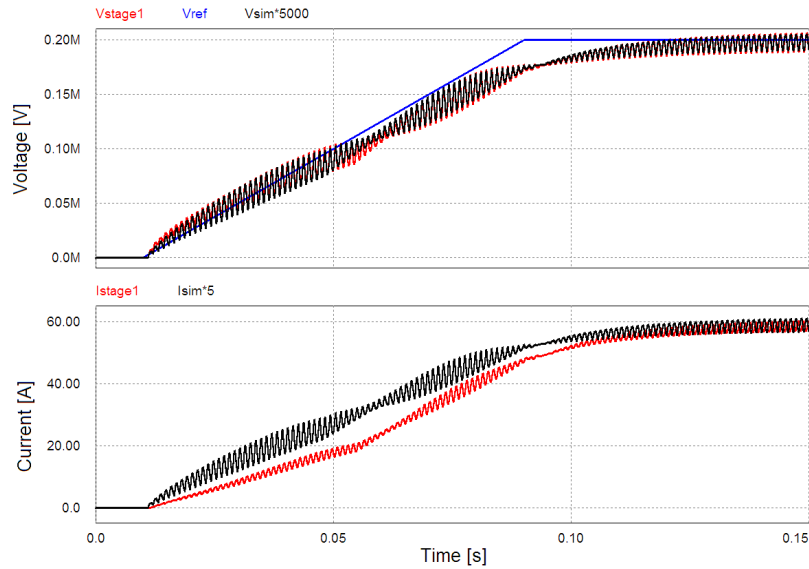
Figure 13-16 – First row: dc output voltage reference (blue), dc output voltage from the model of the real DCG (red) and of the DCG simulator (black, multiplied by 5000). Second row: dc output current from the model of the real DCG (red) and of the DCG simulator (black, multiplied by 5). For the real DCG, the output current is controlled in agreement with the perveance matching law, whereas for the DCG simulator the load is a pure resistor

13.2.4   Conclusions

Being the DCG unavailable at the time of the acceptance tests of the AGPS-CS, a suitable DCG simulator has been proposed, with the aim of testing the AGPS voltage control loop by replicating the DCG output voltage measurements. It has been demonstrated that equivalent voltage measurements can be reproduced without generating the DCG high voltage, with a simple low power circuit. Being the DCG circuit topology just duplicated and scaled down in terms of voltages and currents, the DCG simulator shows the same dynamic behaviour of the real DCG, as demonstrated by simulations. It has been shown also that the AGPS dynamic performance could be tested (with less accuracy) by using just a resistor as load of the DCG simulator, instead of replicating the typical voltage/current characteristic of the DCG load (in which the current is imposed by an external circuit).

During the test of the voltage control loop with DCG simulator, the AGPS dc/ac inverter shall be connected to a minimum load able to guarantee the regular switching function of the inverter, in order to generate at the inverter outputs the typical voltage waveforms of a NPC inverter for the given modulation index. The influence of the DL current in the output voltage waveforms and in the dynamic performance with the DCG simulator is negligible (just the dc-link voltage drop is affected) if the simulator is applied directly at the output of the inverter under test, upstream the inverter decoupling inductances, and if the inverter is switching properly.

In section 13.1, a R-L DL has been proposed, with the aim of testing the AGPS inverters at the rated rms output current, which occurs in case of rated H- operation. The proposed R-L DL

has been designed assuming maximum modulation index (m = 1) and dc-link voltage equal to 5386 V. If the same DL designed for testing the AGPS inverters at full power (in current control loop) is used for the voltage control loop test, special care shall be taken to avoid exceeding the DL and inverter rated parameters, in particular their rated rms current. In fact, some combinations of inverter modulation index and dc-link voltage (for example, V_{dc} = 6500 V and m $\cong$ 1, D- operation) can produce rms currents in the DL higher than the respective rated current.

14 Conclusions

The activity that gave origin to this thesis has been carried out in the framework of the research for the ITER Neutral Beam Injection system, and in particular for its Acceleration Grid Power Supply.

On this basis, the author contributed to the definition of the present reference design of the AGPS by performing technical considerations and calculations of the parameters and ratings of the main components. The author studied also the AGPS control system, with the aim to find technical solutions in order to comply with the functional requirements.

A set of models has been developed by the author to verify the compliance of the AGPS to the electrical specifications. The steady state performance of the AGPS has been verified by simulation: in particular, it has been found that, under certain constraints on the steady state error of the dc-link voltage, the dc output voltage can be reached in nominal operating conditions with the present step-up transformer turn ratio. The voltage ripple is lower than the required maximum value if the dc-link voltage is properly controlled, also without phase shifting the inverter switching carriers. The currents in the inverter power switches have been simulated, confirming that at least two IGCT in parallel for each inverter stage leg or two basic bridges for each dc/ac inverter stage have to be provided to guarantee the rated output voltage and current.

As far as the simulations on the AGPS dynamic performance are concerned, it has been found that the specified rise time of the output voltage can be achieved also by choosing 150 Hz as fundamental frequency for the inverter output voltage square waveform, taking some provision on the control system and the voltage reference. The maximum over-currents produced by the dc/ac inverters in grid breakdown conditions have been estimated and the actual maximum inverter switch-off time has been evaluated in detail. In addition, the over-voltages at the AGPS outputs caused by a sudden loss of load (beam-off) have been evaluated, both in case of intervention of the protection and in case of protection fault. These over-voltages however do not represent the worst case. Further considerations on over-voltages in various fault conditions can be carried out, considering together the fault probability and the over-voltage amount.

To estimate the voltage oscillations that could occur on the AGPS conversion system in case of grid breakdown, induced from the secondary to the primary side of the step-up transformers through their stray capacitances, a dedicated HF model has been developed by the author, based on a set of assumptions on the stray parameters and the AGPS layout. Even if the model is simplified with respect to reality, useful suggestions have been derived for the AGPS grounding connections and the most critical stray parameters have been identified.

Particular attention has been paid to specific aspects of the tests to be carried out on the real AGPS system to verify the compliance with the given requirements. In particular, an alternative type of dummy load (resistive and inductive) has been proposed, to more accurately reproduce the current waveforms on the inverter power switches under nominal operating conditions. The feasibility of such dummy load has been proven by calculations and the proper operation has been verified through computer simulations. Different solutions for the making switches aiming at simulating the breakdown conditions have been analyzed and compared. Finally, a technical solution to test the AGPS voltage control loop in the absence of the final stages and the respective dc output voltage measurements has been proposed and validated by additional computer simulations. This will be particularly useful during the acceptance tests of the conversion system.

The technical developments and the results achieved with the calculations and the models presented in this thesis have been widely used to support the design of the AGPS and the definition of the functional and technical specifications of the AGPS conversion system. In particular, this work helped in achieving more confidence on the technical feasibility of the AGPS, finding also possible technical solutions in order to comply with the required performance. These analyses gave an important contribution also on the discussion about the interface parameters between the high voltage components, to be procured by the Japanese Domestic Agency, and the conversion system, to be procured by the European Domestic Agency. Moreover, these studies helped in the definition of additional technical constraints to be imposed to the Supplier in the technical specifications and of specific tests for the more critical aspects, allowing the increase of the reliability of the overall system.

15 Acknowledgments

16 References

[1] "Scaling up alternative energy", Science, Vol. 329, 13 Aug. 2010.

[2] Greene D.L., Hopson J.L. and Li J., "Running out of and into oil: analyzing global depletion and transition through 2050", ORNL/TM-2003/259, Oak Ridge National Laboratory, Oak Ridge, Tennessee, Oct. 2003.

[3] "Climate change 2007: the physical science basis, summary for policymakers", Fourth assessment report of the Intergovernmental Panel on Climate Change, Paris, Feb. 2007.

[4] Ongena J. and Van Oost G., "Energy for future centuries", Transactions for fusion science and technology, Vol. 49, no. 2T, 2006.

[5] Noterdaeme J.M., "Controlled fusion, from basic plasma physics to nuclear engineering", 12th International Conference on Emerging Nuclear Energy Systems, Brussels, Belgium, 21-26 Aug. 2005.

[6] Wesson J., "Tokamaks", Clarendon Press, 2004.

[7] Faulconer D.W., "Current drive", Transactions for fusion science and technology, Vol. 49, no. 2T, 2006.

[8] Koch R., "Plasma heating by neutral beam injection", Transactions for fusion science and technology, Vol. 49, no. 2T, 2006, pp. 167-176.

[9] http://www.iter.org

[10] Holtkamp N. and the ITER project team, "An overview of the ITER project", Fusion Engineering and Design, Vol. 82, no. 5-14, 2007, pp. 427-434.

[11] Maisonnier D. et al., "The European power plant conceptual study", Proc. of the 23rd Symposium of Fusion Technology, SOFT 23, Fus. Eng. Des., Vol. 75-79, Nov. 2005, pp. 1173-1179.

[12] How J., ITER Plant Integration Documentation, ITER_D_2234RH, ver. 3.0, Jan. 2007.

[13] Antoni V. et al., "The ITER Neutral Beam system: status of the project and review of the main technological issues", invited talk, 24th Symposium on Fusion Technology, Sept. 2006, Warsaw, Poland.

[14] ITER Design Description Document (DDD) 5.3, "Neutral beam heating & current drive system", July 2003.

[15] Ikeda Y. et al., "Recent R&D activities of negative-ion-based ion source for JT-60SA", IEEE Trans. on Plasma Science, Vol. 36, no. 4, Aug. 2008.

[16] Sonato P., "The neutral beam test facility in Padova: the necessary step to develop the neutral beam injectors for ITER", invited talk, 26th Symposium on Fusion Technology, Sept. 2010, Porto, Portugal.

[17] Pamela J., "The physics of production, acceleration and neutralization of large negative ion beams", Plasma Phys. Control. Fus., Vol. 37 (1995), pp. A325-A336.

[18] Hemsworth R. et al., "Status of the ITER heating neutral beam system", Nucl. Fusion, Vol. 49 (2009).

[19] Hanada M. et al., "Development of negative ion sources for the ITER neutral beam injector", Fus. Eng. and Des., Vol. 56-57 (2001), pp. 505-509.

[20] Franzen P. et al, "Progress of the development of the IPP RF negative ion source for the ITER neutral beam system", Nucl. Fusion, Vol. 47 (2007), pp. 264-270.

[21] P. Sonato et al., The ITER full size plasma source device design, Proc. of the 25th Symposium on Fusion Technology, Vol. 84, June 2009, pp. 269-274.

[22] Fubiani G., Hemsworth R.S., De Esch H.P.L. and Svensson L., "Analysis of the two accelerator concepts foreseen for the neutral beam injector of the international thermonuclear experimental reactor", Phys. Rev. ST Accel. Beams, Vol. 12 (2009).

[23] Gaio E., Toigo V., De Lorenzi A., Piovan R. and Zanotto L., "The alternative design concept for the ion source power supply of the ITER neutral beam injector", Fus. Eng. and Des., Vol. 83 (2008), pp. 21-29.

[24] Rostagni G., "RFX: an expected step in RFP research", Fus. Eng. and Des., Vol. 25 (1995), pp. 301-313.

[25] Annex B to Procurement Arrangement 5.3.P6.EU.01.0 between the ITER International Fusion Energy Organization for the Joint Implementation of the ITER Project and EU-Domestic Agency, ITER IDM ref. 2N8Z8F_v1_0.

[26] Zanotto L., Toigo V., Ferro A., Barp M., Laterza B., "Draft of the technical specification for Acceleration Grid Power Supply Conversion System and Ground Related Power Supply", Task deliverable T4.12/D2 of F4E Grant F4E-2009-GRT-32-PMS-H.CD, rev. 1, Nov. 2010.

[27] Mohan N., Undeland T.M. and Robbins W.P., "Elettronica di potenza", Hoepli edizioni, 2005.

[28] Toigo V. and Consorzio RFX project team, "Integrated Design Document of the Neutral Beam Power Supply System", EFDA Task: TW6-THHN-NBD1 – Design activities for the first ITER NB Injector, Task deliverable: 3.6.1 – Power Supply, March 2008.

[29] Nabae A. et al., "A new Neutral-Point-Clamped PWM inverter", IEEE transactions on industry applications, Vol. IA-1 7, no. 5, Sept/Oct 1981.

[30] http://www.powersimtech.com

[31] Zanotto L., Ferro A., Toigo V., "Assessment of performance of the acceleration grid power supply of the ITER neutral beam injector", Fus. Eng. and Des., Vol. 84 (2009), pp. 2037-2041.

[32] Piovan R., Novello L., De Lorenzi A., Gaio E., Milani F., "ITER NB Injector Test Facility: analyses of the impact on the high voltage network", Fusion Science and Technology, Vol. 52 (2007), pp. 403-407.

[33] Bigi M., De Lorenzi A., Grando L., Watanabe K. and Yamamoto M., "A model for electrical fast transient analyses of the ITER NBI power supplies and the MAMuG accelerator", Fusion Eng. and Des., Vol. 84 (2009), pp. 446-450.

[34] Guarnieri M. and Malesani G., "Elementi di Elettrotecnica – Reti Elettriche", II edition, Edizioni Progetto, Padova, 2001.

[35] Ferro A., Zanotto L., Toigo V., "Effects of the grid breakdowns on the Acceleration Grid Power Supply of the ITER NBI", 23rd Symposium on Fusion Engineering, June 2009, S. Diego, USA.

[36] Aristoncavi, "Medium voltage cables", brochure from http://www.aristoncavi.com, Jan. 2007.